MULTISTABILITY IN MICROBEAMS: NUMERICAL SIMULATIONS AND EXPERIMENTS IN CAPACITIVE SWITCHES AND RESONANT ATOMIC FORCE MICROSCOPY SYSTEMS

by

Devin Kalafut

A Dissertation

Submitted to the Faculty of Purdue University

In Partial Fulfillment of the Requirements for the degree of

Doctor of Philosophy

School of Mechanical Engineering

West Lafayette, Indiana

August 2021

THE PURDUE UNIVERSITY GRADUATE SCHOOL
STATEMENT OF COMMITTEE APPROVAL

Dr. Anil Bajaj, Co-Chair

School of Mechanical Engineering

Dr. Arvind Raman, Co-Chair

School of Mechanical Engineering

Dr. Marisol Koslowski

School of Mechanical Engineering

Dr. Aaron Yip

Department of Mathematics

Approved by:

Nicole L. Key

ACKNOWLEDGMENTS

This material is based upon work supported by the National Science Foundation Graduate Research Fellowship under Grant No. DGE-1333468. Any opinion, findings, and conclusions or recommendations expressed in this material are those of the author and do not necessarily reflect the views of the National Science Foundation.

Thanks to both the Ross Fellowship and the Alpha P. Jamison Professorship Endowment at Purdue University for providing support during this dissertation work.

TABLE OF CONTENTS

LIST OF TABLES

LIST OF FIGURES

ABSTRACT

Microelectromechanical systems (MEMS) depend on mechanical deformation to sense their environment, enhance electrical circuitry, or store data. Nonlinear forces arising from multiphysics phenomena at the micro- and nanoscale – van der Waals forces, electrostatic fields, dielectric charging, capillary forces, surface roughness, asperity interactions – lead to challenging problems for analysis, simulation, and measurement of the deforming device elements. Herein, a foundation for the study of mechanical deformation is provided through computational and experimental studies of MEMS microcantilever capacitive switches. Numerical techniques are built to capture deformation equilibria expediently. A compact analytical model is developed from principle multiphysics governing operation. Experimental measurements support the phenomena predicted by the analytical model, and finite element method (FEM) simulations confirm device-specific performance. Altogether, the static multistability and quasistatic performance of the electrostatically-actuated switches are confirmed across analysis, simulation, and experimentation.

The nonlinear multiphysics forces present in the devices are critical to the switching behavior exploited for novel applications, but are also a culprit in a common failure mode when the attractive forces overcome the restorative and repulsive forces to result in two elements sticking together. Quasistatic operation is functional for switching between multistable states during normal conditions, but is insufficient under such stiction-failure. Exploration of dynamic methods for stiction release is often the only option for many system configurations. But how and when is release achieved? To investigate the fundamental mechanism of dynamic release, an atomic force microscopy (AFM) system – a microcantilever with a motion-controlled base and a single-asperity probe tip, measured and actuated via lasers – is configured to replicate elements of a stiction-failed MEMS device. Through this surrogate, observable dynamic signatures of microcantilever deflection indicate the onset of detachment between the probe and a sample.

1. INTRODUCTION

This chapter is provided to set up broad concepts encountered in the dissertation research projects and to establish continuity across the body chapters which are published or submitted research articles in their own right. First, a brief background is provided to introduce the main topic. Next, motivation for specific research goals are outlined to address major unsolved problems in the associated body of previous literature. Finally, a preview to the chapters is included to describe how each stand-alone article-chapter fits together in the larger dissertation narrative.

1.1 Background

Beam-based microelectromechanical systems (MEMS) have been employed in several key application areas since their inception. As sensors, they are used to detect biological, environmental, and physical information [1]–[4]. In high-speed wireless communications they see use as capacitors, filters, switches, and resonators [5]–[9]. Possibly most interesting is their presence in memory storage, offering an option for non-volatile memory cells for extreme environments like outer space [10]. Examples of such beam-based device configurations are shown in Figure 1.1 and 1.2 for reference.

Application areas are driven by utilization of the electromechanical coupling, converting external energy input into mechanical deformation and in turn modifying electrical signals for readout. The external energy input may be added mass [11], pressure changes [12], acceleration [3], [13], electrostatic attraction, or direct applied force. The mechanical beam element of the MEMS device will then move and/or deform while under restriction of their designed boundary conditions: clamped ends, cantilevers, or even freely moving as a rigid body. When in different physical configurations due to such mechanical effects, the beam element will lead to a change in the electrical signal running through the system for measurement or information transfer.

Herein, the focus is on microcantilever capacitive switches, depicted in Figure 1.2, which operate at the intersection of many relevant multiphysics encountered at the micro- and nanoscale. Beam deformation is often viewed under the assumptions and analysis methods

of Bernoulli-Euler or the finite element method (FEM) [14], [15]. Electrostatic effects are described as a continuous extension of the parallel plate model with the possibility for fringe field effects up around the side walls of the beam element [16]. Finally, surface interaction forces, often adhesion, are of critical consideration at this scale from van der Waals forces [17]–[20], capillary effects [21], or electrostatic charging during device operation [22]. When all combined into a force balance with elastic restorative forces competing with actuation and adhesion, these MEMS devices can exhibit exotic nonlinear behavior exploitable for novel design.

The force balance, while integral to device operation profiles, can also lead to stiction-failure when attractive forces between two contacting surfaces overwhelm competing restorative forces from microbeam bending. Stiction-failure can be present in devices straight out of fabrication, but can also arise through operation due to surface roughness changes, dielectric charging, surface wetting due to humidity, and/or creep [21], [23]–[25]. Releasing a device from stiction-failure is of concern for the MEMS community, which has approached it by reducing adhesion or by excitation techniques to encourage detachment [26], [27].

1.2 Motivation

Determining the particular relationship between external energy input and resulting mechanical deformation of MEMS elements is the foundation for design and performance. Thus, designers first need access to computational tools for straightforward evaluation of static equilibria as a baseline for quasistatic device performance. Second, they need a compact analytical model of the microcantilever capacitive switch which encompasses all operating modes of the mechanical element shapes and multiphysics interactions. Hand-in-hand with the modeling is the need for experimental validation of the mechanical performance under relevant external actuation. Finally, when devices fail to stiction between contacting elements, researchers need an observable signature of dynamic detachment to inform release from contact.

1.3 Preview

Chapter 2 addresses the aforementioned call for numerical tools to identify mechanical deformation equilibria in MEMS devices. One software package, AUTO-07p, is introduced as a benchmark for solving nonlinear equilibria from analytical models. Another, COMSOL Multiphysics®, provides qualitatively and quantitatively similar performance on standard device configurations while allowing for additional numerical power in exploring models with complicated geometry – a struggle for analytical approaches. Several examples are explored to showcase this approach.

Chapter 3 builds on the analytical component of the prior chapter, but digs into the multistability present in a MEMS microcantilever capacitive switch. The existence of several stable states is revealed for a compact multiphysics model, along with the quasistatic operation limits governing the switching between configuration shapes of the deformable beam element. Operation regions of mono-, bi-, and tristability are all identified for physically-relevant model parameters, and an uncertainty quantification study is provided to determine the propagation of fabrication uncertainty through the dynamical model.

Chapter 4 pulls from the COMSOL Multiphysics® portion of the numerical equilibria solution methods and bolsters it with experimental validation through measurements of fabricated MEMS microcantilever capacitive switches. The multistability predicted in Chapter 3 is confirmed, while device-specific COMSOL Multiphysics® models provide device-specific explanation for performance variability. Under such validation, it is confirmed that the multiphysics phenomena are aptly captured by the modeling approach and is thus a suitable and computationally expedient technique for MEMS design as well as performance monitoring.

Chapter 5 is a departure from strictly MEMS focus and seeks to elucidate the dynamic nature of detachment between a vibrating microcantilever and a sample via an atomic force microscopy (AFM) system. Isolating the dynamic detachment mechanism in a single-asperity contact system of the AFM probe tip and the sample leads to observable signatures for release from contact. For AFM users this informs of an upper limit to measurements in a popular measurement mode, but for MEMS researchers it can inform of the initiation of detachment for stiction-failed members.

Chapter 6 summarizes the dissertation contributions and looks to the future for research projects adjacent to and stemming from the completed works in the main chapters. Both MEMS and AFM have unexplored phenomena relating to the precise nature of detachment dynamics which could be explored through analytical approaches as well as numerical computation.

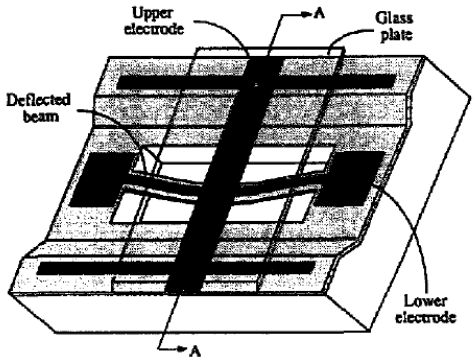

(a) Acceleration sensor [3]. [1]

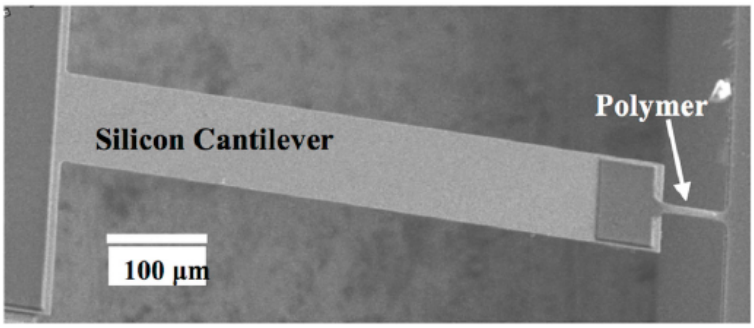

(b) Resonator [28]. [2]

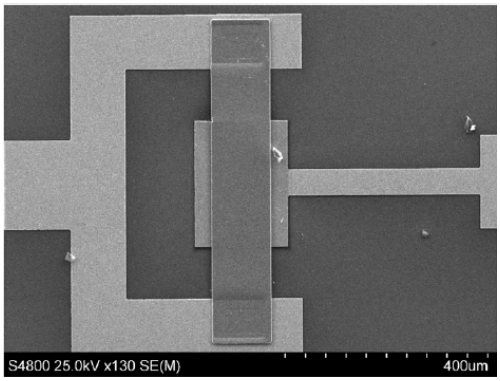

(c) Clamped capacitive switch [29]. [3]

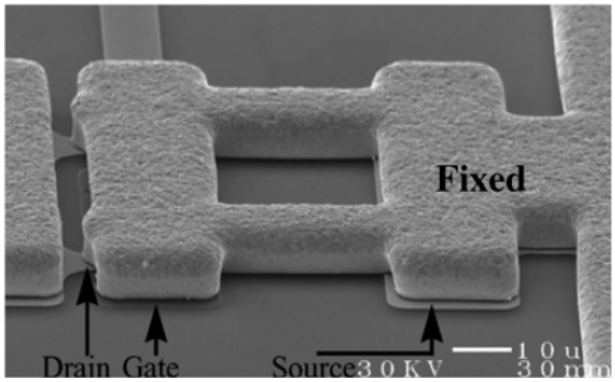

(d) Cantilever ohmic switch [30]. [4]

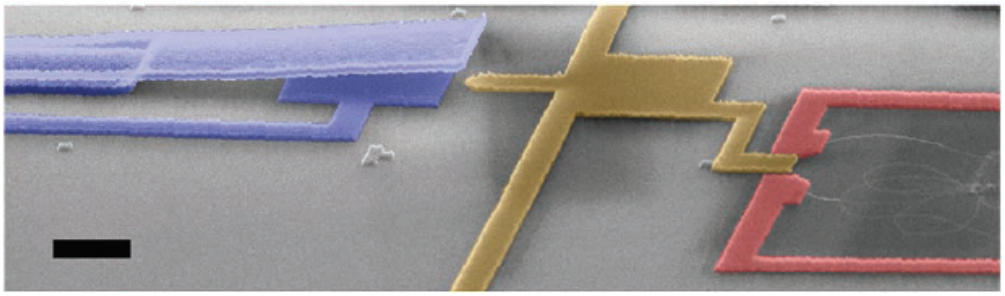

(e) Nonvolatile memory cell [31]. [5]

Figure 1.1. Example beam-based MEMS devices.

[1]↑ Republished with permission of Elsevier Science & Technology Journals, from *Snapping microswitches with adjustable acceleration threshold*, Y.-H. Cho et al., vol. 54, issues 1-3, copyright © 1996, DOI: https://doi.org/10.1016/S0924-4247(97)80018-0; permission conveyed through Copyright Clearance Center, Inc.

[2]↑ Reprinted figure with permission from Keivan Asadi et al., *Mechanism of geometric nonlinearity in a nonprismatic and heterogeneous microbeam resonator*, vol. 96, page 115306, 2017, DOI: https://dx.doi.org/10.1103/PhysRevB.96.115306. Copyright 2017 by the American Physical Society.

[3]↑ Sourced from Ryan C. Tung et al., *Estimating residual stress, curvature and boundary compliance of doubly clamped MEMS from their vibration response*, Journal of Micromechanics and Microengineering, vol. 23,

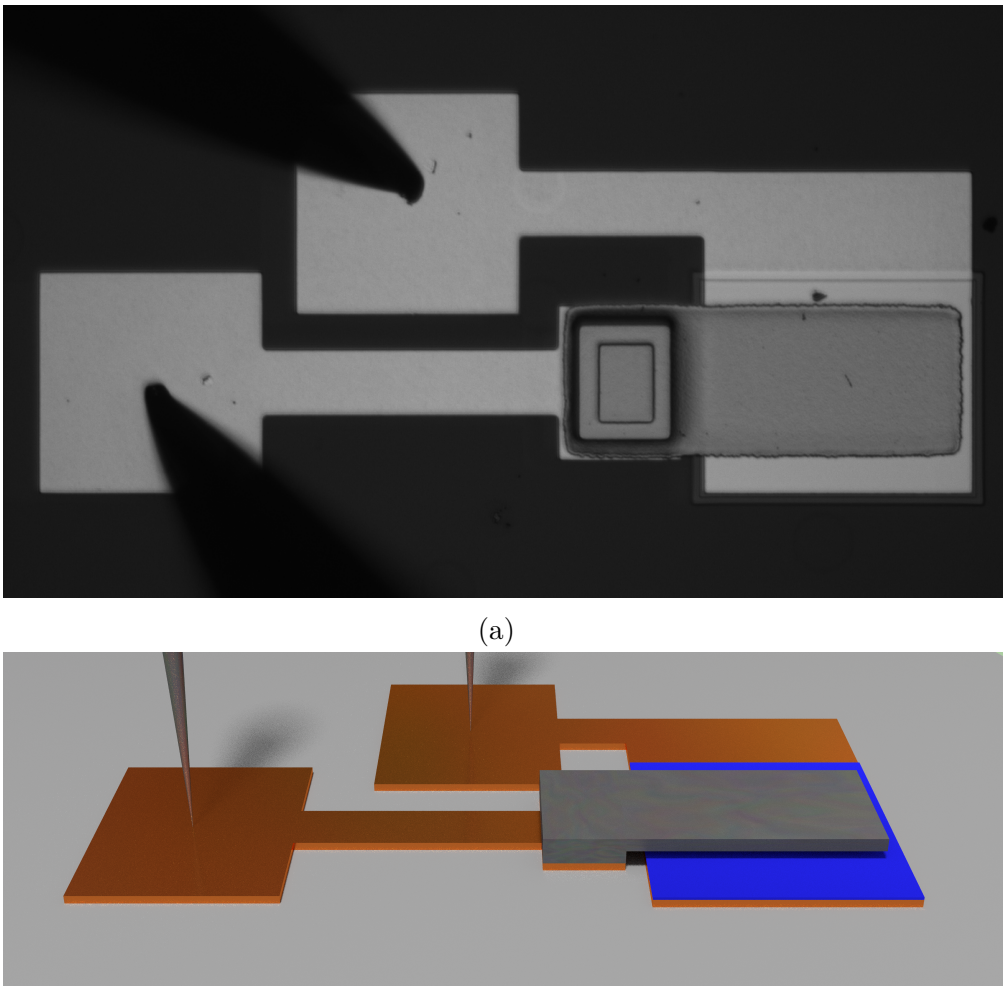

(a)

(b)

Figure 1.2. MEMS cantilever capacitive switch (a) top view from optical camera and (b) side view from rendered schematic.

no. 4, page 045009, 2013, DOI: https://doi.org/10.1088/0960-1317/23/4/045009. © 2013 IOP Publishing. Reproduced with permission. All rights reserved.

[4]↑ Sourced from Z. J. Guo et al., *Modeling, simulation and measurement of the dynamic performance of an ohmic contact, electrostatically actuated RF MEMS switch*, Journal of micromechanics and Microengineering, vol. 17, no. 9, page 1899, 2007, DOI: https://doi.org/10.1088/0960-1317/17/9/019. © 2007 IOP Publishing. Reproduced with permission. All rights reserved.

[5]↑ Reproduced from Sang Wook Lee et al., *A fast and low-power microelectromechanical system-based non-volatile memory device*, DOI: https://doi.org/10.1038/ncomms1227. Copyright © 2011 Sang Wook Lee et al. and licensed under a Creative Commons Attribution-NonCommercial-No Derivative Works 3.0 Unported License http://creativecommons.org/licenses/by-nc-nd/3.0/.

2. SOLVING MICROBEAM BOUNDARY VALUE PROBLEMS VIA CONTINUATION IN NONLINEAR MEMS DESIGN

The study of microbeam steady state behavior is commonplace in microelectromechanical system (MEMS) design, though only some simple devices are microbeams and have closed-form analytical solutions for their deflection behavior. However, strong nonlinear interactions in structural and multiphysics domains are pertinent for most interesting systems at this small scale, leaving researchers to decide between approximating the nonlinear behavior, making assumptions on the beam behavior, or exploring numerical modeling and solution algorithms. Numerical solutions are also often included to replace or supplement experimental observations even when they are not the basis of a research project. Thus, it is imperative for research groups studying MEMS design to have a carefully laid out approach to numerically solving microbeam boundary value problems (BVPs). The software package COMSOL Multiphysics® is commonly used to some extent in MEMS design, but its efficacy as a tool for parametric studies and continuation of solutions to determine static equilibria of these BVPs is much less utilized. In this chapter, COMSOL's numerical continuation capabilities are benchmarked against the more traditionally accepted nonlinear analysis software AUTO and explore these advanced functionalities through several relevant examples of increasing complexity.

2.1 Introduction

Microelectromechanical systems (MEMS) are powerful applications in modern engineering systems that utilize capacitive, piezoresistive, electrostatic, or thermoelectric phenomena involving devices for functioning and transducing at a small scale. Sensors benefit from the electrical component to measure mass or acceleration of their moving parts, while switches and memory cells benefit from the mechanical coupling to exploit deformation shapes or small-scale forces for novel applications. Regardless of the application, most MEMS devices experience nonlinear multiphysics phenomena and tend to have qualitative changes in system behavior while quasistatically varying parameters – whether actuation, material property, or geometry. Identifying this relationship between parameter modulation and system behavior

is the backbone to MEMS design, but there are several approaches available for solving static equilibria (final resting states) of their mechanically-deforming elements. MEMS devices can operate in static or dynamic domain though flexible structural elements do contribute to their dynamics. More and more operations of mems are in dynamic regime with fluctuating time-dependent force or electric inputs. In this chapter, the focus is on steady state behavior of MEMS, mostly for devices whose structural elements consist of beam-like elements.

An elementary approach to finding static equilibria in nonlinear MEMS is to assemble a dynamical model and simulate it via time-integration for a specific set of parameters at a particular actuation level until transient motions die out and the system settles to a rest at an equilibrium. For developing an understanding of the effect of actuation, one needs to then identify a neighboring equilibrium point, whereby the actuation level (or any system parameter) is increased or decreased by a sufficiently small (incremental) amount and the model is again simulated via time-integration until the system achieves equilibrium. This process only identifies stable equilibria though it is continued to fill out a set of parameters and the associated equilibria for the system. Unfortunately, there are drawbacks to this approach. First, the increment of step-size in parameter(s) is often large or the computation time tends to become prohibitively lengthy for systems with complicated models like multiple beams, patterned elements, or nonlinear multiphysics phenomena. Coarse step-sizes can be detrimental to identifying the location of novel equilibria features. Second, the solutions are restricted only to stable equilibria that can be reached from "quasistatic" changes to the system parameters. While it is reasonable to argue that identification of unstable equilibria is of lesser importance for many of the devices, it is the bifurcations and instabilities arising from the points where unstable and stable segments connect that are crucial to performance of systems with nonlinearities. An approach that solves for both stable and unstable solution branch segments could fare better at locating the transition points.

Over the last few decades, many computational packages with increasing algorithmic as well as multiphysics modeling sophistication have been developed for simulating and designing MEMS. The most versatile is COMSOL Multiphysics® [32], a popular finite element method (FEM) package championed for its expansive multiphysics module support.

In general, numerical continuation is the answer for this modeling; these techniques can identify system equilibria (both stable and unstable) and uncover the relationship between parameter changes and MEMS device behavior at a fraction of the computational cost of direct time-integration. By excluding the dynamical terms of an analytical model, this approach iteratively solves for equilibria directly. Herein is an introduction to the basics of numerical continuation and how it is achieved in two software packages: AUTO-07p Continuation and Bifurcation Software for Ordinary Differential Equations (AUTO) [33], a flagship algorithm in nonlinear dynamics communities for solving nonlinear static and dynamic parameter-dependent ordinary differential equation models for identifying static equilibria, periodic solutions, and bifurcations; as well as COMSOL Multiphysics®. While AUTO needs formulation of a model as a parametric boundary value problem (BVP), COMSOL Multiphysics® can solve systems with complicated boundary conditions involving multiphysics domains. This chapter collects and presents explorations into a variety of MEMS examples with various complexities in multiphysics and geometry of COMSOL Multiphysics® modeling. It is determined that COMSOL Multiphysics® is a suitable software package for numerical continuation in MEMS design, with few drawbacks that can be addressed in practice.

2.2 Methods

In outlining numerical continuation basics, one may follow the structure of Beyn et al. [34]. One starts with a dynamical system,

$$\frac{\partial x(t)}{\partial t} = f\left(x(t), \alpha\right), \quad x \in \mathbb{R}^n, f(x, \alpha) \in \mathbb{R}^n, \tag{2.1}$$

where x is a vector of length n, f is sufficiently smooth, and α denotes the continuation parameter of interest. Though the latter can be extended to evaluate multiple parameters, this chapter only covers the one-parameter family of solutions achieving codimension-1 bifurcations. The interest in continuation is to solve Equation (2.1) for equilibria,

$$f\left(x, \alpha\right) = 0. \tag{2.2}$$

The two basic evaluation procedures are *parameter continuation*, which follows equilibria through incremental steps in the parameter, and *pseudo-arclength continuation*, which follows equilibria through incremental steps along the path itself. Diagrams of each procedure are shown in Figure 2.1.

Parameter continuation: start with a solution x_0 of Eqn. (2.2) and its derivative $\left(\frac{\partial x}{\partial \alpha}\right)_0$ at α_0. To find solution x_1 at a neighboring parameter $\alpha_1 \equiv \alpha_0 + \Delta\alpha$, one solves $f(x_1, \alpha_1) = 0$ for x_1 by Newton's method,

$$f_x\left(x_1^{(\nu)}, \alpha_1\right) \Delta x_1^{(\nu)} = -f\left(x_1^{(\nu)}, \alpha_1\right), x_1^{(\nu+1)} = x_1^{(\nu)} + \Delta x_1^{(\nu)}, \forall\ \nu = 0, 1, 2, ..., n, \tag{2.3}$$

with $x_1^{(0)} = x_0 + \Delta\alpha \left(\frac{\partial x}{\partial \alpha}\right)_0$. The successive derivative vector $\left(\frac{\partial x}{\partial \alpha}\right)_1$ can be found via

$$f_x\left(x_1, \alpha_1\right) \left(\frac{\partial x}{\partial \alpha}\right)_1 = -f_\alpha\left(x_1, \alpha_1\right) \tag{2.4}$$

to continue evaluating successive equilibrium points, where f_x and f_α denote partial derivatives of function f with respect to x and α, respectively. The graphical representation of the procedure is shown in Figure 2.1a. While this is sufficient in the example continuation step from solution x_0 to solution x_1, the incremental stepping in parameter – as depicted by $\Delta\alpha$ – cannot continue to follow the equilibrium path once it reaches the point labeled TP.

Pseudo-arclength continuation: start with solution (x_0, α_0) of $f(x, \alpha) = 0$ and the normalized direction vector $\left(\left(\frac{\partial x}{\partial s}\right)_0, \left(\frac{\partial \alpha}{\partial s}\right)_0\right)$ at (x_0, α_0). To find solution (x_1, α_1), the equations of Keller's method can be employed [35],

$$f\left(x_1, \alpha_1\right) = 0,\ \left(x_1 - x_0\right)^T \left(\frac{\partial x}{\partial s}\right)_0 + \left(\alpha_1 - \alpha_0\right) \left(\frac{\partial \alpha}{\partial s}\right)_0 - \Delta s = 0, \tag{2.5}$$

where s is the arclength of the solution path. This is solved by Newton's method,

$$\begin{pmatrix} \left(f_x^1\right)^{(\nu)} & \left(f_\alpha^1\right)^{(\nu)} \\ \left(\frac{\partial x}{\partial s}\right)_0 & \left(\frac{\partial \alpha}{\partial s}\right)_0 \end{pmatrix} \begin{pmatrix} \Delta x_1^{(\nu)} \\ \Delta \alpha_1^{(\nu)} \end{pmatrix} = - \begin{pmatrix} f\left(x_1^{(\nu)}, \alpha_1^{(\nu)}\right) \\ \left(x_1^{(\nu)} - x_0\right)^T \left(\frac{\partial x}{\partial s}\right)_0 - \left(\alpha_1^{(\nu)} - \alpha_0\right) \left(\frac{\partial \alpha}{\partial s}\right)_0 - \Delta s \end{pmatrix}, \tag{2.6}$$

and the direction vector for the next solution point can then be found via

$$\begin{pmatrix} f_x^1 & f_\alpha^1 \\ \left(\frac{\partial x}{\partial s}\right)_0^T & \left(\frac{\partial \alpha}{\partial s}\right)_0 \end{pmatrix} \begin{pmatrix} \left(\frac{\partial x}{\partial s}\right)_1 \\ \left(\frac{\partial \alpha}{\partial s}\right)_1 \end{pmatrix} = \begin{pmatrix} 0 \\ 1 \end{pmatrix}. \tag{2.7}$$

The graphical representation of the procedure is shown in Figure 2.1b. Note the differences between this and *parameter continuation* of Figure 2.1a. The most glaring of which is through imagining what would happen at point TP. While *parameter continuation* falters, *pseudo-arclength continuation* continues to march on solving equilibria along the path beyond TP.

It is important to note that the resulting continuation curves are often comprised of both stable and unstable segments [36], the latter of which are generally unidentifiable in basic time-integration approaches to equilibria identification. However, the focus of this chapter is solely on the identification of static equilibria and not the nature of stability, instead leaving such a task for further dynamics analysis when necessary.

2.2.1 AUTO

Numerical continuation in AUTO is incorporated here as a benchmark to the following section of continuation in COMSOL Multiphysics®. It can employ continuation for algebraic systems, ordinary differential equations (ODEs), and some partial differential equations (PDEs), and also includes bifurcation identification, stability analysis, as well as periodic solutions when applicable. The software performs adaptive pseudo-arclength continuation for equilibria, while adaptively discretizing BVPs via orthogonal collocation with piecewise polynomials. From a user's perspective, the development of a problem in AUTO stems from a set of analytical functions; accessible for theory development yet cumbersome for nontraditional geometry. Starting with a PDE, eliminating the time dependent terms while maintaining the boundary conditions yields a boundary value problem (BVP) that can be represented in first order form for AUTO input. This process is showcased using two examples for benchmarking: a clamped-clamped microbeam actuated by a uniformly distributed

load and a cantilever (clamped-free) microbeam actuated by electrostatic load with surface interaction forces.

A clamped-clamped microbeam with initial curvature has the potential to exhibit bistability [36]. This is observed when the microbeam abruptly snaps through from one equilibrium configuration to another during a continuous change in loading. To explore this behavior in AUTO, one may start with a coupled PDE model [36], [37],

$$\begin{cases} \rho A\frac{\partial^2 u}{\partial t^2} - EA\frac{\partial^2 u}{\partial x^2} = \frac{1}{2}EA\frac{\partial}{\partial x}\left[w_0\frac{\partial \bar{w}}{\partial x}\frac{\partial w}{\partial x} + \left(\frac{\partial w}{\partial x}\right)^2\right] \\ \rho A\frac{\partial^2 w}{\partial t^2} + EI\frac{\partial^4 w}{\partial x^4} = EA\frac{\partial}{\partial x}\left[\left(\frac{\partial w}{\partial x} - w_0\frac{\partial \bar{w}}{\partial x}\right)\left(\frac{\partial u}{\partial x} - w_0\frac{\partial \bar{w}}{\partial x} + \frac{1}{2}(\frac{\partial w}{\partial x})^2\right)\right] + P(x) \end{cases} \tag{2.8}$$

and associated clamped-clamped boundary conditions (see Figure 2.2a for schematic), with lateral displacement w, initial shape $\bar{w}$ (normalized such that the maximum value is 1), maximum offset of initial shape w_0, axial displacement u, longitudinal position x, time t, Young's modulus E, area moment I, density ρ, cross sectional area A, second area moment of the cross section I, and uniformly distributed load $P(x) = P_0[H(x) - H(L - x)]$, where $H(x)$ is the Heaviside or step function and L is the length of the microbeam. Corresponding parameter values are given in Table 2.1, while the initial shape is chosen to be the first eigenfunction of a flat, clamped-clamped beam of similar properties [14]. Those who study transverse deflection of clamped-clamped beams may be more familiar with an uncoupled version of Equation (2.8) where the axial stretching of the PDE for u is incorporated into the PDE for w, but this is inconvenient for decomposition into a first order system for AUTO

input. Isolating only the static terms, Equation (2.8) can be rewritten in its equivalent first order form,

$$\begin{cases} \frac{d}{dx}\boldsymbol{u}_1 = \boldsymbol{u}_2 \\ \frac{d}{dx}\boldsymbol{u}_2 = w_0 \frac{d^2\bar{w}}{dx^2}\boldsymbol{w}_2 + w_0 \frac{d\bar{w}}{dx}\boldsymbol{w}_3 - \boldsymbol{w}_2\boldsymbol{w}_3 \\ \frac{d}{dx}\boldsymbol{w}_1 = \boldsymbol{w}_2 \\ \frac{d}{dx}\boldsymbol{w}_2 = \boldsymbol{w}_3 \\ \frac{d}{dx}\boldsymbol{w}_3 = \boldsymbol{w}_4 \\ \frac{d}{dx}\boldsymbol{w}_4 = -\frac{A}{I}\left(w_0 \frac{d^2\bar{w}}{dx^2} - \boldsymbol{w}_3\right)\left[\boldsymbol{u}_2 - w_0 \frac{d\bar{w}}{dx}\boldsymbol{w}_3 + \frac{1}{2}\left(\boldsymbol{w}_3\right)^2\right] + P_0 \end{cases} \tag{2.9}$$

where $\boldsymbol{u} = \left[u, \frac{\partial u}{\partial x}\right]$ and $\boldsymbol{w} = \left[w, \frac{\partial w}{\partial x}, \frac{\partial^2 w}{\partial x^2}, \frac{\partial w^3}{\partial x^3}\right]$. Numerical evaluation of static equilibria stemming from the undeformed $P, u, w = 0$ solution is performed with P_0 as the continuation parameter.

In the interest of exploring nonlinear continuation with multiphysics relevant to many MEMS devices, one may look at a microcantilever capacitive switch depicted in the schematic of Figure 2.3a [38]. Though no longer including the axial stretching of the clamped-clamped prior example, this switch can be modeled by the following PDE:

$$\rho A \frac{\partial^2 w}{\partial t^2} + EI \frac{\partial^4 w}{\partial x^4} = \frac{\varepsilon_0 b V^2}{2(a + \frac{d}{\varepsilon_r} - w)^2} + \frac{bH}{6\pi(a-w)^3}\left[1 - \left(\frac{z_0}{a-w}\right)^6\right], \tag{2.10}$$

and associated cantilever boundary conditions (clamped base, free tip), with permittivity of free space ε_0, beam width b, voltage potential V, undeflected gap a, dielectric thickness d, dielectric permittivity ε_r, Hamaker constant H, and zero pressure gap z_0. As with the prior

example, corresponding parameter values are given in Table 2.1. The system of Equation (2.10) is rewritten without time-dependent terms in its equivalent first order form,

$$\begin{cases} \frac{d}{dx}\boldsymbol{w}_1 = \boldsymbol{w}_2 \\ \frac{d}{dx}\boldsymbol{w}_2 = \boldsymbol{w}_3 \\ \frac{d}{dx}\boldsymbol{w}_3 = \boldsymbol{w}_4 \\ \frac{d}{dx}\boldsymbol{w}_4 = \frac{\varepsilon_0 b V^2}{2EI(a+\frac{d}{\varepsilon_r}-\boldsymbol{w}_1)^2} + \frac{bH}{6\pi EI(a-\boldsymbol{w}_1)^3}\left[1-\left(\frac{z_0}{a-\boldsymbol{w}_1}\right)^6\right]. \end{cases} \tag{2.11}$$

Numerical evaluation of static equilibria stemming from the undeformed beam at zero applied voltage is performed with V as the continuation parameter.

2.2.2 COMSOL Multiphysics®

Equilibrium analysis via COMSOL Multiphysics® is an accepted practice for nonlinear MEMS design, yet it is often achieved through time-integration solutions run for significant computation time until a system is deemed to reach "steady state". Understandably, this only allows researchers to identify a limited set of stable steady states (equilibria) uncovered by coarse steps in application of actuation voltage. COMSOL Multiphysics® is actually able to calculate static solution branches (both stable and unstable, though without distinction) via numerical continuation while drastically reducing computation time and revealing a more complete representation of the nonlinear behavior [39]. The software then brings substantial design space through the ability to analyze 1D, 2D, and 3D configurations containing exotic geometry, boundary conditions, and dozens of built-in or custom multiphysics. For the numerical continuation itself, it is most accessible to explore by way of *parameter continuation*, as the functionality of *pseudo-arclength continuation* is only achieved with additional algorithms [40].

The primary hurdle in setting up a COMSOL Multiphysics® model for *parameter continuation* is in finding a suitable continuation parameter to avoid any potential difficulties like that following around a point TP in the graphical depiction of Fig. 2.1a. By way of an additional constraint on the system, a monotonic function can be required to match an

arbitrary parameter that is swept through a set of values, thus making the function itself the guide through equilibria branches. This can be any function constructed within the vast array of software options, and not strictly a choice of one value from the model. For MEMS microbeam problems, it is often possible as to take the average displacement of the beam or the displacement of a judiciously-identified point along the beam as the monotonic function for an initial foray into static equilibria analysis. To implement this in the software, a global equation is defined such that the difference between the function and the arbitrary parameter is zero [39].

To benchmark against AUTO, numerical continuation is configured in COMSOL Multiphysics® for the clamped-clamped microbeam under uniformly distributed load with parameter values given in Table 2.1. Beam deflection is modeled using 1D Bernoulli-Euler beam theory, while the uniformly distributed load is assigned as a boundary load along the microbeam length. The monotonic continuation function is assigned as the average displacement of the microbeam.

In a follow-up to the microcantilever capacitive switch of the previous AUTO section, similar models are constructed in COMSOL Multiphysics® using the 1D, 2D, and 3D domain options [41]. Beam deformation in the 1D case is the usual Bernoulli-Euler, while electrostatics and surface-interaction forces are added with manual functions as beam loads. In 2D and 3D, the beam deformations are governed by evaluation of linear stress elements, electrostatic forces are determined by the surface Maxwell stress tensor, and the surface-interaction between the contacting features is still based on the same Lennard-Jones form of the final term in Equation (2.10). For the three capacitive switch examples, the average displacement of the microbeam is chosen as the continuation parameter.

As a final set of numerical continuation examples in COMSOL Multiphysics®, the inclusion of complex geometry within a 2D microcantilever capacitive switch model allows for a glimpse into the power of the approach beyond the benchmarking successes of prior examples. This is explored through three different patterning options available to current microfabrication processes: a patterned electrode, a patterned dielectric, and a patterned microcantilever underside. All three manipulate the electrostatics, but the latter two offer stark changes in the contact regions between the microcantilever and the dielectric layer. Patterns are

implemented by alternating fifths of the cantilever along its length, with thicknesses of the "removed" material pattern elements (for dielectric and microcantilever patterns) given in Table 2.1 along with other essential model parameters.

2.3 Results and Discussion

Nonlinear equilibrium behavior is well captured by the COMSOL Multiphysics® 1D model of the clamped-clamped microbeam with uniformly distributed load when compared to the AUTO benchmark. Numerical continuation solutions are shown alongside the associated schematic in Figure 2.2 for comparison. By imagining quasistatic operation of the system beginning from the undeflected initial shape, the basic performance of the device is revealed: continuous displacement increase with continuous uniformly distributed load up until the snap-through point, where the beam abruptly switches into a lower configuration, then the same situation but in reverse for the release back to the initial shape at zero applied actuation. Both the AUTO and COMSOL Multiphysics® 1D modeling solutions are in good agreement. Thus, COMSOL Multiphysics® has suitable qualitative and quantitative potential for exploring nonlinear equilibria via numerical continuation.

Benchmarking COMSOL Multiphysics® numerical continuation to that of AUTO extends to higher modeling dimensions with additional multiphysics phenomena. Solutions to the MEMS capacitive switch in AUTO and COMSOL Multiphysics® 1D, 2D, and 3D are provided in Figure 2.3d, while continuation step examples from the evaluation of 2D and 3D models are shown in Figures 2.3b and 2.3c, respectively. Four switching thresholds (pull-in, pull-down, pull-up, pull-out) are visible in this model versus only the two (snap-through, release) of the previous clamped-clamped configuration. This additional multistable behavior is driven by the nonlinear distributed force balance between the electrostatics and surface interaction forces along the length of the beam, which becomes critical in the post-touchdown configurations (i.e. microcantilever touching dielectric layer). When comparing the numerical continuation curves of the trio of COMSOL Multiphysics® models to that of AUTO, it is clear that the suitability of the COMSOL Multiphysics® approach extends to higher dimensions with nonlinear multiphysics and a free microbeam end boundary condition.

Finally, the real power and ease to using COMSOL Multiphysics® is evident when exploring numerical continuation solutions of systems with complicated geometry elements. Rather than finding suitable analytical elements to include in a PDE, material within the software domain can effectively be added or removed akin to the real fabrication processes used to create MEMS devices. The continuation solution curves for patterned electrodes, patterned dielectric layer, and patterned microcantilever underside models (all done in 2D) are provided in Figure 2.4, preceded by representative continuation step examples for each patterning. While some of the standard switch behavior presented in previous examples is still present, each patterning scheme has unique additional multistability exhibited in the highest actuation regime corresponding to the discontinuous nature of the relationship between the beam, dielectric layer, and/or underlying electrode(s).

2.4 Conclusion

Numerical continuation schemes allow MEMS practitioners to explore the nonlinear features present in the static equilibria of their devices, often with much greater speed than other limited techniques can offer. While researchers may choose to write their own numerical schemes to accomplish this task, the software packages of AUTO and COMSOL Multiphysics® are both well suited for such analysis in MEMS design. With a few drawbacks, COMSOL Multiphysics® can perform relevant numerical continuation for any multiphysics MEMS model assembled from its array of modules and built-in functions across one, two, or three spatial dimensions. Most device analysis and design benefit from understanding the underlying static equilibria.

Supplementary Information

Additional continuation step depictions are provided in Figures 2.5 to 2.9 for COMSOL Multiphysics® simulations of the microcantilever capacitive switch in 2D, the switch in 3D, the electrode patterned switch, the dielectric patterned switch, and the microcantilever patterned switch, respectively.

Table 2.1. Parameter values for numerical simulations

Parameter	Name	Value
ρ	Beam density (nickel)	8900 kg·m^{-3}
E	Beam elastic modulus (nickel)	219 GPa
	Beam Poisson's ratio (nickel)	0.31
L	Beam length	100 μm
h	Beam thickness	1 μm
b	Beam width	10 μm
w_0	Maximum value of initial shape	2 μm
H	Hamaker constant	1x10^{-21} J
z_0	Zero pressure gap	10 nm
a	Beam-dielectric gap (at tip)	1 μm
	Dielectric elastic modulus (silicon nitride)	250 GPa
	Dielectric Poisson's ratio (silicon nitride)	0.23
	Dielectric density (silicon nitride)	3100 kg·m^{-3}
ε_r	Dielectric relative permittivity (silicon nitride)	3.7
d	Dielectric thickness	100 nm
	Surrounding relative permittivity (nitrogen)	1
	Pattern element thickness	100 nm
ε_0	Permittivity of free space	8.85x10^{-21} F·m^{-3}

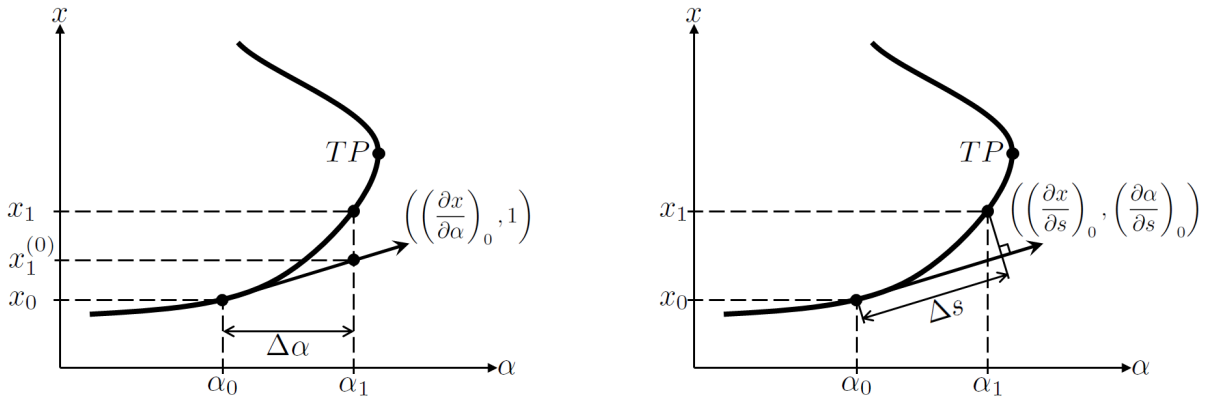

(a) (b)

Figure 2.1. Graphical representations for (a) *parameter* and (b) *pseudo-arclength continuation* based on similar figures of Beyn et al. [34].

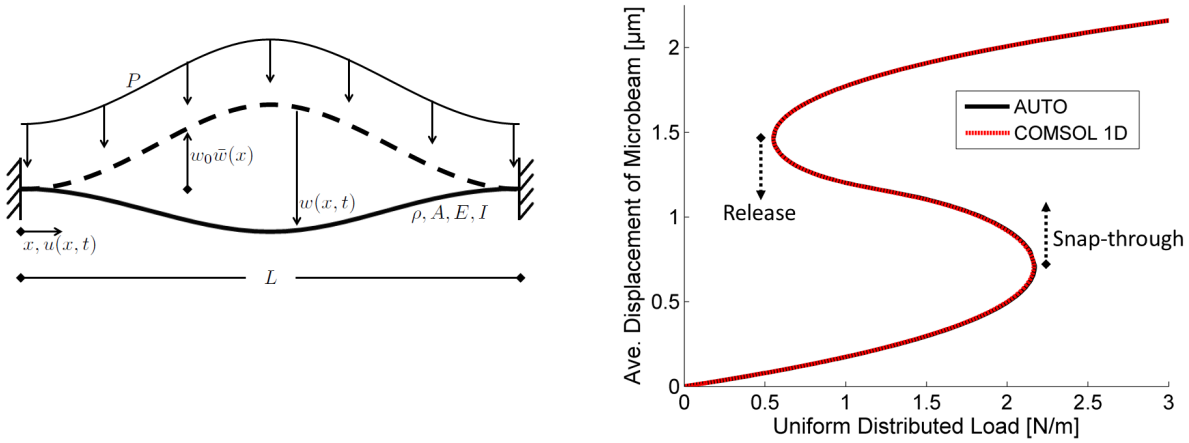

(a) (b)

Figure 2.2. Initially curved, clamped-clamped microbeam under uniformly distributed load. (a) Schematic detailing variables, parameters, loading, and boundary conditions. Variables indicate the uniformly distributed load P, the longitudinal location x, longitudinal displacement u, transverse displacement w, initial curvature $w_0\bar{w}$, density ρ, cross sectional area A, Young's modulus E, second area moment of cross section I, and beam length L. (b) Numerical continuation static equilibria results for AUTO and COMSOL Multiphysics® 1D. Snap-through and release instabilities identified.

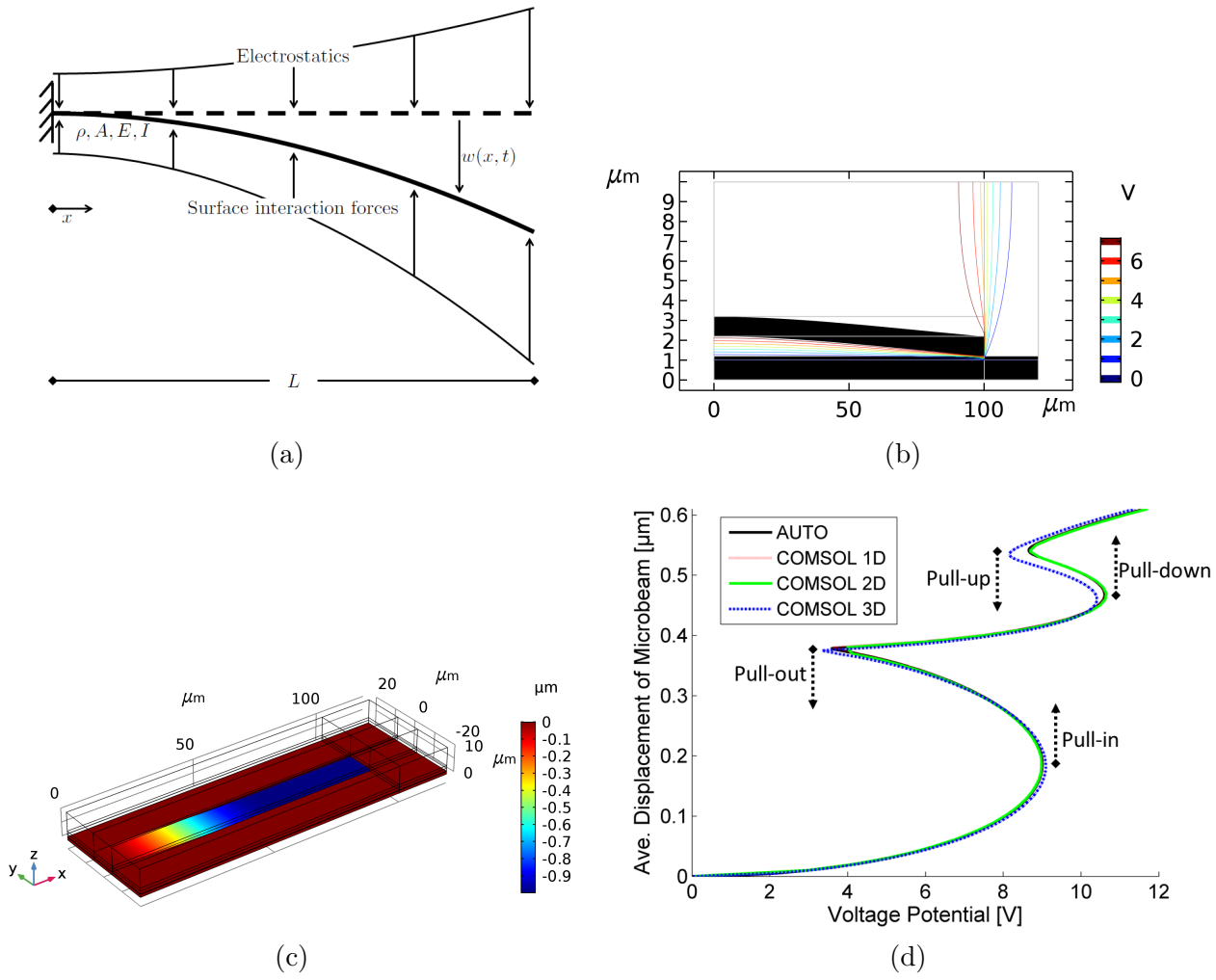

Figure 2.3. MEMS microcantilever capacitive switch with electrostatics and surface interaction forces [38], [41]. (a) Schematic indicating beam deflection, properties, external distributed forces, and beam boundary conditions. Variables denote the longitudinal position x, transverse displacement w, density ρ, cross sectional area A, Young's modulus E, second area moment of cross section I, and beam length L. (b) Numerical continuation step example for COMSOL Multiphysics® 2D model displaying microbeam deflection as well as (colored) contours for the electrostatic field. (c) Continuation step example for the 3D model showing (colored) displacements. (d) Collected static equilibria curves for AUTO as well as COMSOL Multiphysics® 1D, 2D, and 3D models for the capacitive switch, with additional labels for switching thresholds.

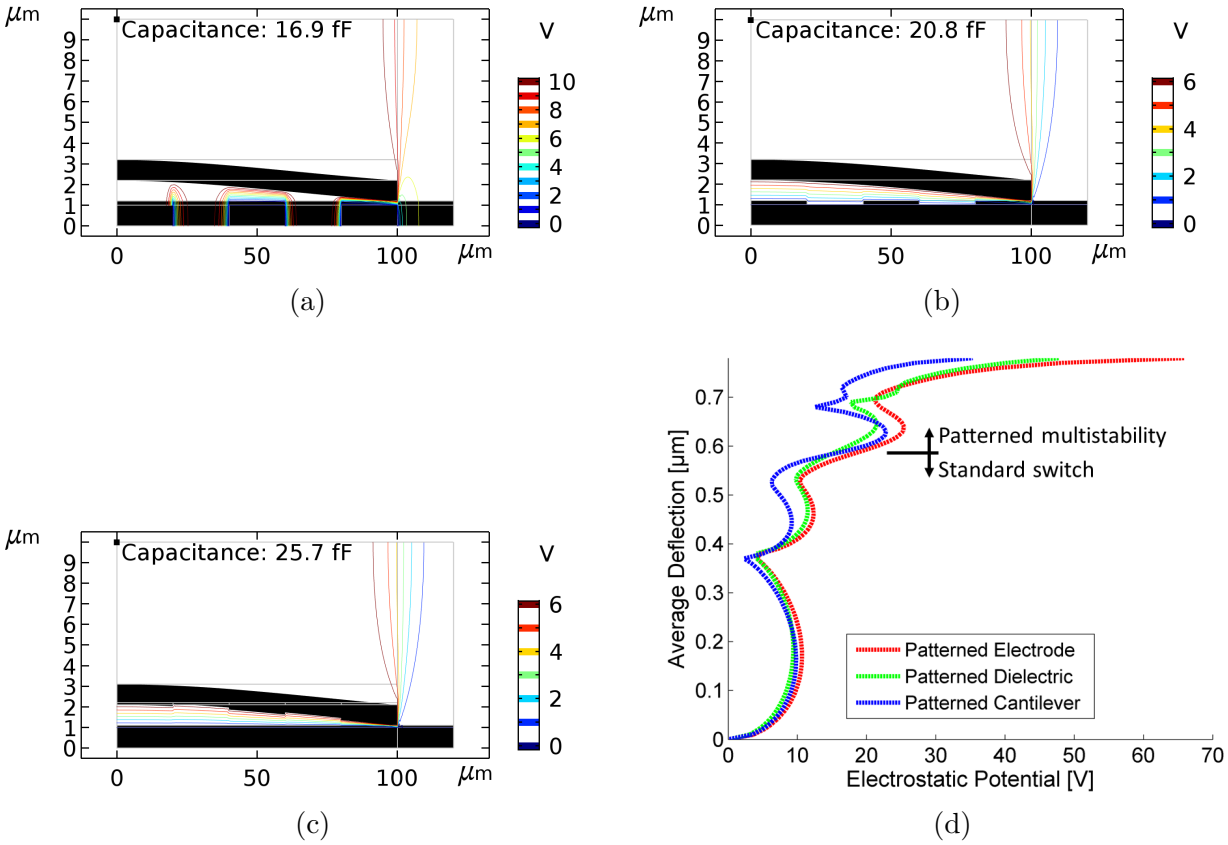

(a) (b) (c) (d)

Figure 2.4. Examples of complex geometry in COMSOL Multiphysics® 2D models through patterned elements of the standard MEMS microcantilever capacitive switch. (a)-(c) Patterning of electrodes, dielectric layer, and microcantilever underside, respectively. (d) Collected static equilibria curves from numerical continuation of the trio of patterning options; threshold indicator for previously-identified behavior of a standard capacitive switch versus the higher multistability regions of the patterned models.

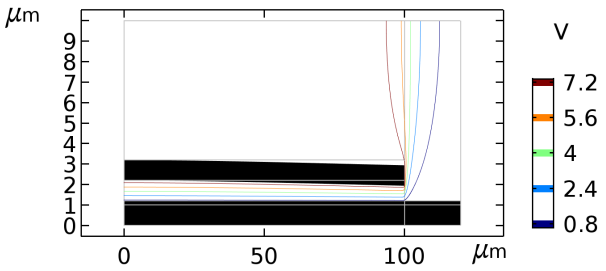

(a) Average displacement: 0.1 μm (floating)

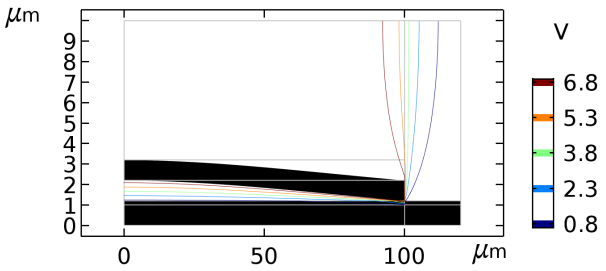

(b) Average displacement: 0.4 μm (arc-shaped)

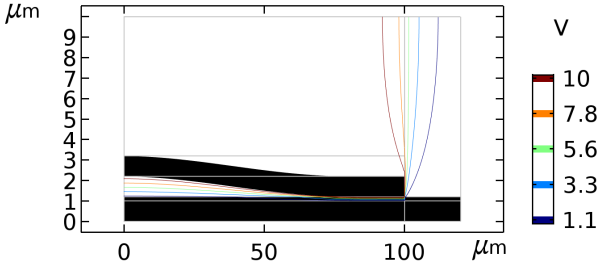

(c) Average displacement: 0.6 μm (s-shaped)

Figure 2.5. Microcantilever capacitive switch at various solution steps of the COMSOL Multiphysics® 2D model. Average displacement of the microcantilever is chosen to be the monotonic function for numerical continuation. Colored contour lines indicate electrostatic field between the microcantilever terminal and the lower electrode terminal. Parenthetical configuration shape labeling is consistent with that of Kalafut et al. [41].

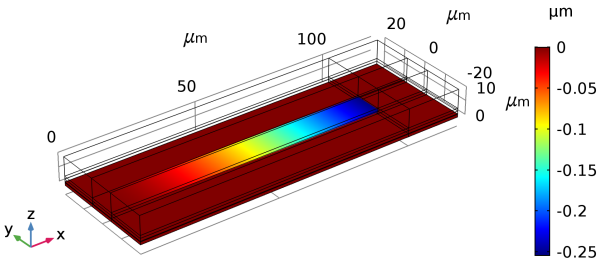

(a) Average displacement: 0.1 μm (floating)

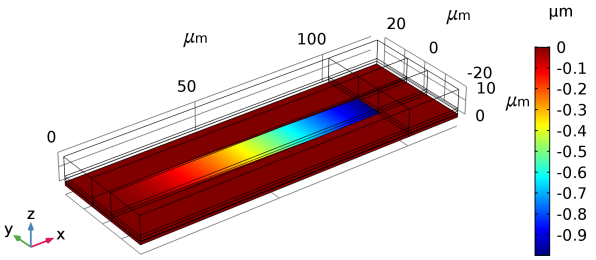

(b) Average displacement: 0.4 μm (arc-shaped)

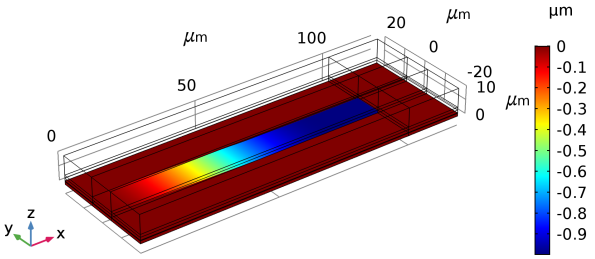

(c) Average displacement: 0.6 μm (s-shaped)

Figure 2.6. Microcantilever capacitive switch at various solution steps of the COMSOL Multiphysics® 3D model. Average displacement of the microcantilever is chosen to be the monotonic function for numerical continuation. Colored contour lines indicate electrostatic field between the microcantilever terminal and the lower electrode terminal. Parenthetical configuration shape labeling is consistent with that of Kalafut et al. [41].

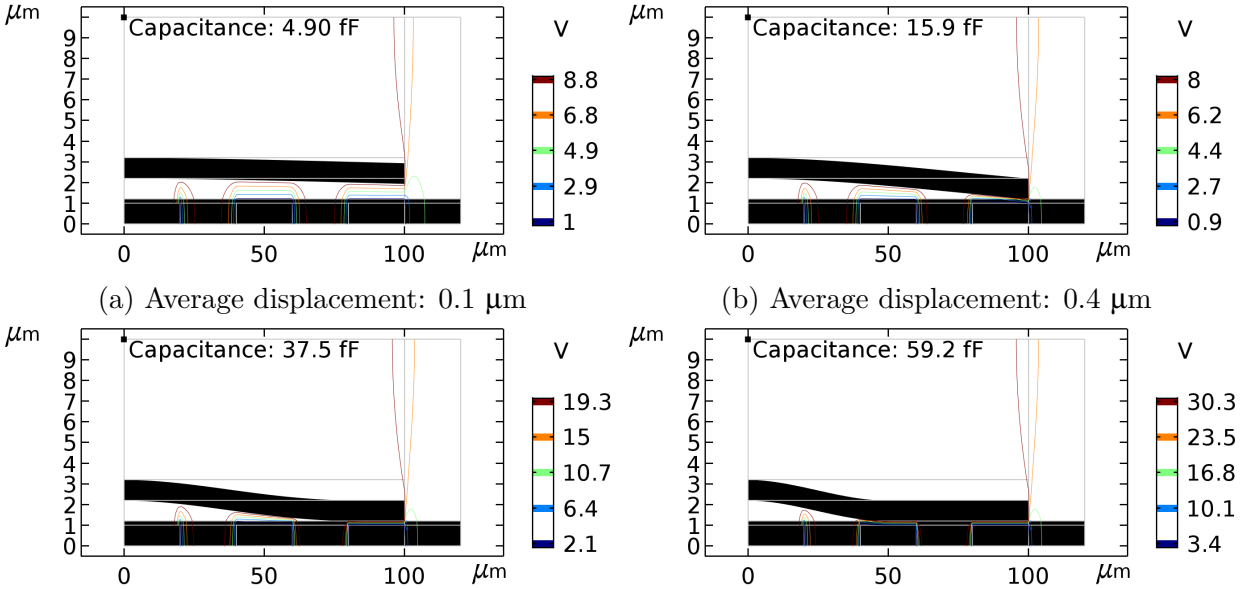

(a) Average displacement: 0.1 μm

(b) Average displacement: 0.4 μm

(c) Average displacement: 0.6 μm

(d) Average displacement: 0.75 μm

Figure 2.7. Microcantilever capacitive switch at various solution steps of the COMSOL Multiphysics® 2D model with electrode patterning. Average displacement of the microcantilever is chosen to be the monotonic function for numerical continuation. Colored contour lines indicate electrostatic field between the microcantilever terminal and the lower electrode terminal.

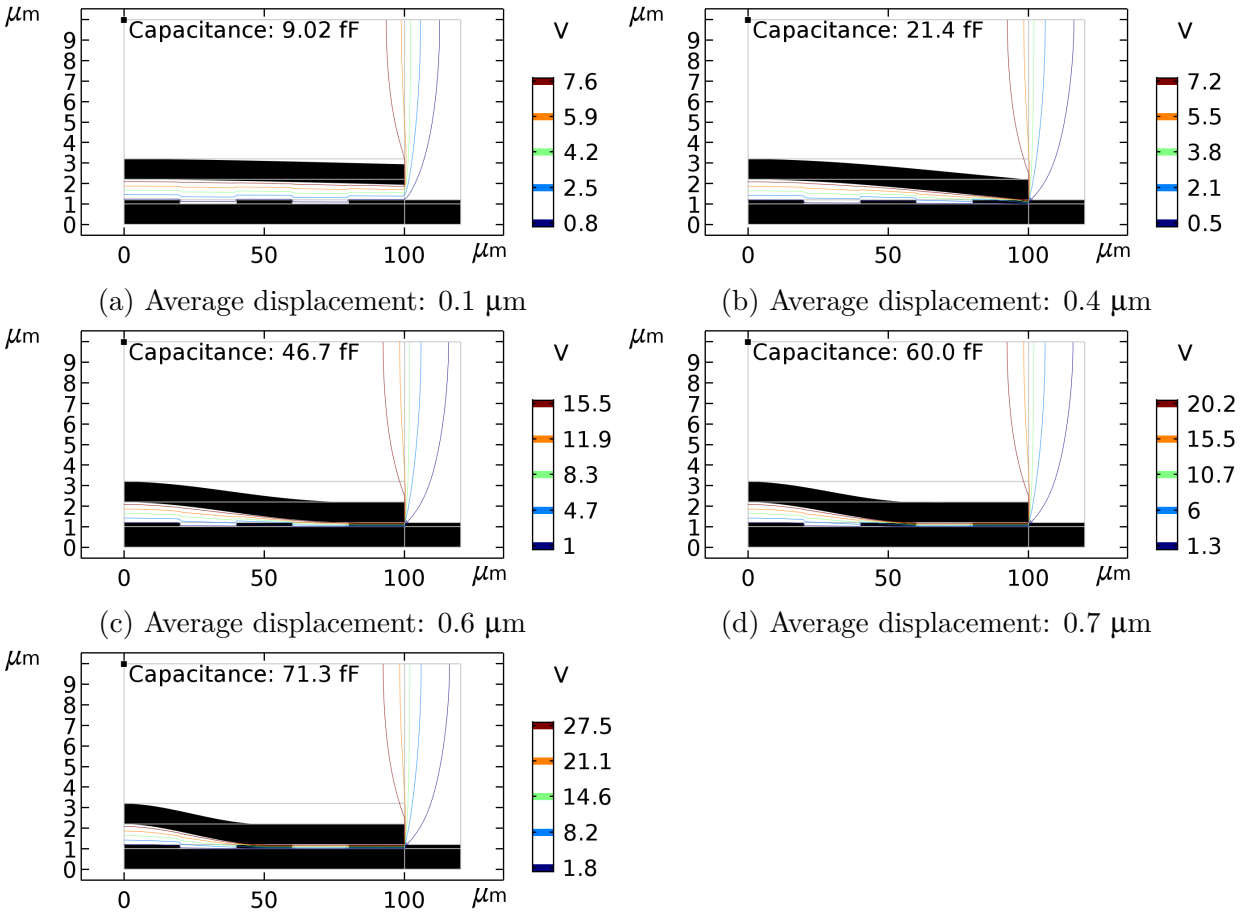

(a) Average displacement: 0.1 µm

(b) Average displacement: 0.4 µm

(c) Average displacement: 0.6 µm

(d) Average displacement: 0.7 µm

(e) Average displacement: 0.75 µm

Figure 2.8. Microcantilever capacitive switch at various solution steps of the COMSOL Multiphysics® 2D model with dielectric patterning. Average displacement of the microcantilever is chosen to be the monotonic function for numerical continuation. Colored contour lines indicate electrostatic field between the microcantilever terminal and the lower electrode terminal.

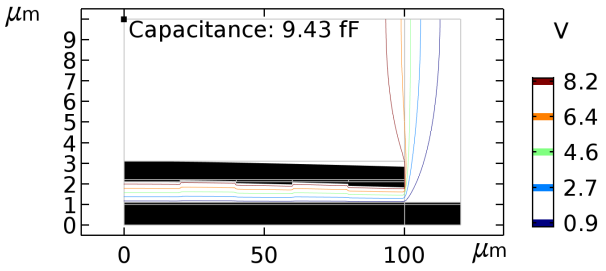

(a) Average displacement: 0.1 μm

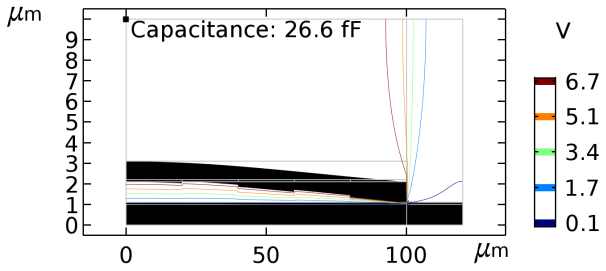

(b) Average displacement: 0.4 μm

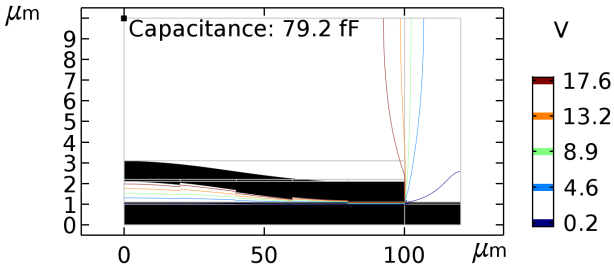

(c) Average displacement: 0.6 μm

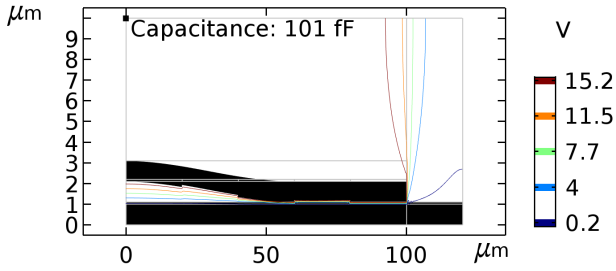

(d) Average displacement: 0.7 μm

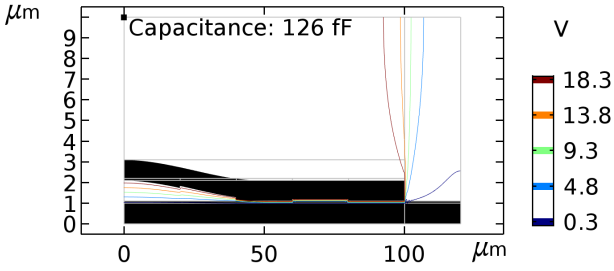

(e) Average displacement: 0.75 μm

Figure 2.9. Microcantilever capacitive switch at various solution steps of the COMSOL Multiphysics® 2D model with microcantilever underside patterning. Average displacement of the microcantilever is chosen to be the monotonic function for numerical continuation. Colored contour lines indicate electrostatic field between the microcantilever terminal and the lower electrode terminal.

3. MULTISTABILITY OF CANTILEVER MEMS/NEMS SWITCHES INDUCED BY ELECTROSTATIC AND SURFACE FORCES[1]

MEMS/NEMS switches are ideally bi-stable, with one ON and one OFF state and a reliable switching between the two induced by electrical actuation. Presented herein is an exploration into non-ideal behavior, i.e. tri-stability, and parametric sensitivity of a generalization of cantilever MEMS/NEMS switches. The representative system model employs multiphysics features based on Euler-Bernoulli beam theory, parallel plate capacitance for electrostatics, and a Lennard-Jones form of surface interaction. The geometry, material properties, and surface features of the device are condensed into just a few dimensionless quantities, creating a parameter space of low enough dimensionality to provide accessible representations of all system equilibria within physically relevant ranges. Analysis of this system model offers insight regarding conditions necessary for bi- and tri-stability in such systems, which are crucial for informing studies on switching dynamics and various device performance metrics.

3.1 Introduction

Investigations into failure modes, switching time and velocity, device reliability, and identification of critical actuation voltages for MEMS switches all require a sound knowledge of switching dynamics. The dynamics of switching in turn strongly depends on whether or not the switch behaves ideally, i.e. is bi-stable or tristable/multistable.

Prior literature is predominantly divided in emphasis between multistability and surface forces. Many past works focus on multistability without explicit inclusion of surface forces [15], [42]–[44], and tend to be interested in the relationship between the electrostatic forces and equilibrium positions. It is possible to identify more than two equilibrium positions in a capacitive switch model without surface forces, but the lack of such an attractive interaction restricts the breadth of multistability exhibited. Most importantly, any occurrence of stiction

[1]↑The findings of this chapter have been disseminated by the paper Kalafut et al. [38] published in the International Journal of Non-Linear Mechanics.

failure is unrealizable without adhesion. As shown in the current chapter, the precise nature of the surface interactions relevant to a device can completely change the stability behavior.

Conversely, various studies have analyzed van der Waals forces relevant to MEMS/NEMS switches, often in conjunction with Pauli repulsion in the Lennard-Jones potential, but without directly relating the results to multistability [23], [45]–[48]. This class of investigation aims to systematically understand the delicate balance of forces acting on the beam surface when near/in contact with the substrate below, and in some cases relate this information back to a specific instability. Independent implementations of these surface force models could each have their own nuances when identifying resulting multistable behavior, but the significance of their inclusion in capacitive switch modeling is universal.

More recently, some research groups have considered both surface forces and multistability in the context of specific device configurations. For example, Stulemeijer and co-workers analytically and experimentally identified equilibrium positions of a rectangular plate capacitive MEMS switch suspended by four spring-like supports, using an exponential form for the repulsive-only surface forces [40]. Additionally, they explored a range of complexity in device configuration, starting from a single degree of freedom representation. Results apply solely to their fit of experimental surface forces for a device, which alone has sufficient complexity in geometry and support configuration to restrict generality. Also, Ouakad and Younis studied the influence of capillary forces on instabilities of cantilever and clamped-clamped beams [21]. It is shown that capillary forces contribute to the attraction between the beam and the substrate, in turn influencing transitions from one stable equilibrium position to another.

In this chapter, common geometries and multiphysics models are employed to explore a dimensionless relationship between surface forces and multistability. The apparent simplicity of formulation serves to identify and classify static behavior intrinsic to a wide variety of cantilever capacitive switches. Furthermore, it serves as a foundation for continued modular study, where additive effects arriving due to initial beam curvature, electrostatic field fringing, finite electrodes, capillary forces, and surface roughness can be added conveniently. Also included is a brief Monte Carlo simulations based probabilistic analysis of the effect of parametric uncertainty on multistability, evaluated using independent realizations of random

inputs to calculate statistical moments [49]. While the same broad features exist, many critical points are highly susceptible to variation in parameters.

3.2 Theoretical Model

Cantilever MEMS/NEMS capacitive switches are fabricated with a small air gap between the beam and the dielectric-coated substrate, as shown in Figure 3.1(a) and Figure 3.2(b). Device operation is controlled by the electric potential applied between the metallic beam and underlying electrode beneath the dielectric. An example electrode configuration is depicted in Figure 3.1(b). When a high enough potential is applied for a given configuration, it is possible for the deflecting beam to come into contact with the dielectric. Thus, both electrostatic and surface forces between the two solid materials play key roles in determining final resting states and shapes of the cantilever, and, in turn, the overall capacitance of the device.

For each contributing force interaction in the model, a simple formulation is chosen to capture the most basic behavior relevant to the analysis. Electrostatic interaction between the beam and lower electrode is represented as a series of infinitesimal parallel plate capacitors creating a force per unit length along the beam that depends on local gap. Here, as in Figure 3.1(a), $\hat{w}(\hat{x},\hat{t})$ is the deflection at a given distance along the length of the beam $\hat{x}$, and at time $\hat{t}$. The beam thickness b, applied voltage $\hat{V}$, undeflected/fabricated air gap a, and dielectric thickness d can also be identified. Not shown are the dielectric constant ϵ_r, and the permittivity of free space ϵ_0, a known constant. The assumption with regard to the parallel plate model is of greater validity for wider beams, as narrower ones will have a larger proportion of their electrostatic fields affected by fringing. Various models exploring the significance of this electrostatic field fringing due to both the beam geometry and orientation of finite electrodes add complexity [16], [50], [51], and can easily be included in the present analysis. In this chapter, fringing fields are not included since the general features of multistability are not affected qualitatively by their inclusion. Additionally, it has been noted that the contributions due to field fringing are small when the beam is close to the dielectric, which is relevant to certain beam configurations [15]. This approach aligns with the theme of exploring rich multistable behavior within a generalized model for this

class of devices. Thus, the per-unit-length force representation of electrostatics is modeled as:

$$F_{electrostatic} = \frac{\epsilon_0 b \hat{V}^2}{2(a + \frac{d}{\epsilon_r} - \hat{w}(\hat{x}, \hat{t}))^2} \tag{3.1}$$

Surface interactions between the deflecting beam and the dielectric below are modeled using an extension of the 9-3 Lennard-Jones potential [52], [53], which is often used to model attractive-repulsive interactions of two interacting solid surfaces. With two perfectly flat surfaces interacting, the $\hat{H}$ and the $\hat{z}_0$ represent material properties known as the Hamaker constant and the zero-pressure gap, respectively. In literature, the zero-pressure gap is taken to be 0.5 nm [53], and is described as the gap between two interacting solid surface elements at which no net pressure is exerted. This notion is generalized to a per-unit-length interaction force that is derived by assuming that these forces depend on the local gap [54]. Thus, the per-unit-length force representation of the surface interaction is assumed as:

$$F_{surface} = \frac{b\hat{H}}{6\pi(a - \hat{w}(\hat{x}, \hat{t}))^3} \left[1 - \left(\frac{\hat{z}_0}{a - \hat{w}(\hat{x}, \hat{t})}\right)^6\right]; \tag{3.2}$$

The dominant features of the force-gap curve are the attraction (positive values), the zero-pressure gap (gap at which the curve crosses the zero-force axis), the repulsion (negative values), and the dramatic reduction in force as the beam is further away from the dielectric. More realistic effects, such as surface roughness and capillary adhesion, merit inclusion in interaction models [18], [55]. Specifically, roughness serves to reduce the cumulative energy of van der Waals adhesion [56], though the Lennard-Jones potential is still of significance when tracking net interaction between the mean planes of rough surfaces [47]. Therefore, the assumption of perfect smoothness of the interacting surfaces can be considered a worst-case scenario with regard to dry stiction failures. Conversely, capillary forces work to increase adhesion energy, and can be conveniently incorporated as an additional term to expand the surface interaction model complexity [21]. It is assumed that both the beam and the dielectric surfaces are smooth, since it provides a starting point for including surface forces in a systematic way in MEMS/NEMS switch models. Alternatively, $\hat{z}_0$ and $\hat{H}$ could be viewed as fitting parameters to experimental force-gap curves to circumvent the addition of

extra modules for other physical interactions, but the consequences of this approach are not explicitly explored herein.

After combining suggested submodels in a force balance with Euler-Bernoulli beam theory, appropriate for long, thin cantilevers [14], the resulting equation of motion for the cantilever beam system is a PDE as follows:

$$EI\frac{\partial^4 \hat{w}}{\partial \hat{x}^4} + \rho A\frac{\partial^2 \hat{w}}{\partial \hat{t}^2} = \frac{\epsilon_0 b\hat{V}^2}{2(a+\frac{d}{\epsilon_r}-\hat{w})^2} + \frac{b\hat{H}}{6\pi(a-\hat{w})^3}\left[1-\left(\frac{\hat{z}_0}{a-\hat{w}}\right)^6\right], \tag{3.3}$$

which includes the elastic modulus E, area moment $I = \frac{1}{12}bh^3$, density ρ, and beam cross-sectional area $A = b*h$. The beam length is assumed to be fixed throughout the comparatively small deflections, so there is no inclusion of a geometric nonlinearity term for axial stretching.. By introducing nondimensional quantities

$$w = \frac{\hat{w}}{a}, x = \frac{\hat{x}}{L}, t = \frac{\hat{t}}{T}, T = \sqrt{\frac{\rho AL^4}{EI}} \tag{3.4}$$

and

$$V = \frac{\epsilon_0 bL^4\hat{V}^2}{2EIa^3}, g = \frac{{}^{d}/_{\epsilon_r}}{a}, z_0 = \frac{\hat{z}_0}{a}, H = \frac{bL^4\hat{H}}{6\pi EIa^4}, \tag{3.5}$$

the resulting non-dimensional equation of motion is

$$\frac{\partial^2 w}{\partial t^2} + \frac{\partial^4 w}{\partial x^4} = \frac{V}{(1+g-w)^2} + \frac{H}{(1-w)^3}\left[1-\left(\frac{z_0}{1-w}\right)^6\right], \tag{3.6}$$

with boundary conditions on the fixed end:

$$w|_{x=0} = 0, \left.\frac{\partial w}{\partial x}\right|_{x=0} = 0, \tag{3.7}$$

and those at the free end:

$$\left.\frac{\partial^2 w}{\partial x^2}\right|_{x=1} = 0, \left.\frac{\partial^3 w}{\partial x^3}\right|_{x=1} = 0. \tag{3.8}$$

In Equations (3.6) to (3.8), it is assumed that the elastic modulus E and area moment I do not vary along the length of the beam x, and thus do not contribute to respective partial

derivatives stemming from evaluating the bending moment and shear force at the cantilever tip. Furthermore, by only including terms relevant to statics, Equation (3.6) becomes

$$\frac{\partial^4 w}{\partial x^4} = \frac{V}{(1+g-w)^2} + \frac{H}{(1-w)^3}\left[1 - \left(\frac{z_0}{1-w}\right)^6\right], \tag{3.9}$$

with the same boundary conditions as in Equations (3.7) and (3.8). Notice how this final form for the static behavior of the device is a BVP of an ODE, and only depends on the four dimensionless quantities introduced in Equation (3.5). This is the basis of further analysis.

3.3 Computational Approach

Multiple equilibria arise directly from solving Equations (3.7) to (3.9), while an additional parametric sensitivity analysis serves to quantify basic uncertainty in the findings. To represent solutions concisely, a dimensionless capacitance is defined as:

$$C = \int_0^1 \frac{1}{1+g-w} \mathrm{d}x, \tag{3.10}$$

which is both a scalar metric for the deflection of the beam and the device output quantity of interest. One-dimensional continuation in V of Equations (3.7) to (3.9) is handled in AUTO, the Continuation and Bifurcation Analysis software, to provide equilibrium solutions in terms of C [33]. Details regarding the equations, parameters, and tolerances used to run the AUTO continuation are given in Appendix A, while a set of example results are shown in Figure 3.2(a).

The stable and unstable segments of a branch are marked in solid and dashed lines, respectively, in the example of Figure 3.2(a), with details of the analysis given in Appendix B. With stability identified, it is clear that there are three stable solution segments isolated by unstable sections and existing within separate bands of dimensionless capacitance; these are the three configuration shapes depicted in Figure 3.2(b). Though sourced in this continuation solution methodology under distributed forces and fixed-free boundary conditions, these configurations have a similar appearance to those found by varying tip boundary conditions between free, pinned, and fixed [15]. As such, notation from literature is followed in denoting

the stable equilibrium shapes as either floating (low C), arc-shaped (medium C), or s-shaped (high C) [15], [57].

Additionally, the turning points themselves are labeled in Figure 3.2(a) with regard to varying the dimensionless actuation. The pull-in instability refers to the loss of the floating stable beam shape with increasing V, above which the only equilibria possible are the arc- and s-shapes. Similarly, the pull-down instability corresponds to the loss of the arc-shape equilibrium with increasing V. Then, on withdrawal, the pull-up and pull-out instabilities describe the loss of s-shaped and arc-shaped equilibria, respectively, with decreasing V. This understanding provides the basis upon which dynamic switching simulations would take place.

As turning points are determined from a given set of parameters, their locations on the C-V plane vary under any uncertainty embodied in the dimensionless parameters. To perform a basic Monte Carlo analysis for investigating the effects of parameter variability, reasonable distributions are assumed for geometric parameters a and d. Distributions and values chosen are as follows:

$$\begin{cases} a \sim \text{Normal distribution of 1 } \mu\text{m mean and 0.1 } \mu\text{m standard deviation,} \\ d \sim \text{Normal distribution of 100 nm mean and 10 nm standard deviation,} \\ z_0 = 0.5 \text{ nm,} \\ \epsilon_r = 2. \end{cases} \tag{3.11}$$

Since these are combined in the dimensionless parameters of Equation (3.5), other mathematically equivalent example sets could be chosen so long as the ratios between nominal values as well as the ratios between the means and standard deviations are preserved. Independent realizations from these distributions are used in separate continuation runs, and the outcomes are collected to define the mean and standard deviations of the critical instability points.

3.4 Results

Across the wide parameter space discussed, the stable, static equilibrium shapes fall into a variety of multistability categories – whether the given cantilever MEMS/NEMS

capacitive switch is mono-, bi-, or tristable – depending on specific values of the dimensionless parameters from Equation (3.5). Several sets of z_0 and g values are shown in the multistability diagrams of Figure 3.3, where both the multistability regions and their instability boundaries are labeled. For example, Figure 3.3(a) depicts tri-stability between the pull-up and pull-in boundaries, in which floating, arc-shaped, and s-shaped stable, static equilibria are realizable. In the same figure, there exist various regions of mono- and bi-stability, depending on V and H. To compare diagrams within Figure 3.3, only z_0 is increased by a factor of 10 between (a) and (c), while their counterparts in (b) and (d) have double the value for g.

Following the example distributions outlined in Equation (3.11), results of the Monte Carlo analysis are given in Figure 3.4. Statistical means and standard deviations for the V values of each instability point are calculated along fixed H values, or vertical lines, in the chosen multistability diagram. Mean values (solid black) are labeled, and nominal values (dashed white) are included, corresponding to $z_0 = 0.0005$ and $g = 0.05$ as in Figure 3.3(a). The shaded regions represent two standard deviations both above and below respective means, while the accompanying histogram insets depict cross sections of the 1000 Monte Carlo realizations at several example points.

3.5 Discussion

As cantilever capacitive switches are clearly not simple ON/OFF devices under various physically realizable conditions, identification of the pull-in instability alone is not necessarily sufficient to inform switch closure – nor is that of the pull-up instability for switch opening. This comes directly from the possibility of the intermediate arc-shaped equilibrium configuration, whose effect on static behavior is substantial. This is best shown via Figure 3.2(a). For example, a device in the floating configuration at $V = 0$, which corresponds to zero applied voltage, is at its lowest capacitance (OFF state). As V is increased past the pull-in point, the device could switch into either the arc- or s-shaped configuration, depending on the transient dynamics. If it does rest in the arc-shape, another transition occurs with increasing V after the pull-down point, above which the device will come to rest in the s-shape configuration. A similar set of behavior can take place on release with decreasing V crossing the pull-up and

pull-out points, but it is possible to have sets of parameters for which one or both of these instabilities exist at negative V values, which are not physically realizable. This corresponds to stiction failure in either the arc- or s-shaped configuration, where the device does not release into the lowest capacitance state, even as the electrostatic actuation is removed.

Extension of the stiction behavior across wider parameter variety can be seen in the pull-up and pull-out intersections along the $V = 0$ axis of each plot in Figure 3.3. By comparing the top set to the bottom set, it is apparent in this example that an increase in z_0 by an order of magnitude requires an increase in H values of approximately two orders of magnitude for the same stiction failures. It is important to note that this is not a simple result of the nondimensionalization in Equation (3.5). While the undeflected air gap a is common to both z_0 and H, the differences in stiction thresholds are not appropriately captured by algebraic manipulation of this value.

Interestingly, many of the general multistability features exist as $H \to 0^+$. In examining this left axis in the examples of Figure 3.3, each of the three equilibrium configurations of Figure 3.2(b) are realizable under various parameter sets. Thus, the existence of equilibrium shapes is a consequence of the nonlinear electrostatics and repulsion, but does not explicitly require adhesion. There is no observance of stiction, though, which is understandably related to adhesive forces in the absence of electrostatic actuation. Furthermore, a comparison of the right sets of plots to the left in Figure 3.3 reveals the influence of doubling g on the corresponding V values for each instability as $H \to 0$. As d is unique to this dimensionless parameter, the increase in V needed to transition across instability points could be attributed to a doubling of this dielectric thickness.

Finally, the example uncertainty quantification results of Figure 3.4 provide insight into the dependence of multistability on parameter variability. While the statistical mean lines of the instability thresholds do not appear appreciably different than their nominal counterparts in Figure 3.3(a), the statistical variances contribute important information. The narrow regions of two standard deviations above and below the pull-in and pull-out instabilities suggest robustness against uncertain z_0 and g. Conversely, the pull-down and pull-up instabilities have much wider regions of parameter space covered by similar standard deviations, and as such are more sensitive to z_0 and g, as informed by the prescribed distributions for

a and d in Equation (3.11). With regard to stiction failure at $V = 0$, the width of the pull-up and pull-out standard deviation regions are prominent, suggesting strong sensitivity to the uncertain parameters. Furthermore, while the nominal lines and inset histograms of Figure 3.4 are provided for completeness, the slight non-Gaussian appearance of the results may be attributed to the nonlinear nature of the system. A more exhaustive uncertainty quantification study would be required for appropriate justification.

3.6 Conclusion

Multistability regions and instability boundaries are identified in dimensionless parameter space, and the instability sensitivity for the dimensionless parameters is studied. Under the defined methodology, cantilever MEMS/NEMS capacitive switches exhibit mono-, bi-, and tri-stability in physically realizable conditions when even the most innate Lennard-Jones surface interaction model is included and varied. Results provide an easily-expandable framework for exploration of the coupling between multistability and surface interactions, with relevance to the design and performance of such devices.

3.A Numerical Continuation Scheme

To implement Equations (3.7) to (3.9) in AUTO, they are converted to a first-order form as follows, where $u_1(x) = w(x,t)$, and $'$ denotes derivate with respect to x:

$$\begin{cases} u_1 = f_1(u_1,u_2,u_3,u_4) = u_2, \\ u_2 = f_2(u_1,u_2,u_3,u_4) = u_3, \\ u_3 = f_3(u_1,u_2,u_3,u_4) = u_4, \\ u_4 = f_4(u_1,u_2,u_3,u_4) = \dfrac{V}{(1+g-u_1)^2} - \dfrac{H}{(1-u_1)^3}\left[1-\left(\dfrac{z_0}{1-u_1}\right)^6\right], \end{cases} \tag{3.12}$$

$$\begin{cases} f_{B1}(u_1, u_2, u_3, u_4) = u_1(0), \\ f_{B2}(u_1, u_2, u_3, u_4) = u_2(0), \\ f_{B3}(u_1, u_2, u_3, u_4) = u_3(1), \\ f_{B4}(u_1, u_2, u_3, u_4) = u_4(1). \end{cases} \tag{3.13}$$

The four governing equations and associated four boundary equations in Equations (3.12) and (3.13) can be reduced to a single expression that is solved via AUTO:

$$\boldsymbol{F}(u_1, u_2, u_3, u_4) = \mathbf{0}, \tag{3.14}$$

where $\boldsymbol{F} = [f_1, f_2, f_3, f_4, f_{B1}, f_{B2}, f_{B3}, f_{B4}]^T$. Following the prescribed framework for BVPs, the ODE is discretized by the method of orthogonal collocation through the use of piecewise polynomials [58]. Stemming from the known, unactuated, (nearly) undeflected beam configuration, computed solutions are iteratively driven to match at each of the collocation points distributed along the length of the beam. Under minimal tolerances, the procedure marches on to discover equilibrium beam shapes corresponding to V values. Results are finally distilled onto into the C-V plane for convenience.

For proper execution, parameters and tolerances within AUTO must be tuned for the specific model. Definitions of each term are provided in the software manual accompanying AUTO distributions, but the values used for this analysis are as follows:

NDIM=4, IPS=4, IRS =0, ILP =1, SP=['LP4','HB0','BP0']

ICP=[1]

NTST=100, NCOL=4, IAD=3, ISP=2, ISW=1, IPLT=0, NBC=4, NINT=0

NMX=15000, NPR=0, MXBF=10, IID=2, ITMX=8, ITNW=5, NWTN=3, JAC=0

EPSL=1e-8, EPSU=1e-8, EPSS=1e-5

DS=1e-6, DSMIN=1e-20, DSMAX=1e-2, IADS=1

NPAR=15, THL={}, THU={}

UZR={}

UZSTOP={}

3.B Stability of Equilibria

Stability of equilibrium solutions can be identified via an eigenvalue problem constructed from a spatial discretization of Eqns.(3.6) to (3.8). Here, the beam is divided into N evenly-spaced finite difference nodes, denoted $x_1, x_2, ..., x_N$, separated by Δx, with associated deflections $w_\mathrm{i} = w(x_\mathrm{i}, t)$. Then, with $'$ designating derivatives with respect to x, finite difference approximations are constructed as:

$$\begin{cases} w_2 & = & \frac{1}{(\Delta x)^4}\left(12w_2 - 6w_3 + \frac{4}{3}w_4\right) \\ w_3 & = & \frac{1}{(\Delta x)^4}\left(-4w_2 + 6w_3 - 4w_4 + w_5\right) \\ w_k & = & \frac{1}{(\Delta x)^4}\left(w_{k-2} - 4w_{k-1} + 6w_\mathrm{i} - 4w_{k+1} + w_{k+2}\right), k = 4, 5, 6, ..., N-2 \\ w_{N-1} & = & \frac{1}{11(\Delta x)^4}\left(12w_{N-3} - 48w_{N-2} + 60w_{N-1} - 24w_N\right) \\ w_N & = & \frac{1}{7(\Delta x)^4}\left(12w_{N-2} - 24w_{N-1} + 12w_N\right). \end{cases} \tag{3.15}$$

While the w_k equation is a common central difference scheme, the four remaining definitions come from Taylor series expansions at the grid boundaries which are designed to include the fixed and free boundary conditions of Equations (3.7) to (3.8) [59], [60]. Since there is no motion at the point w_1 of the fixed cantilever base, there is no need to evaluate a fourth-order partial derivative at that location.

Substituting Equation (3.15) into Equation (3.6) results in:

$$\frac{d^2 w_\mathrm{i}}{dt^2} = -w_\mathrm{i} + \frac{V}{(1 + g - w_\mathrm{i})^2} + \frac{H}{(1 - w_\mathrm{i})^3}\left[1 - \left(\frac{z_0}{1 - w_\mathrm{i}}\right)^6\right], \tag{3.16}$$

valid for $\mathrm{i} = 2, ..., N$, which is a reduction from the infinite-dimensional spatial continuum to a finite set of N nodes. Denoting the right hand side of Equation (3.16) as RHS_i, a further decomposition and linearization yields a system of first order linear ODEs as follows:

$$\dot{\boldsymbol{w}} = \boldsymbol{A}\boldsymbol{w} \tag{3.17}$$

where

$$\boldsymbol{w} = \begin{Bmatrix} w_2 & \dot{w}_2 & w_3 & \dot{w}_3 & \cdots & w_N & \dot{w}_N \end{Bmatrix}^T \tag{3.18}$$

and

$$\boldsymbol{A} = \begin{Bmatrix} 0 & 1 & 0 & 0 & \cdots & 0 & 0 \\ \frac{\partial \mathrm{RHS}_2}{\partial w_2}\big|_{\boldsymbol{w_0}} & 0 & \frac{\partial \mathrm{RHS}_2}{\partial w_3}\big|_{\boldsymbol{w_0}} & 0 & \cdots & \frac{\partial \mathrm{RHS}_2}{\partial w_N}\big|_{\boldsymbol{w_0}} & 0 \\ 0 & 0 & 0 & 1 & \cdots & 0 & 0 \\ \frac{\partial \mathrm{RHS}_3}{\partial w_2}\big|_{\boldsymbol{w_0}} & 0 & \frac{\partial \mathrm{RHS}_3}{\partial w_3}\big|_{\boldsymbol{w_0}} & 0 & \cdots & \frac{\partial \mathrm{RHS}_3}{\partial w_N}\big|_{\boldsymbol{w_0}} & 0 \\ \vdots & \vdots & \vdots & \vdots & \ddots & \vdots & \vdots \\ 0 & 0 & 0 & 0 & \cdots & 0 & 1 \\ \frac{\partial \mathrm{RHS}_N}{\partial w_2}\big|_{\boldsymbol{w_0}} & 0 & \frac{\partial \mathrm{RHS}_N}{\partial w_3}\big|_{\boldsymbol{w_0}} & 0 & \cdots & \frac{\partial \mathrm{RHS}_N}{\partial w_N}\big|_{\boldsymbol{w_0}} & 0 \end{Bmatrix}. \tag{3.19}$$

Here, $\boldsymbol{w_0}$ refers to an equilibrium solution for the ensemble of finite difference nodes. Though the continuation of the BVP of Equations (3.7) to (3.9) is handled in AUTO, the associated equilibrium solution for the finite difference discretization is taken to be a cubic spline interpolation of such continuation results for a chosen grid density.

Solutions to the eigenvalue problem $\lambda \boldsymbol{v} = \boldsymbol{A}\boldsymbol{v}$ indicate the stability at each equilibrium configuration. Any λ with a positive real component is associated with an unstable equilibrium, while an equilibrium with purely imaginary components is considered neutrally stable under this linearization.

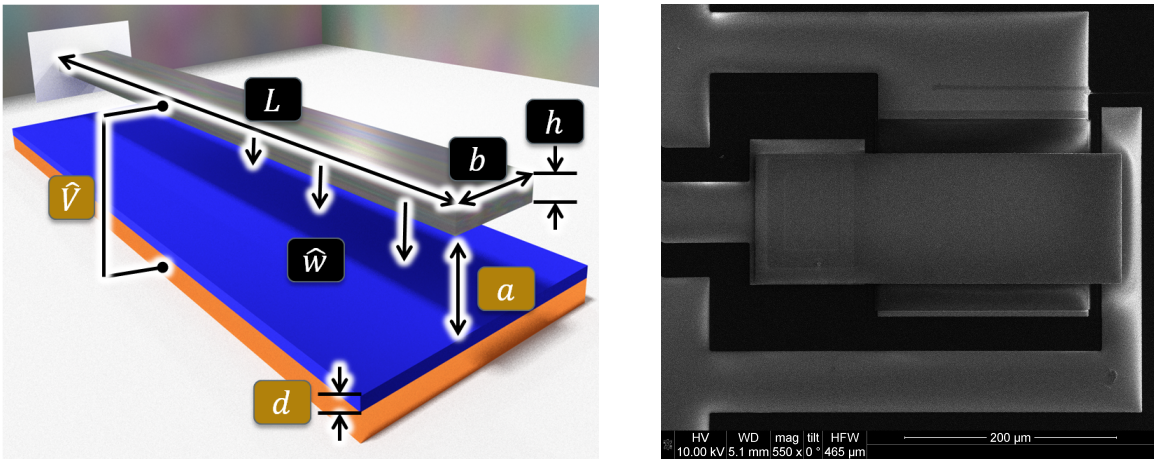

(a) (b)

Figure 3.1. (a) Generalized cantilever capacitive switch configuration, with a fixed-free beam (metallic, suspended from fixed white anchor), dielectric (blue), and underlying electrode (gold). Key parameters identified are: actuation voltage $\hat{V}$, beam length L, beam width b, beam thickness h, beam deflection $\hat{w}$, undeflected air gap a, and dielectric thickness d. (b) [Top view] SEM image of a cantilever MEMS capacitive switch, fabricated by the PRISM center of Purdue University [61]. The nickel beam (center) is anchored on the left, and suspended over a silicon nitride dielectric and an actuation electrode (from top) running along the length of the beam.

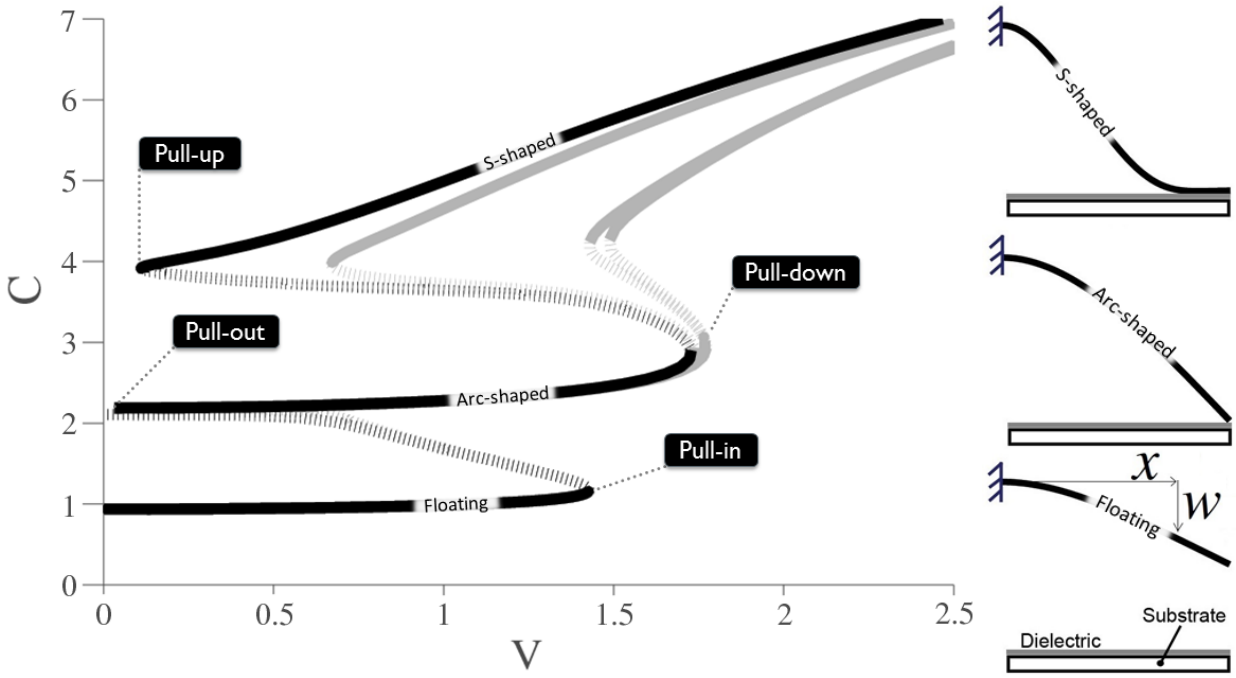

(a) (b)

Figure 3.2. (a) Solutions to the BVP in Equation (3.9), with associated boundary conditions (Equations (3.7) and (3.8)), on the CV plane. These continuation lines are computed in AUTO using parameter values $g = 0.067$, $z_0 = 0.005$, and $H = 0.1, 1.2, 11.2$, and 14.2×10^{-4}, from right to left (i.e. 14.2×10^{-4} as bold, far left line), which exhibit fairly representative behavior across MEMS/NEMS devices. Solid, labeled lines represent stable solutions, while dashed lines represent unstable solutions. Turning points corresponding to system instabilities are located at the transitions between stable and unstable equilibria on a given solution branch. (b) Equilibrium shapes of the cantilever capacitive switch model (anchored on the left), with dimensionless position along length x and dimensionless deflection w. The equilibrium shapes are called s-shaped (TOP), arc-shaped (MIDDLE), and floating (BOTTOM), which are consistent with literature [15], [57].

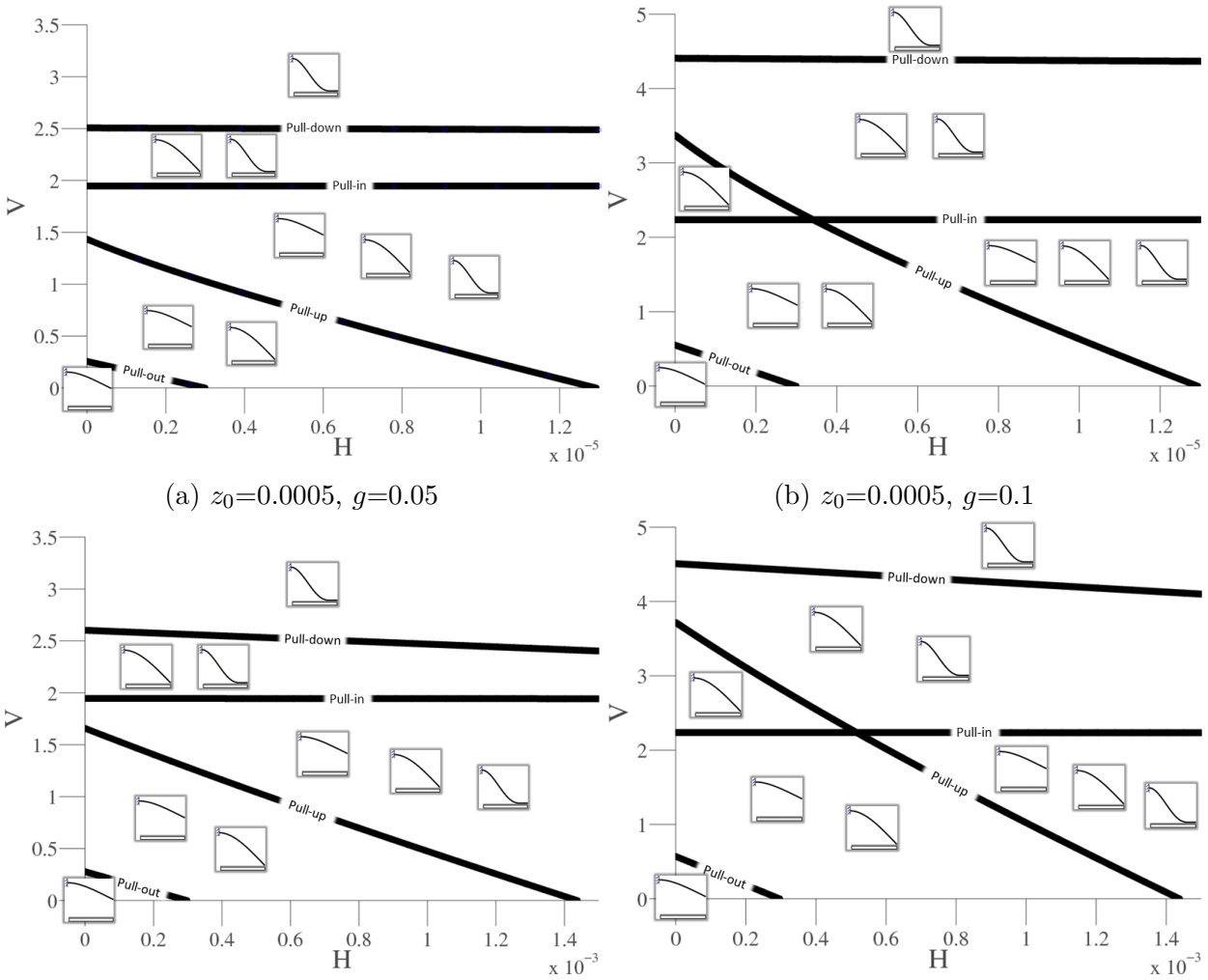

(a) z_0=0.0005, g=0.05

(b) z_0=0.0005, g=0.1

(c) z_0=0.005, g=0.05

(d) z_0=0.005, g=0.1

Figure 3.3. Multistability diagrams windowed on parameters V and H, showing all possible resting states (inset figures) in parameter regions bounded by turning point instabilities (labeled lines); see Figure 3.2 for details. Top and bottom diagram pairs correspond to $z_0 = 0.0005$ and 0.005, respectively, while left and right diagram pairs correspond to $g = 0.05$ and 0.1, also respectively.

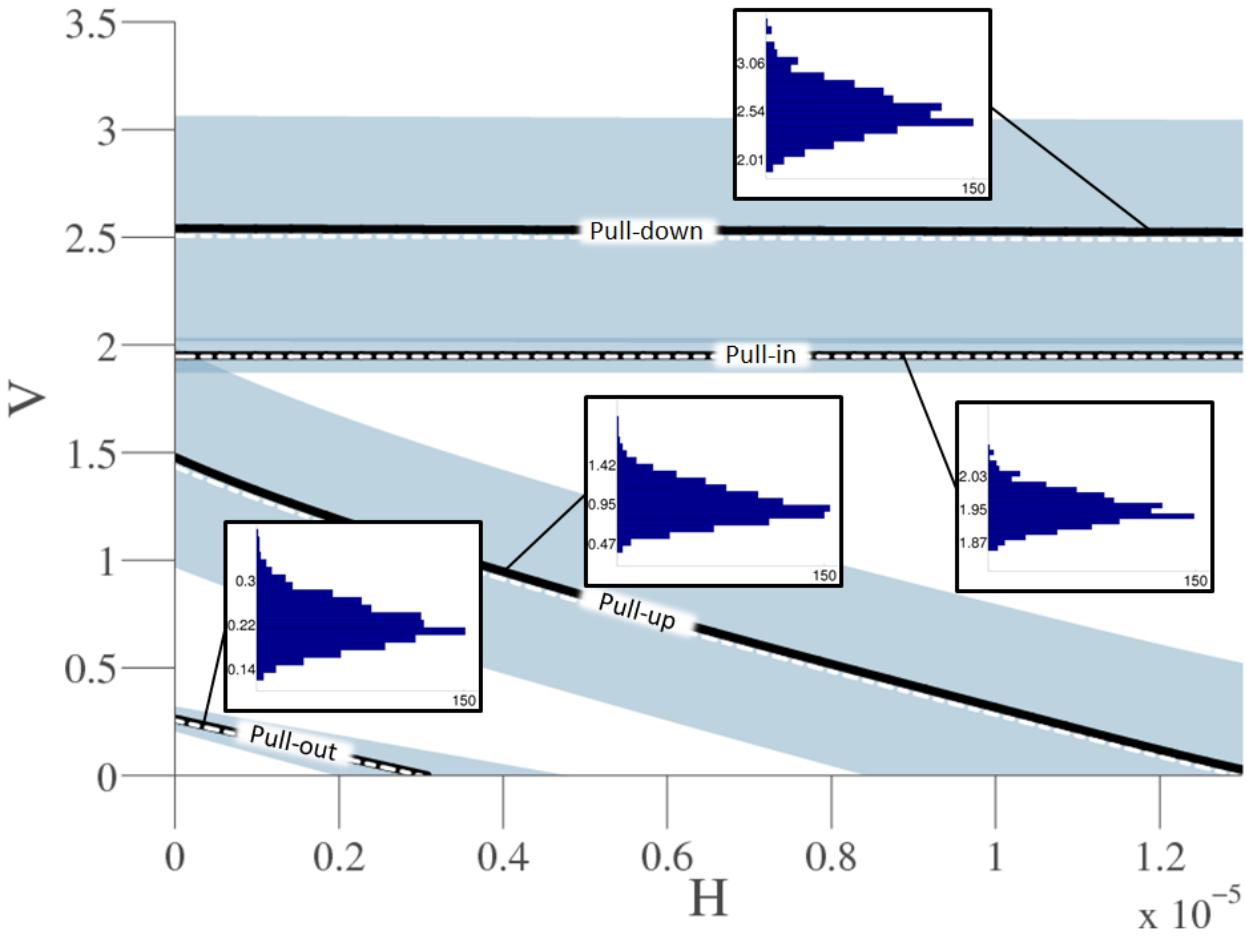

Figure 3.4. Mean lines (solid black), nominal values (dashed white), shaded statistical distributions of two standard deviations above and below the mean, and histogram insets of multistability region boundaries from 1000 Monte Carlo realizations of distributed parameters. Specifically, the figure corresponds to Equation (3.11), where nominal values of $z_0 = 0.0005$ and $g = 0.05$ align with those in Figure 3.3(a).

4. TRISTABLE CAPACITIVE MICROCANTILEVER SWITCHES: MEASUREMENTS AND SIMULATIONS[1]

Multistability is a ubiquitous utilization of nonlinear behavior; light switches, retractable pens, and ratchets are just a few everyday examples. Today, micro- and nanomechanical devices exploit mechanical multistability in circuitry elements to benefit electrical signal manipulation. Multistability at these small scales arises from a competition of elastic, surface, and electrostatic forces. For capacitive microcantilever switches, bistable operation is already commonplace, but inherent tristability expands opportunities for switching, memory, and mechanism applications. Herein, tristability is demonstrated experimentally for 20 capacitive microcantilever switches, while measurement-enhanced simulations quantitatively capture switching thresholds. This chapter goes beyond prior literature theoretically predicting the tristability in switches to experimentally characterize this behavior in real microcantilever devices, and also to present ways to better validate theoretical predictions with experimental results.

4.1 Introduction

If only a single ON and OFF state are desired in MEMS devices, then any additional stable orientation is taken as non-ideal behavior; a fault of design, fabrication, actuation setup, or a mix of all three. This non-ideal behavior, or multistability, can instead drive improvements in several application fields, as seen through novel design [62], [63]; combination of bistable elements [64]–[66]; incorporation of latching mechanisms [67]; or exploitation of material properties [68]–[70].

Capacitive microcantilever switches, a cornerstone of MEMS device configurations, encompass this multistability inherently. This can be summarized via previous works, where mono-, bi-, and tristability is readily encountered in multiphysics mathematical models which include beam mechanics, electrostatic actuation, and surface forces [38], [71], [72]. In studying the static solutions of one multiphysics model, it is shown that the transition points between

[1]↑The findings of this chapter have been disseminated by the paper Kalafut et al. [41] published in the International Journal of Non-Linear Mechanics.

quasi-static switching come about due to saddle-node bifurcations, or turning points, as the voltage is increased or decreased [38]. With regard to the devices considered in the present chapter, shown with components labeled in Figure 4.1a, the resulting stable equilibrium configurations of the microcantilever can be categorized into three cases: floating, arc-shaped, and s-shaped; all depicted in Figure 4.1b.

Experimental evidence of multistability in microcantilevers with surface interactions can be classified into three categories: capacitance measurements of capacitive switches and zipping varactors [73]–[75], current measurements of Ohmic (metal-to-metal) switches [76]–[79], and deflection measurements of adhered microbeams [27], [80]–[82]. The capacitance measurements are of direct interest as they are the MEMS configuration investigated by the current chapter, but they lack associated deflection measurements to confirm nonlinear mechanical behavior. Though Ohmic switches have a different operation profile, tristability in these microcantilevers is important in predicting device failure (secondary pull-in of source to gate). Again, as with capacitive switches, only electrical (current) measurements inform what might be occurring mechanically. Studies of adhesion provide the deflection measurements via interferometry or mechanical probes, however the focus on repairing stiction-failed devices excludes electrostatic actuation. Herein, unequivocal proof of mechanical snap-through behavior in capacitive microcantilever switches substantiates previous nonlinear analysis claims on switching performance, and complements aforementioned works addressing capacitance, (Ohmic) current, and adhesion.

In this chapter, deflection profiles are measured for 20 capacitive microcantilever switches during electrostatic actuation, and a computational model is developed in COMSOL Multiphysics® to explore device-to-device performance variability. Numerical continuation is necessary to identify the quasi-static switching thresholds from stable and unstable branches of the equilibrium solution to this model; time-marching simulations would, at best, only provide an incomplete glimpse of stable behavior at a higher computational expense. While several algorithms exist for numerical continuation in MEMS [40], [83]–[86], the use of commercial software provides an accessible avenue for other MEMS researchers to explore nonlinear behavior of arbitrary geometries and multiphysics. This analysis, developed

in COMSOL Multiphysics®, provides device-specific features of nonlinear behavior which quantitatively match experimental switching threshold measurements.

Section 4.2 of the proposed approach is focused on experimentally measuring the full microcantilever deflection throughout actuation cycles to confirm that the expected switching behavior (i.e. multistability) is occurring. Though the claim of multistability is substantiated, there is as much as a 120 V deviation between experimentally identified switching thresholds (turning point instabilities or saddle-node bifurcations) across the set of devices. In Section 4.3, using a subset of the geometric dimensions accessible through the initial measurement section, simulations of switching thresholds provide tools to investigate the underlying causes of this variability. Specifically, quasi-static continuation performed in COMSOL Multiphysics® reveals device-specific equilibrium curves in the plane of calculated voltage and capacitance from which switching thresholds are determined. In the quantitative comparison between the experimental and simulated switching thresholds of Section 4.4, not only is the nonlinear switching behavior evident, but the device-to-device differences in performance are well captured and explained. The last section provides a brief set of conclusions. For reference, a diagram previewing the major techniques employed throughout the following methods sections is presented in Figure 4.2.

4.2 Initial Device Measurements: Experimental Evidence of Multistability

The first round of device measurements target replication of the nonlinear behavior predicted in Kalafut et al. for a set of fabricated devices under voltage actuation in atmospheric pressure [38]. A brief summary of the fabrication sequence is provided, followed by details on the measurement procedure used to reconstruct the full profile of each individual microcantilever throughout device switching. Microcantilevers are shown to exhibit the floating, arc-shaped, and s-shaped configurations, as well as all four switching thresholds for dynamic jumps between system equilibria, which are documented by their corresponding actuation voltages during the slow ramps up and down.

4.2.1 Microcantilever Configurations During Switching Cycle

Capacitive microcantilever devices were fabricated for the PRISM Center in Discovery Park at Purdue University [61], [87]. Beginning with an oxidized silicon substrate, gold is sputter deposited, patterned, and etched to form two contact electrodes. A layer of silicon nitride is then applied using a plasma-enhanced chemical vapor deposition process, and is subsequently patterned and etched to a single dielectric patch over one segment of gold. Next, a sacrificial photoresist layer is deposited, patterned, and baked to provide a base for the microcantilever. After sputter depositing a thin layer of titanium to promote adhesion, a thin nickel seed layer is evaporation deposited, which is patterned and electroplated to form the microcantilever and anchor. Finally, the sacrificial layer is removed, while exposed titanium and seed layers are etched away with HF and HCl, respectively. For actuation, one probe grounds the dielectric-covered gold electrode, while a second probe provides a bias to the other microcantilever-mounted gold electrode. An example switch, including such actuation probes, is shown in Figure 4.1a with components labeled. Nominal dimensions for the microcantilevers are 250 μm (length) by 120 μm (width) by 2 μm (thickness).

Velocity measurements during full switching cycles provide the first indication of multi-stable behavior, and are the basis of further analysis. A wafer of devices is mounted within a Suss PLV50 ProbeStation in order to control the environmental conditions and employ the accompanying probes. The chamber is pumped down to approx. 1×10^{-3} Torr, and pressurized back to atmospheric pressure (approx. 760 Torr) via a dry nitrogen gas line. This step aids in the reduction of humidity to minimize the unwanted effects of dielectric charging [88], [89]; and capillary adhesion [21]; while maintaining ample pressure to dampen out excessive ringing behavior. Triangular actuation waves, with alternating positive and negative bias to reduce dielectric charging [5], are first generated via the connected Polytec MSA-400 laser Doppler vibrometer (LDV) system. These are then fed through a Piezo Systems EPA-104 linear amplifier (20x gain) before being applied to the microcantilever bias electrode via the corresponding stage probe. Signal generation and acquisition details from the accompanying LDV software are provided in Table 4.1, where a list or range of settings is shown for quantities that change between device scans.

For each device, a rectangular grid of 105 scan points is defined on the top surface of the microcantilever. The system measures each scan point during the application of an actuation wave before moving onto the next scan point, repeating throughout the full grid. The final output is a velocity measurement for each scan point at each sampled point in time. To ascertain a reconstruction of the microcantilever configuration throughout the actuation, the field of velocity data can be numerically integrated, but there is still a need for the initial microcantilever curvature to initialize the resulting displacement field.

To provide the initial microcantilever profile, every device is imaged in a Bruker ContourGT-K 3D optical microscope. In reference to the substrate plane of Figure 4.2, this data directly provides the out-of-plane microcantilever profile and its footprint within the plane, as well as the out-of-plane heights of the gold electrodes and underlying oxidized silicon substrate. An example representation of the height data, after leveling to the flat substrate within the Vision64® Operation and Analysis Software, is shown in the MATLAB plot of Figure 4.3. The one drawback to the white light interferometry technique is that it is not sufficient in capturing the translucent silicon nitride dielectric, which, as an artifact, appears lower than the gold electrode it rests upon. Even without the dielectric layer information, there is enough contribution from these scans to ascertain the undeflected microcantilever profile. This is used to initialize the numerically integrated LDV velocity data and obtain the full microcantilever configurations throughout an actuation cycle.

4.2.2 Results

Both the velocity channel and the corresponding positions are shown in Figure 4.4 for an example device at a scan point along the microcantilever centerline and approximately 50 μm from the tip. In this figure, negative velocity values (decreasing position) correspond to the point moving toward the dielectric layer, while positive velocity values (increasing position) correspond to the point moving away. Thus, there are two sharp transitions towards the dielectric layer during the (absolute) voltage ramp up, and two transitions away during the (absolute) voltage ramp down. This is reflected in the position data as well, where three distinct configurations manifest. The nature of the multistable configurations,

though, is best captured in the switching cycle reconstructions. The three markers for example reconstructions in Figure 4.4 at time instants 0, 4, and 5 ms correspond to the three microcantilever reconstructions of Figure 4.5a (floating), Figure 4.5b (arc-shaped), and Figure 4.5c (s-shaped), respectively. These three shapes appear in the same predictable sequence across hundreds of switching cycles for each device tested.

The actuation voltages at the four high-velocity transitions during a single ON-OFF cycle designate the switching thresholds for a device. During a ramp up of microcantilever bias voltage magnitude (whether positive or negative), the first switching threshold encountered is associated with the pull-in phenomenon, where the microcantilever snaps down from the floating configuration into either the arc-shaped or the s-shaped configuration. If it the former, then the next switching threshold is related to the pull-down, where the microcantilever snaps down from the arc-shaped to the s-shaped configuration. On retraction, pull-up and pull-out refer to the release from the s-shaped and arc-shaped configurations, respectively, and are affiliated with the final two switching thresholds. This is consistent with the instability terminology from Kalafut et al. [38]. These switching thresholds are collected and displayed in Figure 4.6, with devices sorted in ascending order according to the microcantilever bias voltages at which the pull-in phenomenon occurs. Though slight differences (<2 V for devices 1-5; <6 V for devices 6-10; <11 V for devices 11-20) are present between the device-specific switching thresholds identified via positive and negative microcantilever bias voltages, the two magnitudes are averaged for their presentation in Figure 4.6.

4.3 Computational Approach: Capturing Nonlinear Behavior in Simulations

The use of numerical simulations is motivated by the need to explain the device-to-device variability in the experimentally measured switching thresholds. In order to create such simulations, the unknown dielectric layer and microcantilever thickness must be identified for each device. Once obtained, a quasi-static continuation solver is configured in COMSOL Multiphysics® to calculate the full solution branch (both the stable and unstable segments from Kalafut et al. [38]). The nonlinear tristable behavior is not only observed computationally;

device-to-device switching thresholds are quantitatively similar to experimental performance, indicating that the variability is aptly captured through measured differences in geometry.

4.3.1 Device Geometry

To circumvent the imaging artifact of the optical microscope, an Asylum Research MFP-3D-BIO AFM can directly determine the dielectric layer thickness. In order to access the scan region indicated in Figure 4.2 with enough clearance for the AFM equipment, the microcantilever is removed manually (tweezers) for a small set of representative devices. The chosen silicon AFM cantilevers are model CSC38 from MikroMasch (Wilsonville, OR), with 350 µm length, 32.5 µm width, 1 µm thickness, and a nominal spring constant of 0.03 $\frac{\text{N}}{\text{m}}$. Images are created at a scan rate of 1 Hz and a force setpoint of approximately 1 nN in contact mode. For an example device in this set, Figure 4.7 depicts a leveled reconstruction of the 256 px by 256 px scan data (50 µm by 50 µm), while the inset is the associated histogram of pixel heights. From these AFM measurements on five separate devices whose microcantilever have been removed, an average dielectric thickness is calculated from a single peak-to-peak difference on each AFM scan histogram, like that of the inset in Figure 4.7, with results shown in Table 4.2. An average layer thickness of 559 nm from this set of five microcantilever-less devices is used for further analysis and interpretation across the 20 devices used in switching measurements.

The four critical features of the device geometry are the microcantilever profile, the microcantilever thickness, the gap between the microcantilever and the dielectric, as well as the dielectric layer thickness. From direct measurements, the microcantilever top surface profile (optical microscope) and dielectric layer thickness (AFM) are known. Additionally, the tip gap can be found by the maximum distance traveled by the free microcantilever tip (LDV), leaving just the microcantilever thickness unknown. Subtraction of the electrode thickness, dielectric layer thickness, and tip gap from the height of the microcantilever top surface results in the microcantilever thickness at the tip, which is assumed to be uniform throughout its profile. In brief, all but the dielectric layer thickness are obtained uniquely for

each device, allowing for a device-to-device assessment of the relationship between geometry and multistable switching behavior.

4.3.2 COMSOL Multiphysics® Simulations

Once identified, all four critical features of device geometry are imported into COMSOL Multiphysics® along with relevant material properties and physics models to best account for device-to-device variability in switching performance. The computation is set up as a 2D simulation within a vertical, centerline cross-section along the length of the microcantilever, using an assumed out-of-plane depth corresponding to the microcantilever width (see Figure 4.2 for orientation). In order to quantitatively capture the switching thresholds, three primary physics models are included for computation: linear elastic solid deformations, electrostatics, and a Lennard-Jones form of an attractive-repulsive boundary interaction between the microcantilever and dielectric layer from Kalafut et al. [38]. An example representation of computational domains is included in Figure 4.8, while associated material definitions and other settings for the multiphysics computational model are accumulated within Tables 4.3 and 4.4. A synopsis of boundary definitions for the computational domains is as follows (domains correspond to those in Figure 4.8:

- Microcantilever (domain 2): nickel
  - Fixed (zero) displacement at boundary of computational domain associated with anchor
  - Electromechanical coupling (Maxwell stress tensor) at all boundaries with surrounding nitrogen gas
  - Attractive-repulsive boundary interaction at underside and tip with respect to distance from dielectric layer
  - Voltage potential bias on boundaries with surrounding nitrogen gas
- Surrounding atmosphere (domain 1,3,6): nitrogen
  - Prescribed deformation to coincide with microcantilever and dielectric layer deformations

  - Zero charge (electrostatic) at computational domain edges
- Dielectric layer (domain 4,7): silicon nitride
  - Fixed (zero) displacement at boundaries of computational domain
  - Attractive-repulsive boundary interaction at top surface with respect to distance from microcantilever
  - Zero charge (electrostatic) at computational domain edges
- Electrode (domain 5,8): gold
  - Fixed (zero) displacement at boundaries of computational domain
  - Grounded (electrostatic) at boundary with dielectric layer

For the computation sequence itself, a procedure is configured to calculate the static equilibrium solutions via continuation from the undeflected, unactuated configuration. As the voltage bias applied to the microcantilever is expected to both increase and decrease throughout the solution steps, the continuation within COMSOL Multiphysics® is accomplished by defining a separate monotonically increasing parameter driving the step direction. In all simulations, the continuation parameter is the average, absolute displacement of the underside of the microcantilever. Additionally, the capacitance between the grounded gold electrode and the biased nickel microcantilever at each computation step is calculated within the software to construct a representation of the solution output on the capacitance-voltage (CV) plane. As with prior descriptions of the simulations, details on the solution method specific to COMSOL Multiphysics® settings are collected in Tables 4.3 and 4.4.

4.3.3 Results: Device-Specific Capture of Switching

The tristability observed in experimental reconstructions of microcantilever configurations is also captured in the COMSOL Multiphysics® simulations, built using the device geometries found during the measurement steps. To assess the COMSOL Multiphysics® results, quasi-static switching thresholds are identified as the four vertical tangents on the CV plane, as shown in the example plot of Figure 4.9. Due to the limitations of the continuation method employed within COMSOL Multiphysics®, the precise nature of stability is not

calculated explicitly for each step, but rather assumed for the similarity in features from Kalafut et al. [38]. The four switching thresholds are collected for each device and plotted in Figure 4.10a for COMSOL Multiphysics® continuation solutions, sorted in ascending order by experimental microcantilever bias voltages at which pull-in occurs. Furthermore, the inferred microcantilever thicknesses as well as the tip gaps are plotted in Figure 4.10b.

4.4 Discussion

For all 20 devices in the measurement set, which excludes the 5 additional microcantilever-less devices used for AFM scans, the same tristability from theoretical capacitive microcantilever switch studies appear in the experimental reconstructions [15], [38]. Additionally, when the device material properties and geometries are loaded into COMSOL Multiphysics® simulations, the continuation solutions (Figure 4.10a) capture the device-to-device variability in measured switching thresholds (Figure 4.6). Of the 80 total simulated switching thresholds (pull-in, pull-out, pull-up, and pull-down for each of the 20 devices), 22 of them are within ±10% of their corresponding experimental measurements, 72 are within ±50%, and all are within ±70%. So, device-specific switching performance can be predicted from this predominantly non-destructive method, requiring no more input than the brief list of materials used in fabrication.

As the predictive capability of this method is strong with regard to switching thresholds, the measured and inferred geometries are assumed to provide all of the device-to-device variation. The critical geometries that differ between devices are the microcantilever thickness (assumed to be uniform along microcantilever length) and the microcantilever profile, which is reduced to just the gap of nitrogen gas between the microcantilever and the dielectric layer at the free end. Comparing the geometries of Figure 4.10b to the experimental and simulated switching thresholds of Figure 4.6 and Figure 4.10a, respectively, the microcantilever thickness appears to be the governing contribution to the switching threshold variation.

At first glance, a shortcoming of the proposed method is the lack of a direct thickness measurement of the microcantilever, but the approach for indirectly determining this geometry is found to be robust with respect to the identification of switching thresholds. Between

the top surface of the gold electrode and the top surface of the microcantilever (a height measured by the optical microscope), there exists the dielectric layer, a small expanse of nitrogen gas, and the microcantilever itself. While the gas region geometry is calculated on a device-to-device basis from switch performance monitoring, the dielectric layer is an assumed value across each device in the set. If it is over predicted, the microcantilever thickness is under predicted, and vice versa. As a brief exploration, Figure 4.11 summarizes the change in switching thresholds as the example device from Figure 4.9 is further simulated with a wide range of dielectric layer thicknesses and the corresponding microcantilever thicknesses. None of the four critical switching thresholds show any appreciable sensitivity across the span of thicknesses considered, though it is not determined whether the source of the apparent robustness is the small scale of the thickness variability relative to the system as a whole, or a benefit from the additive inverse relationship between dielectric layer and microcantilever thickness errors. For further detail on the relationship between modeling parameters and multistability, the work of Kalafut et al. provides a theoretical investigation using a multiphysics mathematical model [38].

Justification for the computational methodology resides in the degree of quantitative matching with experimental switching thresholds, but many unincorporated mechanical intricacies could be included for higher prediction accuracy. At the micro scale, it can be important to identify material properties (Young's modulus, Poisson's ratio, inhomogeneity, and grain size effects) and clamping compliance on a case-by-case basis to adjust bending stiffness of the microcantilever. Also due to the length scale of the problem, surface roughness between the microcantilever and dielectric layer can reduce the effective contact area, and in turn require an adjustment of the Lennard-Jones form of the surface interaction model used in the study. Finally, due to the choice of constructing a 2D simulation in COMSOL Multiphysics®, there is no explicit inclusion of lateral effects: double curvature, electrostatic field fringing around the sides of the microcantilever, and switching due to microcantilever twisting (no appreciable evidence of this twisting behavior is present in the experimental measurements). If a quantitative improvement to this study is critical, then many of these considerations should be revisited.

4.5 Conclusion

Tristable behavior is now experimentally confirmed with deflection measurements (full profile reconstructions throughout device operation) across 20 capacitive microcantilever switches. Also, the numerical continuation scheme implemented in COMSOL Multiphysics® captures the complete set of stable and unstable equilibria, while quantitatively matching the experimental switching thresholds. Capacitive microcantilever switches with tristability expand options for multistable mechanism design, provide a foundation for bidirectional acceleration threshold sensing, increase cantilever-based memory cell storage density, and alter the current usage of such devices in RF circuitry.

Table 4.1. Polytec Scanning Vibrometer Software: Acquisition Settings

Tab	Option	Setting
General	Measurement mode	Time
	Averaging	Off
Channels	Vibrometer range	200 mV, 500 mV, 1 V, 2 V, 5 V, 10 V
	Vibrometer impedance	1 MOhm
	Vibrometer quantity	Velocity
	Reference range	5 V, 10 V
	Reference impedance	1 MOhm
Filters	N/A	No filters
Time	Sample frequency	102.4 MHz
	Samples	2097152
Trigger	External (TTL)	Rising
	Pre-trigger	0% of Sample time
Vibrometer	Velocity (VD-02)	5, 25, 125, 1000 mm/s/V
	Tracking filter	Off
	Low Pass filter	1.5 MHz
	High Pass filter	Off
Generator	Waveform	Triangular
	Amplitude (pre-20x gain)	4 to 10 V
	Offset	0 V
	Frequency	50 Hz
	Amplifier	On (checked)
	Wait for steady state	0 s

Table 4.2. AFM Measurements of Dielectric Thickness on Five Microcantileverless Devices

Device 21	552 nm
Device 22	606 nm
Device 23	585 nm
Device 24	539 nm
Device 25	511 nm
Mean	559 nm
Std. Dev.	38 nm

Table 4.3. COMSOL Multiphysics® Simulation Details (Domains from Figure 4.8), Part 1

Main Structure	Substructure	Option	Setting
Global definitions	Parameters	Horizontal domain	350 µm
		Vertical domain	20 µm
		Hamaker constant	1×10^{-21} J
		Zero pressure gap	10 nm
Materials	Ni - Nickel (Domain 2)	Density	8900 $^{kg}/_{m^3}$
		Young's modulus	219 GPa
		Poisson's ratio	0.31
	Si3N4 - Silicon nitride (Domain 4,7)	Density	3100 $^{kg}/_{m^3}$
		Young's modulus	250 GPa
		Poisson's ratio	0.23
		Relative permittivity	3.7
	Au - Gold (Domain 5,8)	Density	19300 $^{kg}/_{m^3}$
		Young's modulus	70 GPa
		Poisson's ratio	0.44
	N - Nitrogen (Domain 1,3,6)	Relative permittivity	1
Moving mesh (Domain 1,3,6)	N/A	Geometry shape order	4
		Mesh smoothing type	Winslow
Solid mechanics (Domain 2,4,5,7,8)	N/A	2D Approximation	Plane stress
		Thickness	110 µm
		Structural transient behavior	Quasi-static
		Displacement field discretization	Quadratic serendipity
	Linear elastic material	Temperature	293.15 K
		Absolute pressure	1 atm
		Linear elastic material solid model	Isotropic

Table 4.4. COMSOL Multiphysics® Simulation Details (Domains from Figure 4.8), Part 2

Electrostatics (Domain 1,3,4,6,7)	N/A	Out-of-plane thickness	110 µm
		Reference impedance	50 Ohm
		Electric potential discretization	Quadratic
	Charge conservation	Temperature	293.15 K
		Absolute pressure	1 atm
		Electric field constitutive relation	Relative permittivity
Mesh	Distribution 1 (Domain 1,2,3,4,5)	Number of elements	100
		Element ratio	80
		Distribution method	Geometric sequence
	Distribution 2 (Domain 6,7,8)	Number of elements	30
		Element ratio	60
		Distribution method	Geometric sequence
			Reverse direction
Study	Solver configurations → Stationary solver → Direct	Solver	PARDISO
		Preordering algorithm	Nested dissection multithreaded
	Solver configurations → Stationary solver → Fully coupled	Nonlinear method	Automatic (Newton)
		Initial damping factor	1
		Minimum damping factor	1×10^{-16}
		Restriction for step-size update	10
		Use recovery damping factor	Automatic
		Termination technique	Tolerance
		Maximum number of iterations	1000
		Tolerance factor	1
		Termination criterion	Solution or residual
		Residual factor	1000
	Solver configurations → Stationary solver → Parametric (Continuation)	Initial step size	0.001
		Minimum step size	1×10^{-20}
		Maximum step size	0.1

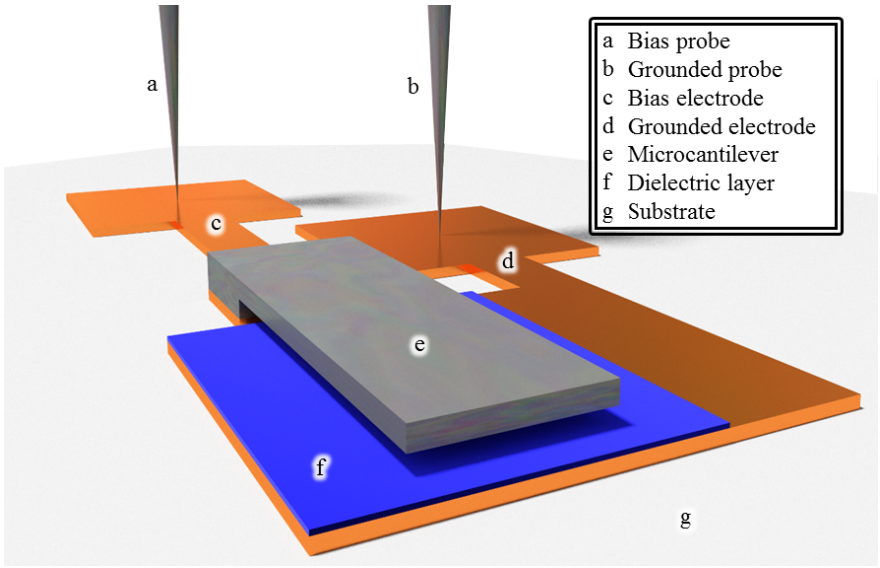

(a)

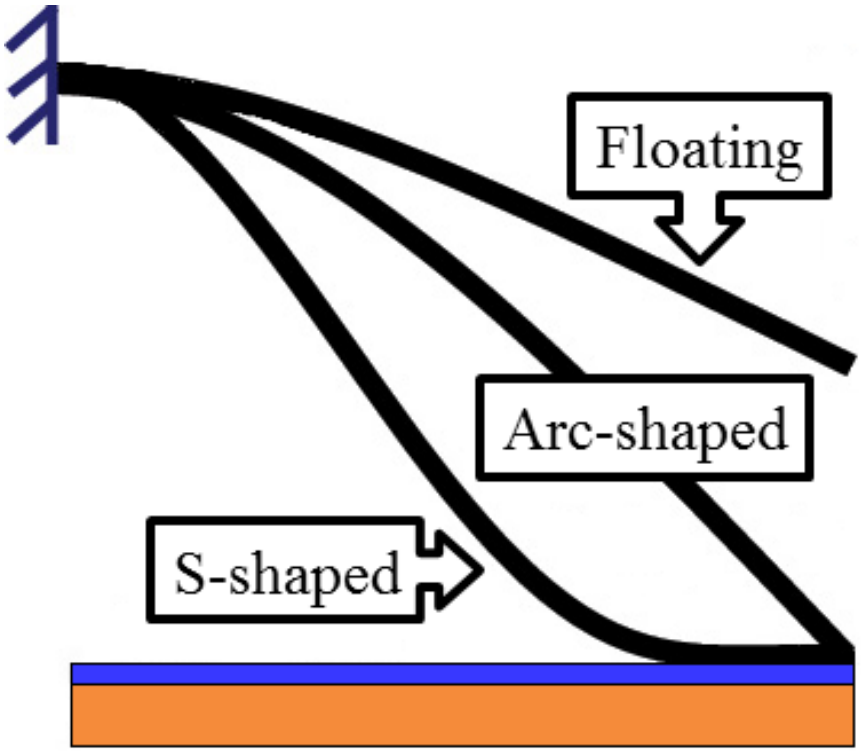

(b)

Figure 4.1. (a) Diagram of an individual device with actuation probes, gold electrodes, nickel microcantilever, silicon nitride dielectric layer, and oxidized silicon substrate labeled. (b) Floating, arc-shaped, and s-shaped equilibrium configurations for a tristable capacitive microcantilever switch; microcantilever configurations (black curves) are anchored on the left, while suspended over the dielectric (blue box) and electrode (gold box).

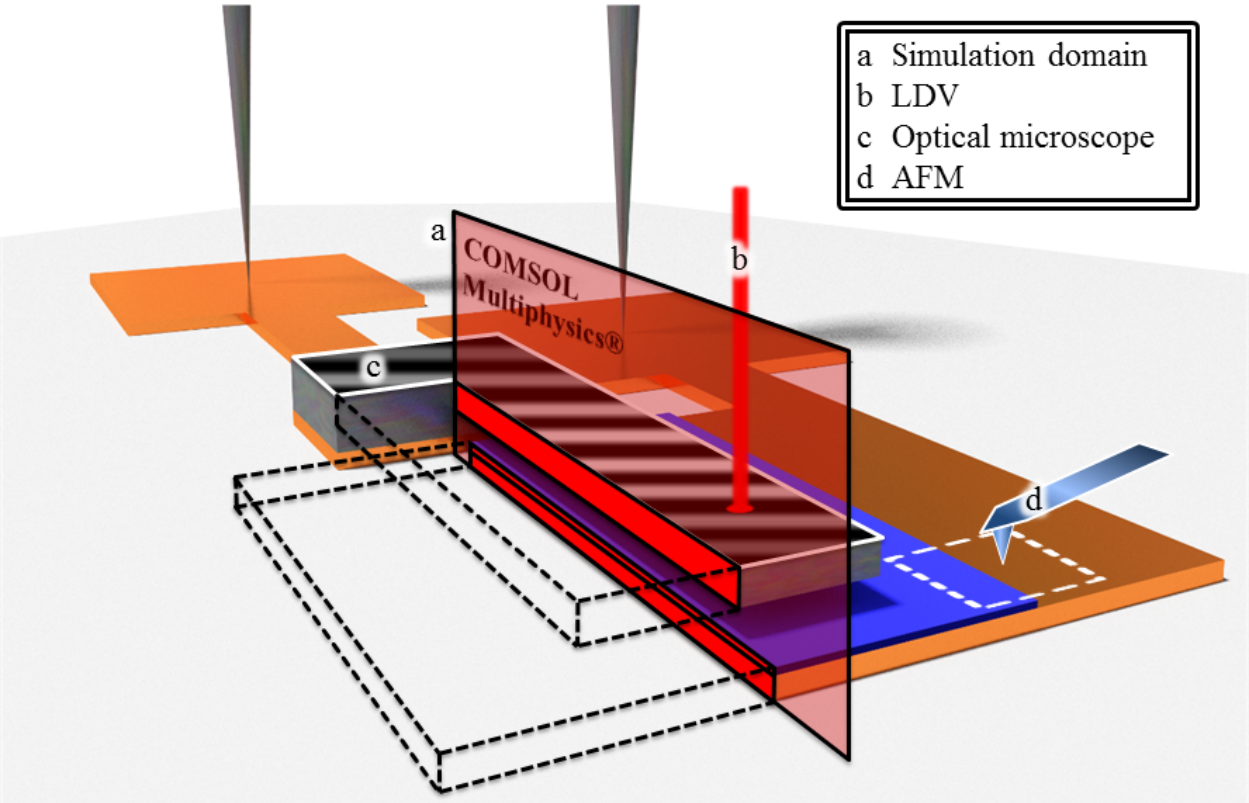

Figure 4.2. Schematic of the experimental setup at device-level, with measurement processes and 2D simulation domain identified. COMSOL Multiphysics® simulation domain is represented by a rectangular pane intersecting the microcantilever along its vertical centerline, laser Doppler vibrometer (LDV) scans are indicated by a red laser beam, optical microscope scans are depicted as an interference pattern superposed on the top surface of the microcantilever, and the AFM scans are illustrated by an exaggerated AFM cantilever.

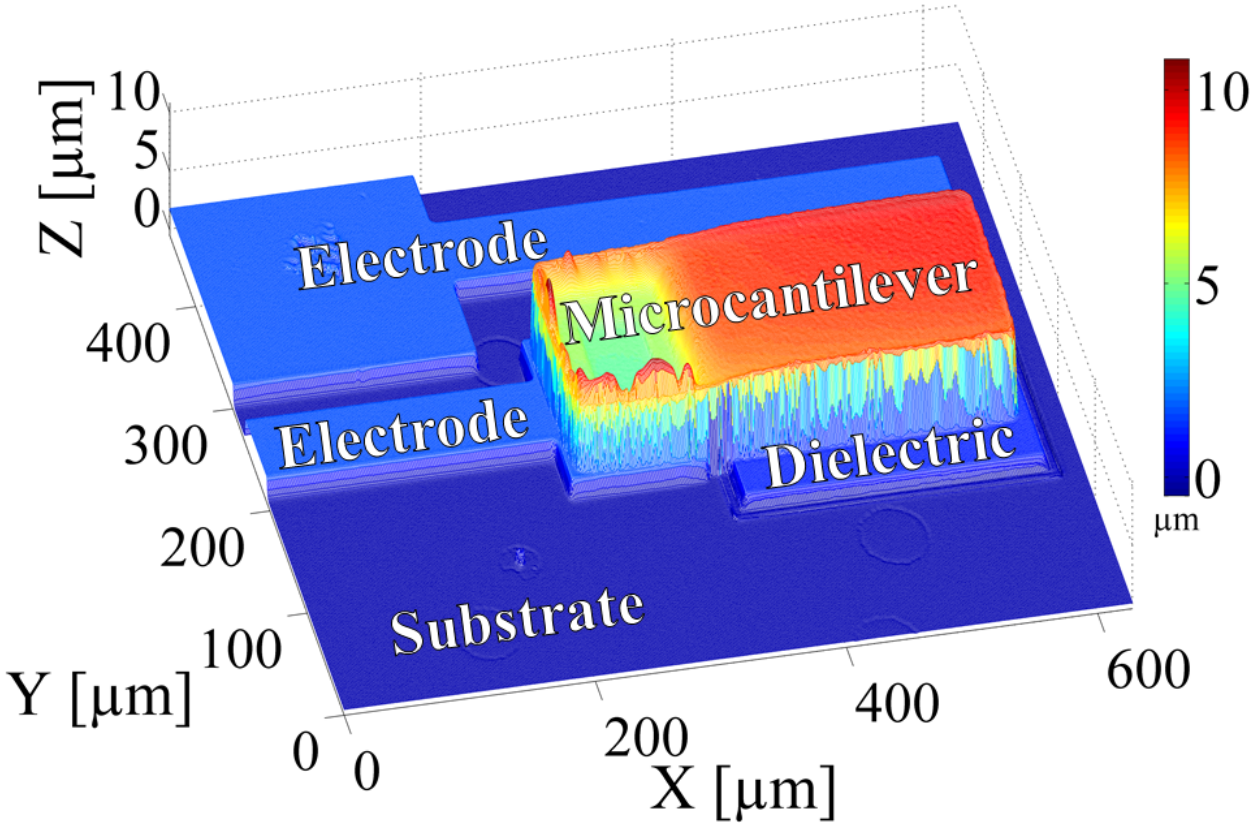

Figure 4.3. Bruker optical microscope scan data reconstruction for a single device, zeroed and leveled to the substrate. The gold electrodes and microcantilever, labeled in Figure 4.1a, are visible with correct heights, while the dielectric layer is not imaged accurately via this white light interferometry technique.

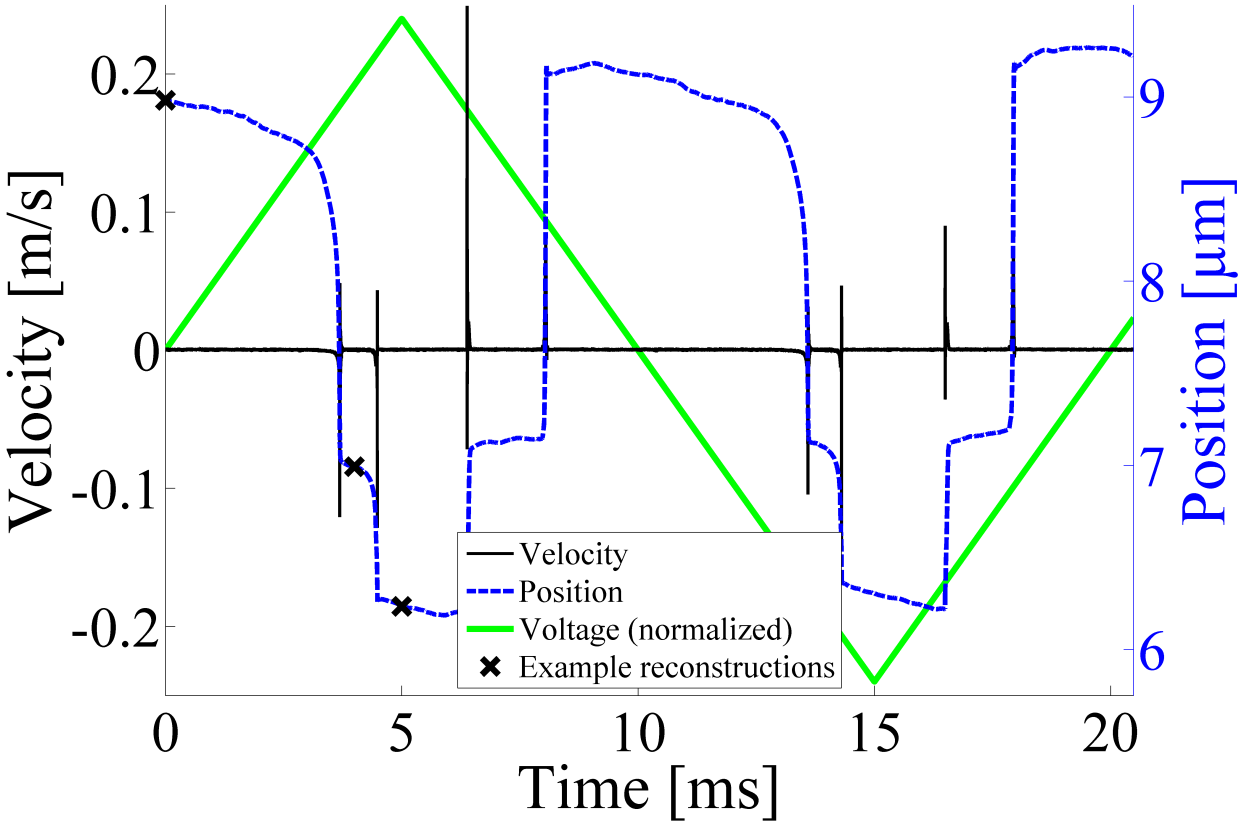

Figure 4.4. LDV velocity measurement for an example device, with normalized actuation voltage waveform and numerically processed position included. The example reconstructions correspond to Figure 4.5.

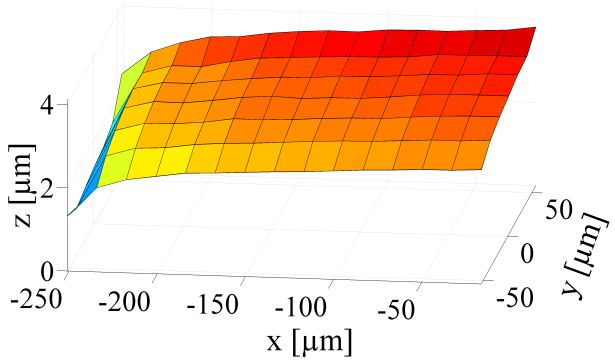

(a)

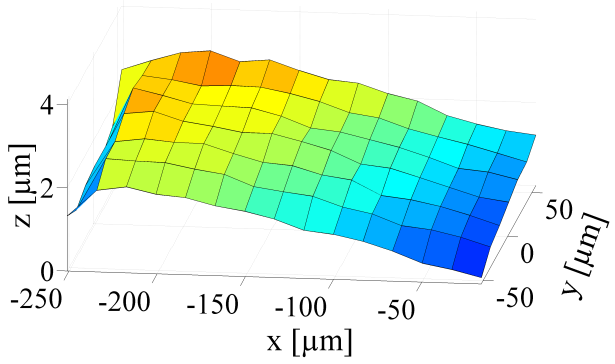

(b)

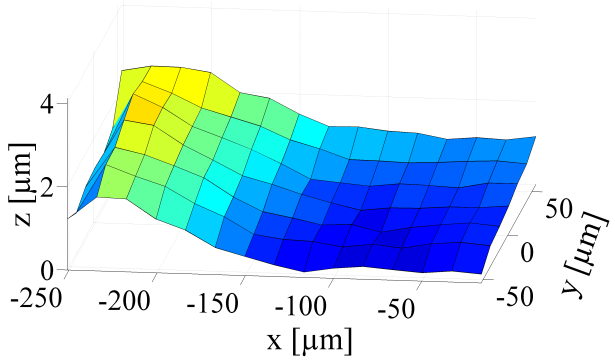

(c)

Figure 4.5. Three microcantilever configurations from an example device, corresponding to the example reconstruction markers in Figure 4.4: (a) floating at 0 ms, (b) arc-shaped at 4 ms, and (c) s-shaped at 5 ms.

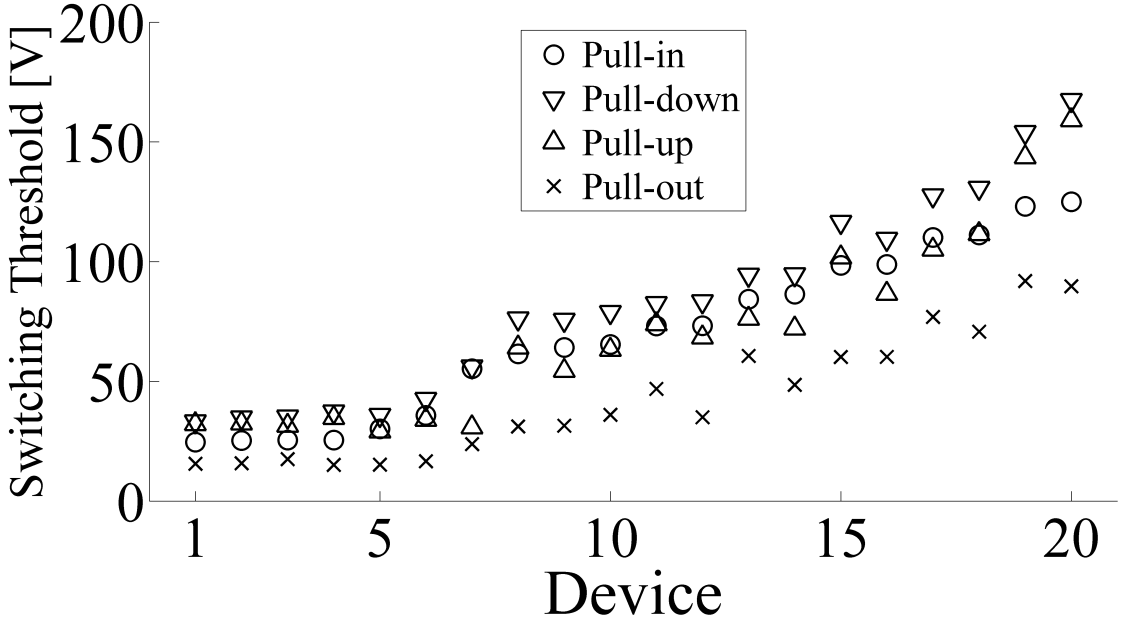

Figure 4.6. Four experimental switching thresholds (microcantilever bias voltages corresponding to pull-in, pull-down, pull-out, and pull-up) for each of the 20 measured devices. .

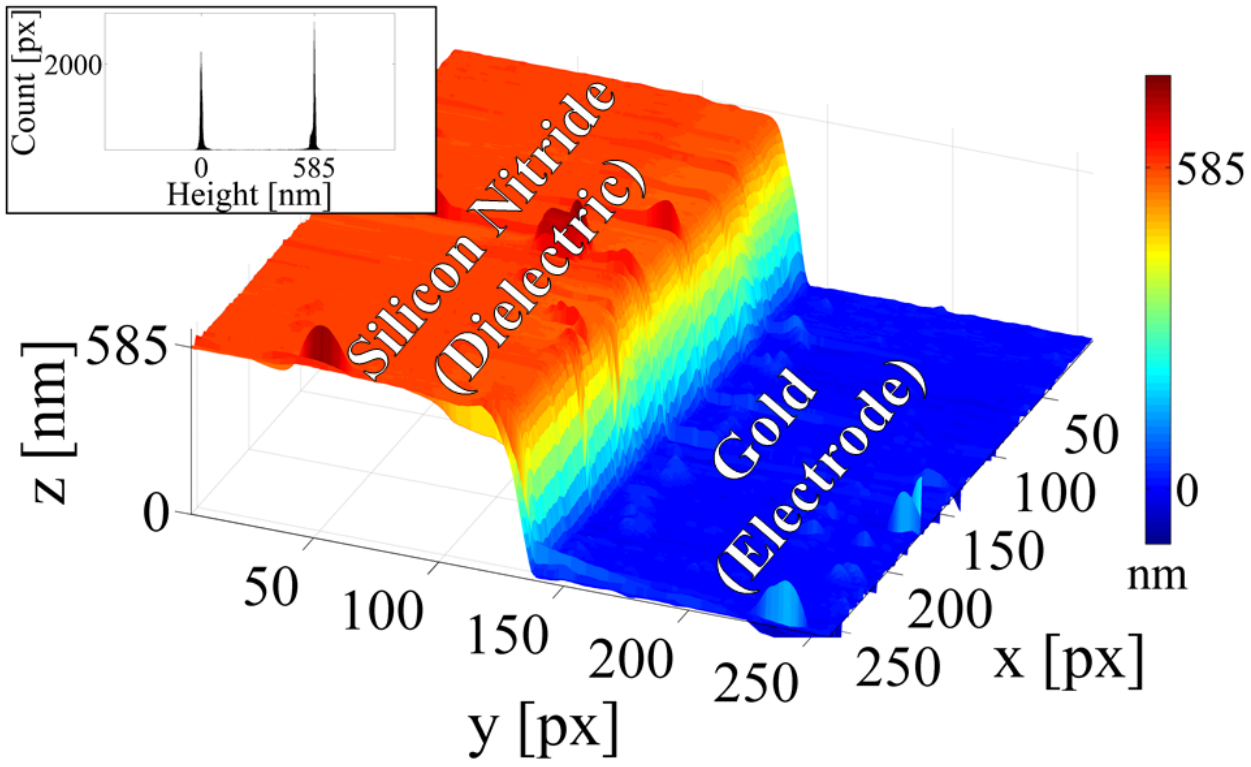

Figure 4.7. Scan data from the Asylum Research MFP-3D-BIO AFM in contact mode for a single dielectric layer over a gold electrode, from the location shown in Figure 4.2. The 256 px by 256 px domain corresponds to a 50 µm by 50 µm region, and the image is zeroed and leveled to the grounded electrode. Inset depicts the histogram (1 nm bin widths) of scan data pixel heights.

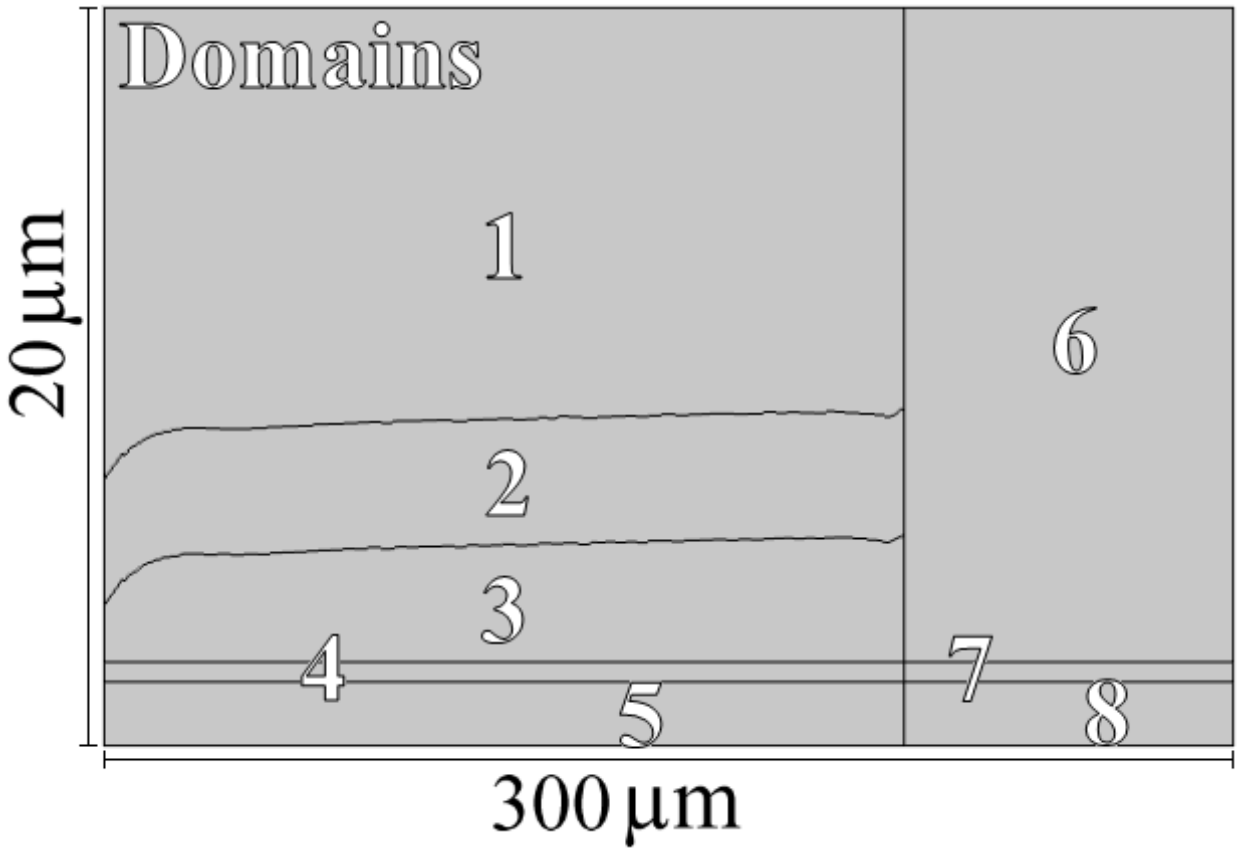

Figure 4.8. 2D COMSOL Multiphysics® geometry initialization for an example device, with domain identifiers indicated for use in Tables 4.3 and 4.4. Domain 2 is nickel (microcantilever); domains 1,3, and 6 are nitrogen gas; domains 4 and 7 are silicon nitride (dielectric layer); and domains 5 and 8 are gold (electrode).

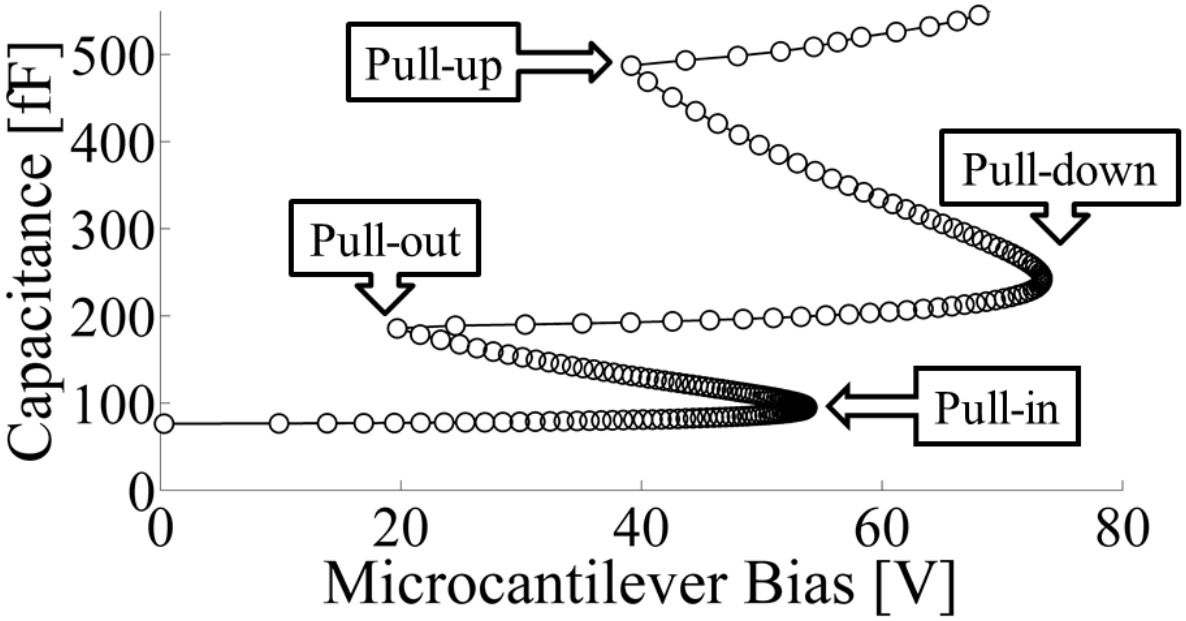

Figure 4.9. COMSOL Multiphysics® quasi-static continuation results for an example device with displayed continuation steps (circles), though even more intermediate steps are used in the calculation process. Switched thresholds (turning point instabilities) are labeled accordingly.

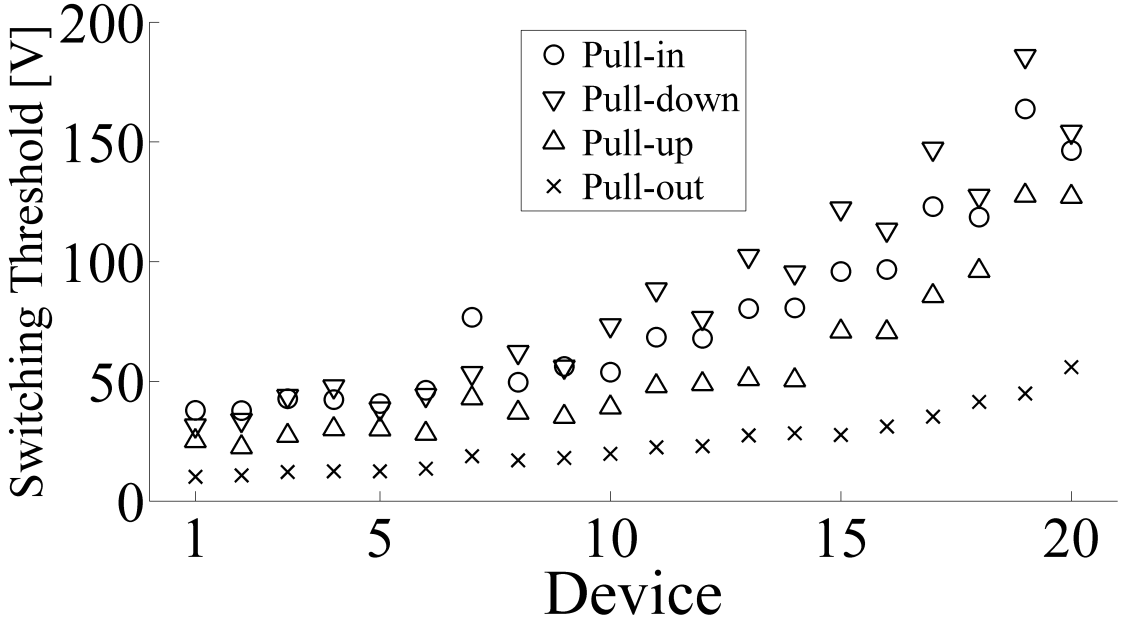

(a)

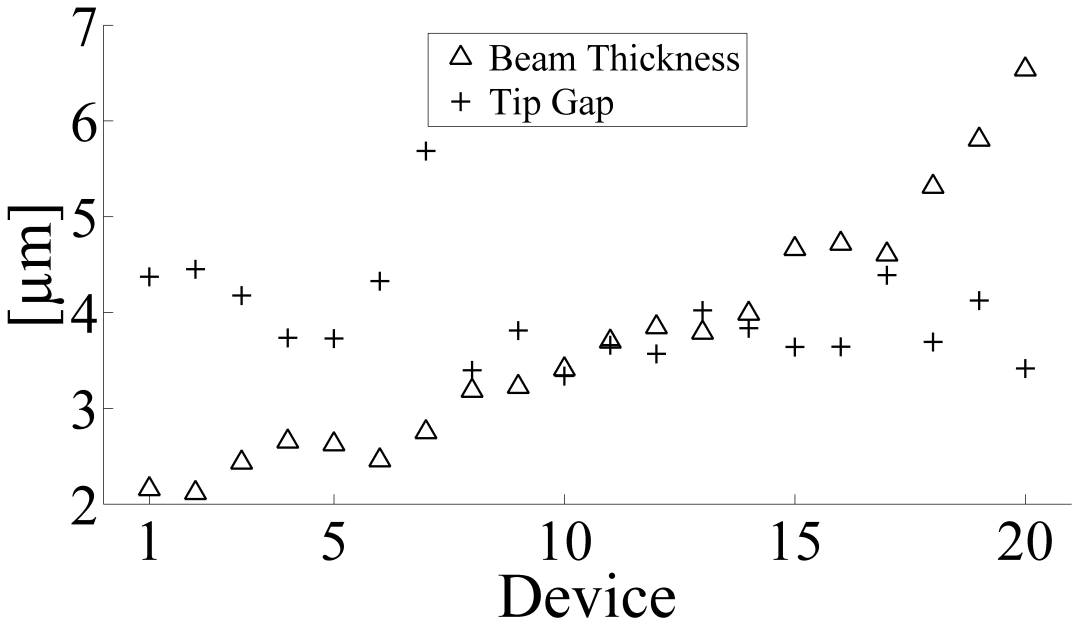

(b)

Figure 4.10. (a) Four switching thresholds (microcantilever bias voltages corresponding to pull-in, pull-down, pull-out, and pull-up) for each device, as calculated in COMSOL Multiphysics® continuation computations. Device labeling is consistent with that of Figure 4.6. (b) Experimentally identified microcantilever thickness and tip gap for each device, sorted as in (a), which explains the geometrical parameter contributions to the differences in device performance.

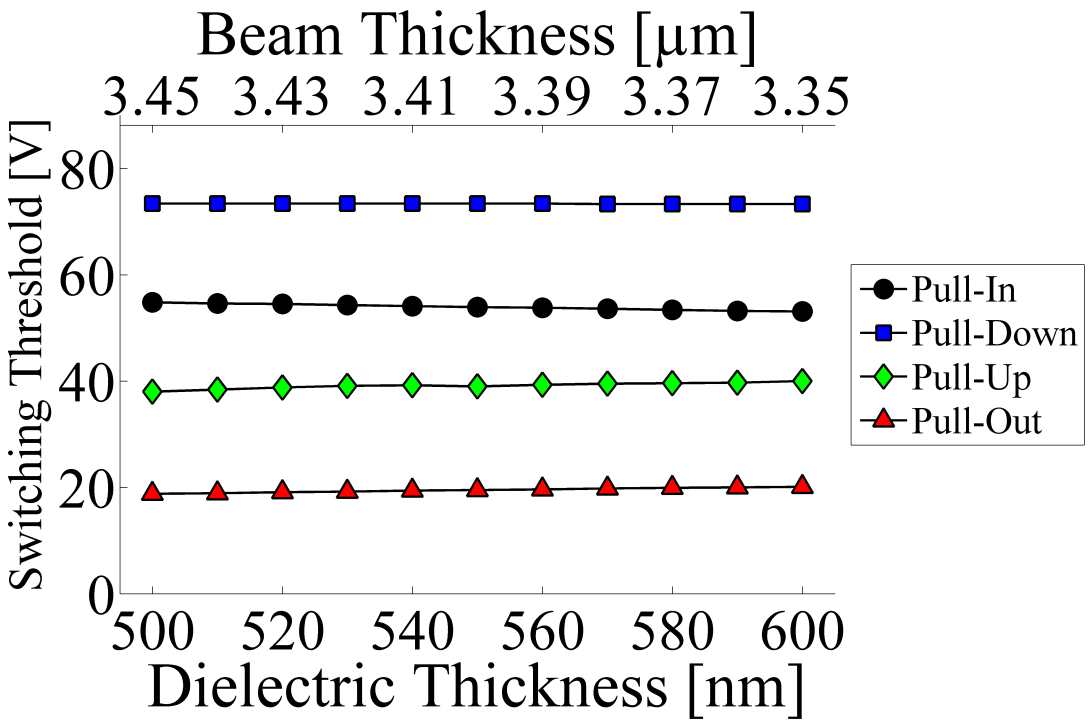

Figure 4.11. Switching thresholds for the example device from Figure 4.9 when simulated with a range of dielectric thicknesses (bottom axis) and associated microcantilever thicknesses (top axis). For reference, the dielectric thickness for the original simulation is 559 nm.

5. CANTILEVER SIGNATURE OF DYNAMIC RELEASE FROM CONTACT IN ATOMIC FORCE MICROSCOPY

Contact resonance atomic force microscopy, piezoresponse force microscopy, and electrochemical strain microscopy are atomic force microscopy modes in which the cantilever is held in contact with the sample at a constant average force while monitoring a small superimposed vibrational signal. Detailed analytical models and clear experimental observables that indicate when the limit of small vibration permanent contact is violated are lacking. Additionally, higher operating amplitudes tend to yield better signal-to-noise ratio, so users may inadvertently reduce their experimental accuracy by inducing tip-sample detachment in an effort to improve their measurements. This issue is solved by deliberately pushing both experimental equipment and numerical simulations to the point of tip-sample detachment to uncover a useful and observable threshold feature in the cantilever response. This is a critical feature identification which assists experimentalists in finding an upper bound for operating amplitude when needing to satisfy the small vibrational amplitude permanent contact assumption in different atomic force microscopy imaging modes. Numerical simulations of the analytical model also allow exploration into cantilever dynamics such as full-length deflection and slope behavior which can be challenging or unobtainable in a standard equipment configuration.

5.1 Introduction

Contact resonance atomic force microscopy (CR-AFM) [90], [91], piezoresponse force microscopy (PFM) [92], and electrochemical strain microscopy (ESM) [93] are atomic force microscopy (AFM) [94] methods where the probe tip is held in contact with the sample at a constant average force while a small superimposed vibrational response is monitored. CR-AFM can measure the viscoelastic properties of a sample [95] and observe subsurface features in some biological and electronics samples [96]–[101]. PFM can measure a sample's piezoelectric and ferroelectric properties [102]–[105]. ESM can measure the ion diffusion in battery materials [93], [106]–[108]. These different AFM methods provide important mechanical and electrical properties across a wide variety of samples.

CR-AFM, PFM, and ESM are built upon the fundamental assumption that as the cantilever is excited, the probe tip remains in contact with the sample. Signal-to-noise ratios in these measurements can be improved by increasing the magnitude of the drive amplitude. However, clear limits on the maximum drive amplitude are poorly defined. Early CR-AFM works suggested that as users operate with high enough drive excitation amplitude, nonlinearity occurs in the response [109]–[111]. Unfortunately, they were not able to either connect the feature to a physical phenomenon or a reproducible characteristic of their model. The mechanical and dynamic processes involving the probe tip detaching from a surface have not been systematically studied.

Presented in this chapter is a systematic analytical, numerical, and experimental study of the process of a probe tip detaching from a sample in CR-AFM. It connects the experientially observed nonlinear response feature to the onset of tip-sample detachment in numerical simulations. The simulations allow for deeper insight into the interaction between the AFM probe tip and the sample, which in turn allows identification and characterization of three different operating regimes: linear, nonlinear softening, and tip-sample detachment. This result provides clear guidance on amplitude limits in CR-AFM, PFM, and ESM measurements.

5.2 Results

Experimental measurements and numerical simulations of cantilever response amplitude as a function of drive frequency at different drive amplitudes are shown in Figure 5.1. Figure 5.1a shows the experimental photodiode amplitude signal as recorded with the AFM's lock-in amplifier in units of volts. Figure 5.1b compares the photodiode amplitude signal in units of μrad to a numerical simulation of the cantilever response driven by moment-couples of different magnitudes. Figure 5.1c shows the maximum deflection of the cantilever about static equilibrium for the numerical simulations. The dashed grey line in this figure indicates the location of the undeformed sample surface. These results directly compare the numerical simulations with experimental measurements.

Detailed breakdowns of the numerical simulations for two different moment couples are shown in Figure 5.2. The lowest bending moment couple amplitude of 1 N·m is shown

in the left column (a,c,e,g), and highest bending moment couple amplitude of 15 N·m is shown in the right column (b,d,f,h). Figures 5.2a and 5.2b represent stroboscopic depictions of cantilever deflection and Figures 5.2c and 5.2d represent stroboscopic depictions of the cantilever slope. For each period of steady-state oscillation, ten equispaced snapshots about the cantilever's static equilibrium are provided. The deflection plots include additional shapes for the analytical first eigenfunction of the cantilever-sample system. Figures 5.2e and 5.2f are plots of the steady-state oscillation position of the probe tip versus time, with the undeflected sample surface location provided for reference. Figures 5.2g and 5.2h are the accompanying Fast Fourier Transform (FFT) data for the steady-state oscillation slope response of the cantilever at the location above the probe tip. Note that the first harmonic amplitude (i.e. the FFT amplitude corresponding to the applied drive frequency) is the value plotted for the simulations in Figure 5.1b since it corresponds to the response amplitude of the photodiode detector from the lock-in amplifier in the experimental measurements.

The aggregate numerical simulation data of Figure 5.1 is also explored by way of the phase space representation in Figure 5.3. The phase space has as many dimensions as state variables, but the viewing is restricted to the dominant contributors of the first three basis function modal coordinates q_1, q_2, q_3 and their respective time derivatives $\dot{q}_1, \dot{q}_2, \dot{q}_3$. Figures 5.3a to 5.3d are all plotted with q_1 and $\dot{q}_1$ in the horizontal plane along with $q_2, \dot{q}_2, q_3$, and $\dot{q}_3$ on the vertical axis, respectively. Each closed loop is a steady-state periodic orbit corresponding to an operating amplitude and frequency.

5.3 Discussion

The experimental measurements in Figure 5.1a reveal interesting features in the dynamic behavior of the cantilever as it is driven by increasing harmonic excitation amplitude. At the lowest drive amplitude, the response amplitude frequency sweep displays linear behavior: a symmetric resonance peak over the first contact resonance frequency. With increasing drive amplitude, the response amplitude of the resonance peak increases, but the frequency of the resonance peak decreases – a nonlinear softening effect. Once a certain drive amplitude threshold is crossed (3.0 mW blueDrive input amplitude), the response amplitude of the

resonance peak itself climaxes and then decreases with increasing drive amplitude. Explaining this final feature is the main target of this investigation.

Simulations of the cantilever-sample system in Figures 5.1b and 5.1c allows one to look behind the AFM measurement features and into the accompanying dynamics at play. The cantilever slope first harmonic amplitude frequency sweeps in Figure 5.1b match the on-resonance behavior shown in the experimental measurements (black background lines). There is a linear response at low drive amplitude, a nonlinear softening at moderate drive amplitude, and a climax followed by a decrease in response amplitude at high drive amplitude. Comparing this to the features of the maximum displacements in Figure 5.1c throughout the same simulated frequency sweeps, one may notice that the climax of the cantilever slope first harmonic amplitude coincides with the onset of tip-sample detachment. Furthermore, though the linear and nonlinear softening features are represented in the maximum deflection, the climax and decrease in response amplitude is not.

To understand why this difference in features between slope and deflection exist, one may first look to the deflection and slope shapes of Figures 5.2a to 5.2d. The low operating amplitude deflection shapes (blue solid lines) in Figure 5.2a appear to be nearly identical to the analytical first eigenfunction of the cantilever-sample system (red dashed lines). When compared to the slope shapes of Figure 5.2c, one might expect that a scalar quantity could be assigned to map from slope to deflection at any point along the length of the cantilever. This is the standard approach for extracting deflection measurements in most AFM operating modes. However, at high operating amplitudes of Figures 5.2b and 5.2d, such a scalar connection is no longer preserved. Interestingly, the slope values near the free end of the cantilever have the same sign at both extremes of the steady state motion, so a mapping from slope to deflection at points in this region is no longer unique.

Further explanation of the discrepancy between slope and displacement is found through the frequency space breakdown of cantilever motion at the location of the probe tip shown in Figures 5.2e to 5.2h. The low operating amplitude probe tip path in Figure 5.2e appears to be a single sinusoid, and since it has been shown that deflection and slope about static equilibrium share a scalar relationship, this is confirmed in the frequency domain (FFT) of the slope response in Figure 5.2g. At high operating amplitude near resonance in Figure 5.2f, the probe

tip motion is more complex and even paths above the sample surface. Not surprisingly, the frequency domain of the slope amplitudes echo the complexity and reveal higher harmonics, or dynamics at multiples of the operating frequency, at play. This is crucial because the lock-in amplifier used to monitor the photodiode output during frequency sweeps is set to only observe dynamics coinciding with the drive frequency. In the standard measurement configuration, any other frequency content, for example higher harmonics of cantilever motion, are not observed.

Finally, one can turn to nonlinear dynamics for an additional perspective on the behavior. In a recent unification of nonlinear normal mode (NNM) definitions, Haller and Ponsioen state that a NNM is a "recurrent motion with a discrete Fourier spectrum of [...] frequencies" for general dissipative systems [112]. This is a relaxation of prior NNM definitions from Rosenberg [113] and Shaw and Pierre [114] which applies to a broader scope of dynamical systems and encompasses fixed points, periodic orbits, and invariant tori realizations of NNMs. In the simulations of Figure 5.1 projected onto the phase space sets of Figure 5.3, each steady-state periodic orbit is a NNM corresponding to a specific operating amplitude and frequency. One can consider the collection of simulated NNMs as a family of periodic orbits (FPO), which appears to be constrained to a manifold in phase space that can be parametrized by the state variables $q_1, \dot{q}_1$ of the first basis function. While NNM analysis in prior literature can be employed to investigate the transient dynamics settling to individual NNMs of the FPO, the FPO itself may be a useful tool in model order reduction for steady-state periodic orbit analysis to reduce a model from many degrees of freedom (e.g. 10 in simulations of Figures 5.1 and 5.3) to few or one (e.g. the first basis function of state variables q_1 and $\dot{q}_1$).

Tip-sample detachment is detrimental to CR-AFM measurements and imaging. Techniques which attempt to use cantilever amplitude to predict material properties depend on a unique mapping between the photodiode detector amplitude and the cantilever deflection amplitude, which is seen to erode at increasing operating amplitude near resonance. Even when resonance frequency is the only observable of interest, tracking of it via both phase-locked loops (PLL) and dual A/C resonance tracking (DART) suffer from the presence of detachment by incorrectly identifying the fundamental contact resonance frequency due to the severe nonlinearities present. Lastly, the AFM probe tip likely deforms at an expedited rate as it is

hammering against the surface during tip-sample detachment cycles, which negatively affects property measurements depending on constant tip geometry.

5.4 Conclusion

In summary, CR-AFM users must be aware of the potential for detachment of the tip from the sample. Figure 5.4 provides a guide for the different regimes of linear, nonlinear softening, and tip-sample detachment that can be observed while taking measurements or imaging. In the linear regime of low operating amplitude, the probe tip remains indented into the sample; it oscillates as a single-frequency sinusoid, and resonance peaks do not shift in frequency with varying operating amplitudes. At moderate operating amplitude, though the probe tip may remain in contact with the sample, the presence of higher harmonics and nonlinear softening of the resonance peak distorts measurements and should be taken as a signal of caution. If operating amplitude continues to increase, it may exceed a threshold above which detachment can occur. This tip-sample detachment regime is observable in-situ by the characteristic climax and decrease of resonance peak in the slope response first harmonic amplitude frequency sweeps, and is likely coupled to probe tip damage and standard CR-AFM, PFM, or ESM analysis techniques cannot be applied for data interpretation.

5.5 Materials and methods

5.5.1 AFM measurements

An AFM utilizes a nanometer-scale microscopy technique that consists of a sharp tip mounted on a microcantilever to probe a sample surface, as shown in Figure 5.5. Measurements were conducted using a Cypher S AFM microscope (Asylum Research, an Oxford Instruments Company, Santa Barbara, CA, USA) with a NCLAu AFM cantilever (NANOSENSORS, Neuchatel, Switzerland) on a silicon sample. This AFM system is equipped with Asylum Research's blueDrive Photothermal Excitation module for laser-based excitation of the cantilever.

The optical lever sensitivity (OLS) corresponding to the static cantilever beam shape with a point load at the tip was calculated from a force displacement curve [115] on the

silicon sample. The thermal method [116] was then used to calculate the static cantilever bending stiffness. To study the process of tip detachment, the measurement algorithm sweeps through drive frequencies (low to high, then high to low) at selected drive amplitudes near the first contact resonance frequency of the cantilever-sample system. The cantilever position was recorded with an optical lever system consisting of a detection laser and a quadrant photodiode. The photodiode signal was converted into amplitude and phase at the drive frequency using a lock-in amplifier.

The OLS resulting from the above calibration procedure is only valid for quasistatic bending of the cantilever or the very similar shape of the first freely vibrating eigenmode. It does not apply to the surface coupled resonances that are the focus of this study. Optical lever systems are predominantly sensitive to changes in cantilever slope. Since the cantilever is deforming in a known shape during the OLS calibration, it is only a matter of multiplying the observed OLS by a ratio of the deflection to slope for a cantilever deforming under a point load applied at the location of the probe tip (assumed from manufacturer specifications) to extract a calibration parameter that can convert between photodiode voltage and cantilever slope. This provides a calibration parameter that remains valid in all measurement circumstances.

5.5.2 Analytical model

The core of the computational exploration is the partial differential equation (PDE) governing the dynamics of the AFM cantilever. At rest, the equilibrium indentation Δ^* is defined as:

$$\Delta^* = -w^*(L_1) - Z, \tag{5.1}$$

where $w^*(L1)$ is the equilibrium deflection of the cantilever at the location of the probe tip L_1, and Z is the undeflected tip position (upward) relative to the undeformed sample surface. While vibrating, the dynamic indentation Δ_{dyn} is defined as:

$$\Delta_{dyn} = \Delta^* - u(L_1, t), \tag{5.2}$$

where $u(L_1, t)$ is the deflection of the cantilever about the equilibrium at the location of the probe tip. The tip-sample interaction F_{TS} is rooted in the Derjaguin, Muller, and Toporov (DMT) model of adhesive contact between particles [117], but modified via works by Shaik et al. [118] to linearize the adhesive regime and Labuda et al. [119] to replace the standard Hertzian indentation model by a generalized Sneddon law interaction for a variety of tip geometries [120]. It is defined as:

$$F_{TS}(\Delta_{dyn}) = \begin{cases} 0 & -\Delta_{dyn} \geq g_{adh} \\ -F_{adh} + \frac{F_{adh}}{g_{adh}}(-\Delta_{dyn}) & g_{adh} > -\Delta_{dyn} \geq 0 \\ -F_{adh} + \alpha_{TS}{\Delta_{dyn}}^{P} & \Delta_{dyn} > 0, \end{cases} \tag{5.3}$$

where F_{adh} is the maximum adhesive force, g_{adh} is the range of the linear attractive region, α_{TS} is the indentation coefficient, and P is the parameter controlling the probe tip geometry. Asylum Research's blueDrive Photothermal Excitation of the AFM cantilever is approximated as a harmonic bending moment couple of amplitude M_{bD} and frequency Ω_{bD} separated by double the laser spot radius r_{bD} and centered at the laser spot location L_{bD}, measured from the base of the cantilever. Altogether, the equation of motion PDE is assembled as:

$$\begin{aligned} &\rho A\ddot{u}(x,t) + c_{cantilever}\dot{u}(x,t) + EI\left[u(x,t) + w^*(x)\right] \\ &\quad = M_{bD}\sin(\Omega_{bD}t)\left[\delta(x - L_{bD} - r_{bD}) - \delta(x - L_{bD} + r_{bD})\right] + F_{TS}\left(\Delta_{dyn}\right)\delta(x - L_1), \end{aligned} \tag{5.4}$$

where $u(x,t)$ is the cantilever deflection at position x and time t about equilibrium, $w^*(x)$ is the equilibrium shape of the cantilever, ρA is the mass per unit length, $c_{cantilever}$ is the linear viscous damping coefficient, and EI is the cantilever flexural rigidity. Dots over variables refer to time derivatives, while primes denote partial derivatives with respect to the position along the cantilever length.

5.5.3 Parameter identification

Careful identification of system parameters is critical for a meaningful comparison of simulations to measurements. Fortunately, much of what is needed is common practice to AFM users, and the following sequence steps through extraction of relevant of quantities predominantly via techniques implemented in Hurley et al. [90]. These are collected for reference in Table 5.1. First, linear vibration cantilever modes are chosen as an orthogonal basis set upon which to project the PDE, defined as [14]:

$$\Phi_{\mathrm{i}}(x) = C_{\mathrm{i}}\left[\sin\beta_{\mathrm{i}}x - \sinh\beta_{\mathrm{i}}x - \left(\frac{\sin\beta_{\mathrm{i}}L + \sinh\beta_{\mathrm{i}}L}{\cos\beta_{\mathrm{i}}L + \cosh\beta_{\mathrm{i}}L}\right)(\cos\beta_{\mathrm{i}}x - \cosh\beta_{\mathrm{i}}x)\right], \tag{5.5}$$

and normalized by $\Phi_{\mathrm{i}}(L_1) = 1 \;\forall\; \mathrm{i} = 1, 2, 3, ..., N$, where N is the number of basis functions used in the discretization set, and C_{i} is the basis coefficient used to satisfy such normalization. The basis set is used to separate the deflection variable into spatial and temporal portions as follows:

$$u(x,t) \approx \sum_{\mathrm{i}}^{N} \Phi_{\mathrm{i}}(x) q_{\mathrm{i}}(t), \tag{5.6}$$

where $q_{\mathrm{i}}(t)$ is the time-varying modal coefficient of the ith basis function. This discretization step is pertinent not only to parameter identification, but also the dynamic simulations.

Measurements of the resonance frequencies for both the free and contact cases allows the identification of critical stiffness quantities required for converting raw experimental output into physical quantities. The dispersion relation for wave number and frequency is given as:

$$(\beta_n L)^2 = 2\pi f_n \sqrt{\frac{\rho A L^4}{EI}}, \tag{5.7}$$

where β_n and f_n are the wavenumber and resonance frequency of the nth mode, respectively [14]. Note that this is also valid for the cantilever in contact with the sample using the contact wavenumber β_n^c and contact resonance frequency f_n^c of the nth mode. As such, a ratio can be constructed between the first free vibration mode and the first contact vibration mode:

$$(\beta_n^c L) = (\beta_1 L)\sqrt{\frac{f_n^c}{f_1}}. \tag{5.8}$$

This is used to back out $\beta_1^c L$ and β_2^c from the measured frequencies f_1, f_1^c, and f_2^c as well as the known $\beta_1 L = 1.875$ from free vibration theory of cantilevers [14]. By defining the relative tip position ratio as:

$$\gamma = \frac{L_1}{L}, \tag{5.9}$$

and the relative spring constant ratio as:

$$k_{ratio} = \frac{k_{sample}}{k_{cantilever}}, \tag{5.10}$$

where k_{sample} and $k_{cantilever}$ are the equivalent linear spring constants of the sample at equilibrium and the cantilever, respectively, the characteristic equation is assembled as [121]:

$$k_{ratio} = \frac{2}{3}(\beta_n^c L\gamma)^3 \frac{1 + \cos\beta_n^c L \cosh\beta_n^c L}{D_r} \tag{5.11}$$

where

$$\begin{aligned} D_r = {} & [\sin\beta_n^c L(1-\gamma)\cosh\beta_n^c L(1-\gamma) - \cos\beta_n^c L(1-\gamma)\sinh\beta_n^c L(1-\gamma)] * \\ & (1 - \cos\beta_n^c L\gamma\cosh\beta_n^c L\gamma) - (\sin\beta_n^c L\gamma\cosh\beta_n^c L\gamma - \cos\beta_n^c L\gamma\sinh\beta_n^c L\gamma) * \\ & [1 + \cos\beta_n^c L(1-\gamma)\cosh\beta_n^c L(1-\gamma)]\,. \end{aligned} \tag{5.12}$$

This relationship has a unique physically-relevant solution valid for both the first and second contact modes, thus determining k_{ratio} and γ for the system. The cantilever spring constant is defined as [90]:

$$k_{cantilever} = \frac{3EI}{{L_1}^3}, \tag{5.13}$$

and the first free vibrating mode stiffness as [122]:

$$k_{1,free} = EI \int_0^L \Phi_1(x)\Phi_1(x)dx, \tag{5.14}$$

allowing one to solve for $k_{cantilever}$ and the flexural rigidity EI. Combining these with previous parameter results allow for the calculation of the sample stiffness k_{sample} and the mass per

unit length ρA. Next, combining the latter term with the quality factor Q of the first contact mode, the linear viscous cantilever damping is defined as:

$$c_{cantilever} = \frac{2\pi f_1^c}{\rho A Q}. \tag{5.15}$$

Remaining system parameters relating to the tip-sample indentation model of Equation (5.3) are defined in conjunction with experimental observables. The adhesion force ${F_{adh}}^*$ and adhesion gap g_{adh} are identified from the retraction force-distance curve taken just before vibration sweeps. While g_{adh} is observed directly, F_{adh} requires multiplication with $k_{cantilever}$ and the inverse OLS to convert from voltage to force. Similarly, the equilibrium tip-sample force ${F_{TS}}^*$ uses the same conversion to interpret the setpoint voltage as a force. Finally, the indentation power P is tuned to match the softened resonance frequency at the response amplitude climax of Figure 5.1a, allowing the subsequent calculation of the coefficient α_{TS}, equilibrium indentation Δ^*, and undeflected tip position Z.

Simulations

All simulations were conducted in MATLAB using an ordinary differential equation solver to evaluate time-marching integration. For each frequency sweep set in Figure 5.1, the system was simulated at a selected bending moment couple drive amplitude until steady-state, at which point the frequency was stepped incrementally up or down using final state variable values from the previous simulation point as initial conditions. A fast Fourier transform of the steady-state time-domain slope response of the AFM cantilever at the location of the probe tip is used to extract the first harmonic amplitude for comparison with measurements. Using the full cantilever response, stroboscopic sampling throughout a period provides explanation of the shapes experienced during simulations. Lastly, orbits of the state variables q_i and $\dot{q}_\mathrm{i}$ for $\mathrm{i} = 1, 2, 3$ are plotted to examine evidence and behavior of NNMs.

Supplementary information

Additional AFM measurements identifying the tip-sample detachment signature are provided in Figure 5.6. These were performed using the same Cypher S AFM microscope with an ACLA AFM cantilever (Applied NanoStructures, Inc., Mountain View, CA, USA) on a silicon sample, but driven by a piezoelectric actuator under the sample instead of via photothermal excitation. This leads to less ideal ("forest of peaks") transfer functions and can complicate parameter identification [123], [124].

A second simulation-only example with hypothetical parameter values of Table 5.2 is provided in Figure 5.7. The associated NNMs collected into a FPO is shown in Figure 5.8.

Table 5.1. Parameter identification from AFM measurements

Parameter	Measured	Parameter	Assumed	Parameter	Calculated
$k_{1,free}$	32.8 N/m	L_1	225 μm	$\beta_1^c L$	3.413
f_1	163 kHz	$\beta_1 L$	1.875	$\beta_2^c L$	5.180
f_1^c	540 kHz	L_{bD}	$0.1 \cdot L$	L ($\gamma = L_1/L$)	227 μm (0.99)
f_2^c	1244 kHz	r_{bD}	1 μm	k_{ratio}	16.4
Setpoint	0.2 V			$k_{cantilever}$	31.9 N/m
InvOLS	$1.27e^{-7}$ m/V	Parameter	Tuned	EI	$1.2e^{-10}$ N·m^2
Q	174	P	1.4	k_{sample}	524.0 N/m
g_{Adh}	14 nm			ρA	$5.4e^{-7}$ kg/m
F_{Adh}	9.2 nN			$c_{cantilever}$	0.018 N·s/m
F_{TS}*	810 nN			α_{TS}	$1.1e^6$ N/m^P
				Δ*	2.19 nm

Table 5.2. Parameter values for hypothetical simulation example

Parameter	Value
L ($\gamma = L_1/L$)	300 µm (0.97)
L_{bD}	$0.1 \cdot L$
h	4 µm
b	20 µm
ρ	2330 kg·m^{-3}
E	169 GPa
ν	0.278
R	10 nm
E_{sample}	10 GPa
ν_{sample}	0.3
F_{Adh}	20 nm
g_{adh}	10 nm
P	1.5 (Hertz)
Q	100
F_{TS}	200 nN

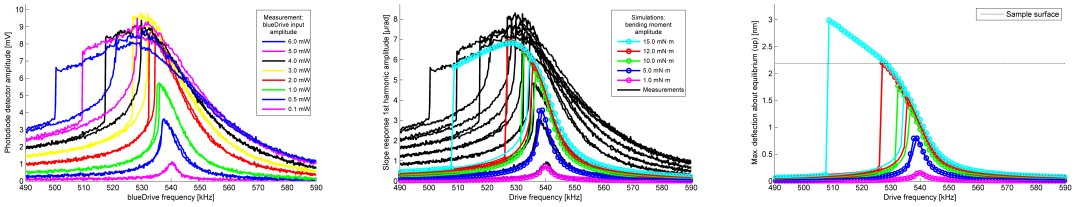

(a) (b) (c)

Figure 5.1. (a) AFM frequency sweep measurements depicted by photodiode detector amplitudes versus blueDrive excitation frequency. Colored curves (sweep up and down) identify various blueDrive input amplitudes. (b)-(c) Dynamic simulations of cantilever driven about contact resonance frequency using ten free cantilever eigenfunctions as a basis set. Measurement data is converted to slope response and depicted as black curves. Simulation data points are shown as colored circles, closed for increasing frequency sweep and open for decreasing, with lines connecting to elucidate jumps between periodic solution branches for both slope response first harmonic amplitudes (b) and maximum probe deflection about equilibrium (c). Undeformed sample surface location is indicated as a threshold for tip-sample detachment.

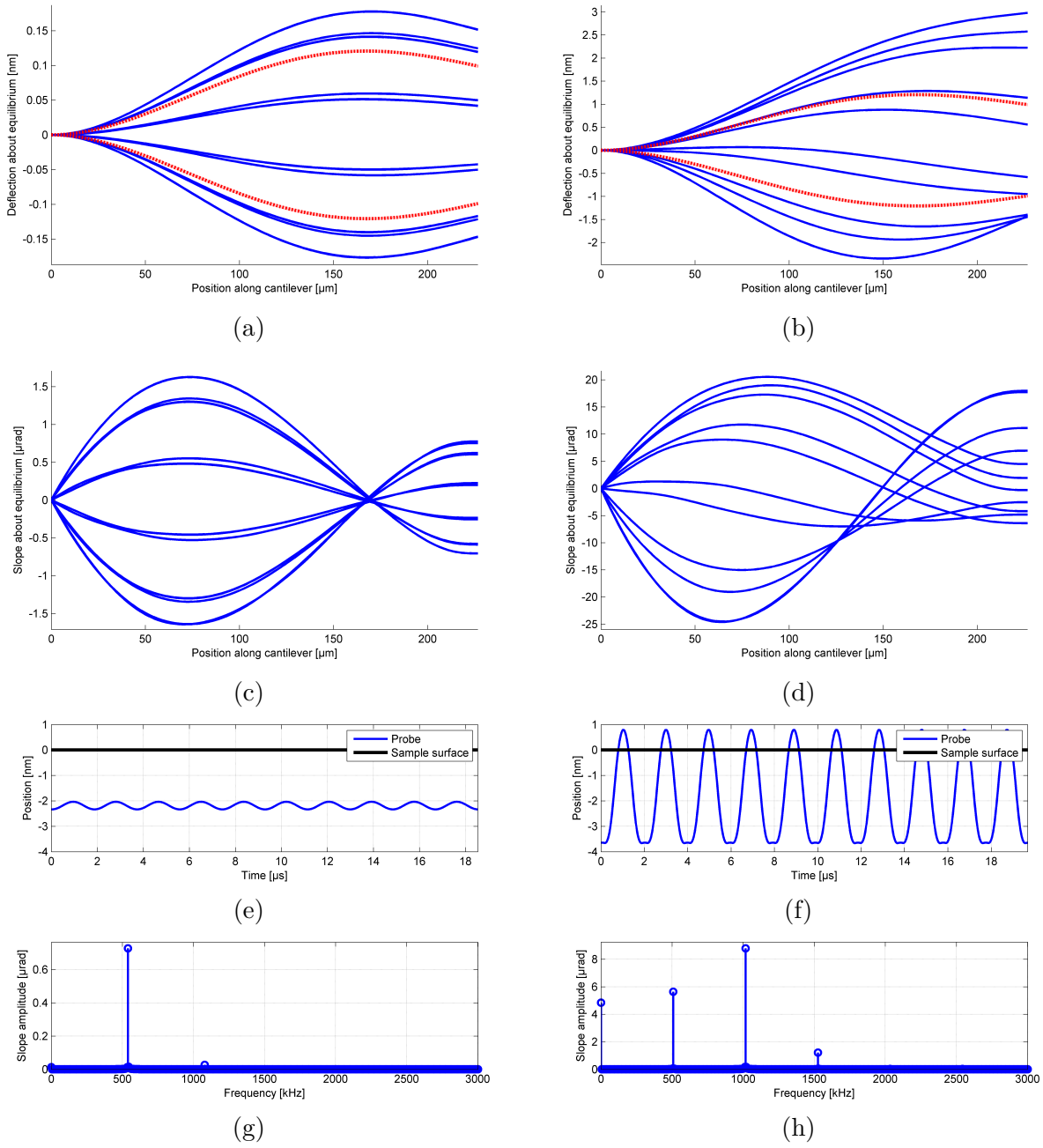

Figure 5.2. Detailed dynamic behavior of two numerical simulations at steady-state and at resonance: low bending moment amplitude of 1 N·m at 540 kHz (left column), and high bending moment amplitude of 15 N·m at 508.7 kHz (right column). Stroboscopic depiction of cantilever deflection (a),(b) and slope (c),(d) shapes about static equilibrium (blue, solid), with linear eigenfunction of cantilever-sample system (red, dashed) overlay. Probe tip path in time (e),(f) with depiction of undeformed sample surface location for reference. Frequency domain (FFT) of slope response (g),(h) to connect with direct observables in CR-AFM measurements.

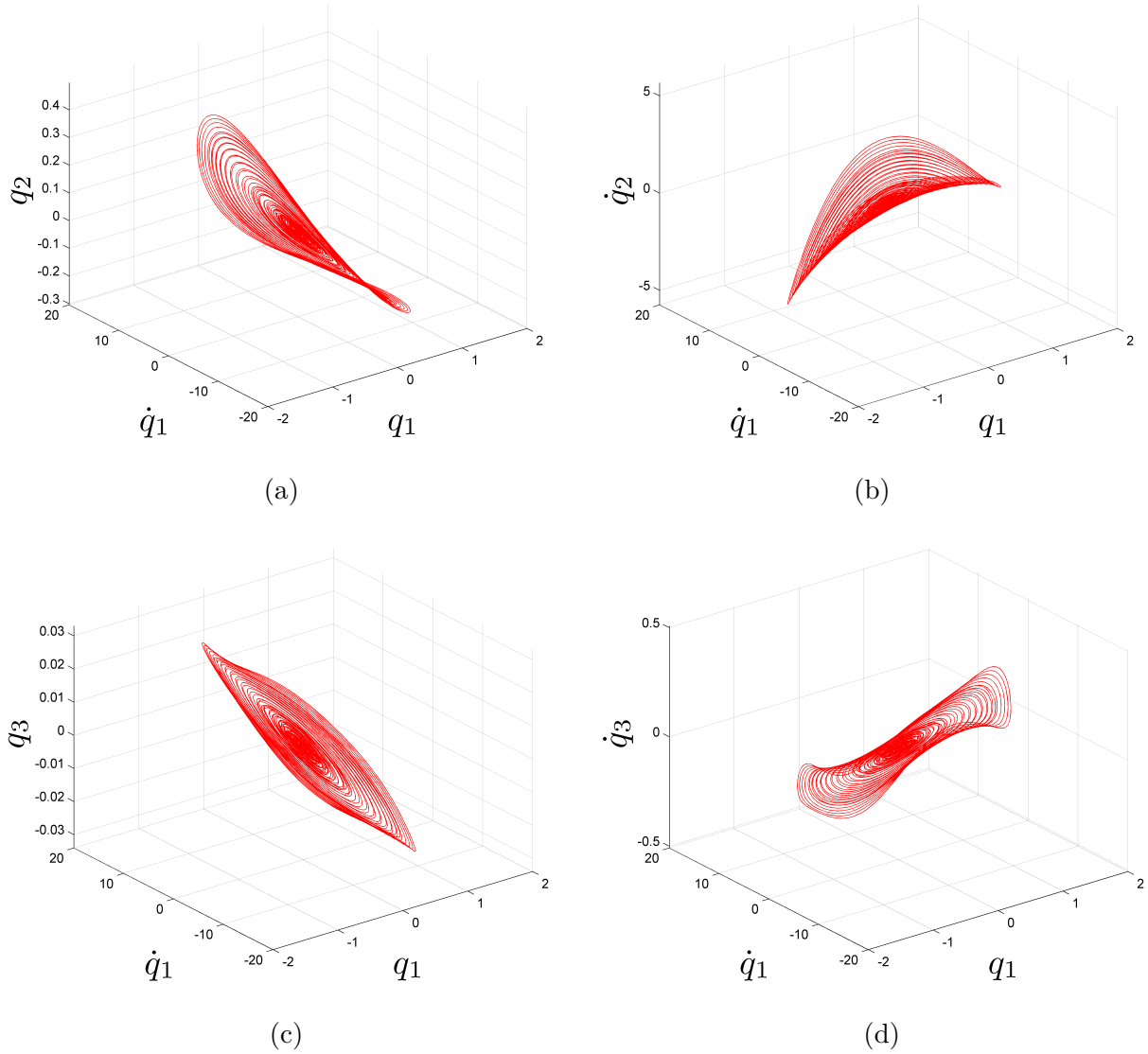

Figure 5.3. Steady-state periodic orbits (nonlinear normal modes) from simulations in Figure 5.1 projected onto phase space comprised of state variables. Second basis function displacement q_2 (a) and velocity $\dot{q}_2$ (b), as well as third basis function displacement q_3 (c) and velocity $\dot{q}_3$ (d) are plotted against first basis function displacement q_1 and velocity $\dot{q}_1$.

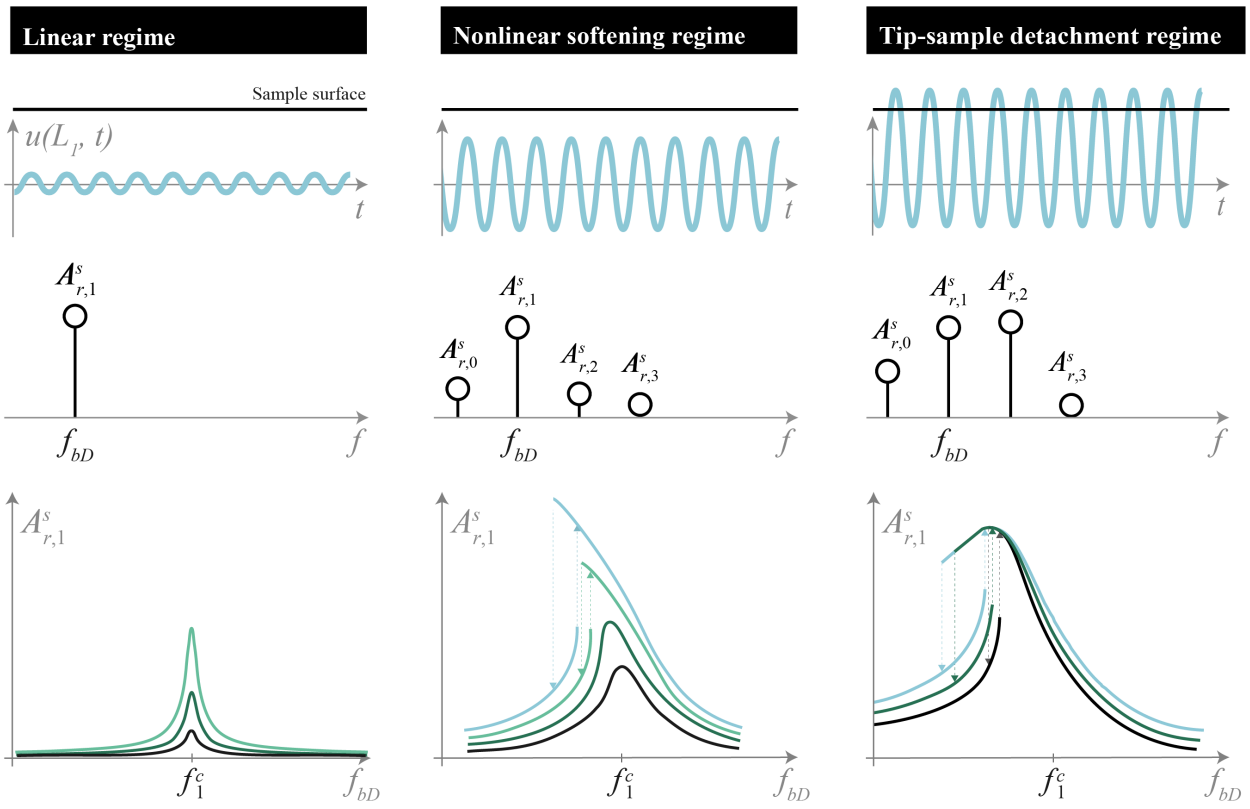

Figure 5.4. Infographic for summary of linear, nonlinear softening, and tip-sample detachment regimes for qualitative AFM cantilever behavior corresponding to low, moderate, and high drive amplitude excitation, respectively. Top plots depict representations of AFM probe tip path in time indented below sample surface, middle plots show representations of harmonic contributions to slope response amplitude of cantilever above probe tip, and bottom plots provide representations of slope response first harmonic amplitudes versus drive frequencies at various drive amplitudes.

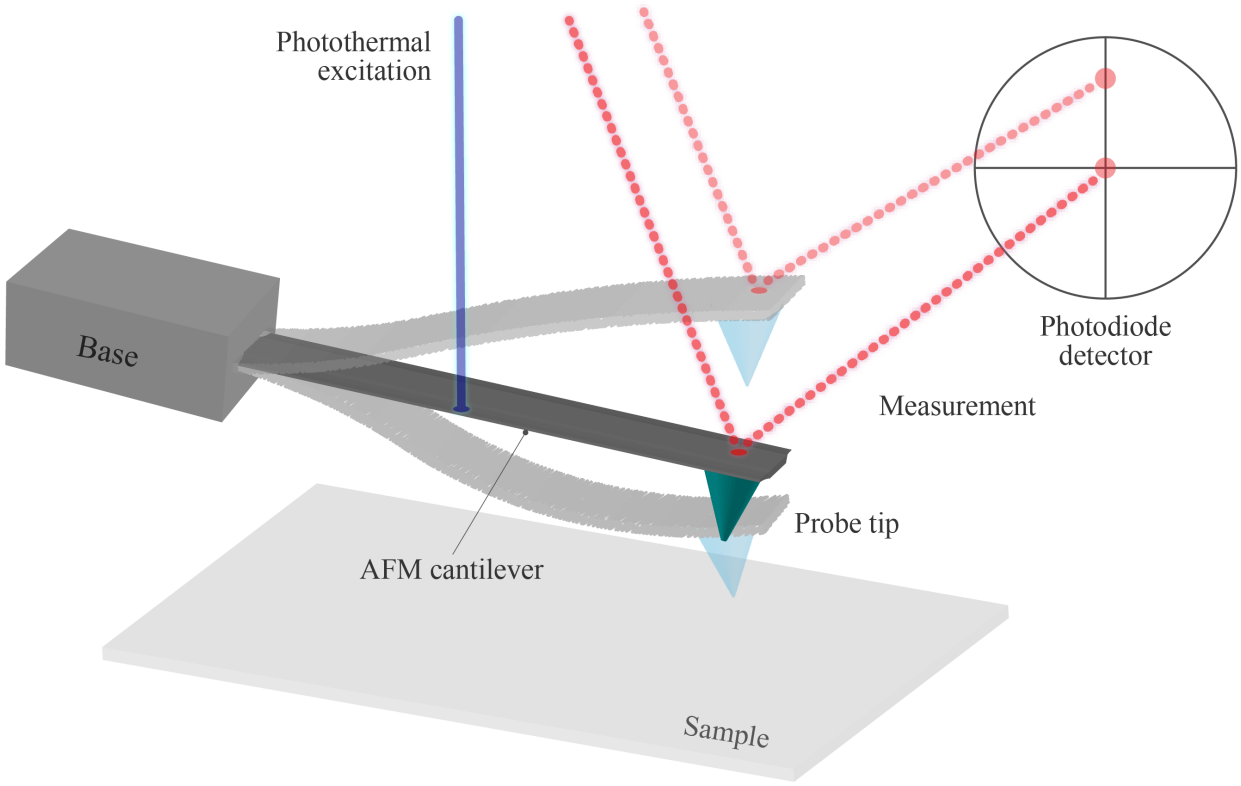

Figure 5.5. CR-AFM schematic for equipment layout depicting the key components for excitation and measurement. The latter of which is performed with a laser reflecting off of the top surface of the cantilever and onto a photodiode detector. Transparent AFM cantilever shapes are included to suggest the motion of the device during vibration response. Though the laser spot change on the detector appears to the naked eye as a resultant of the cantilever deflection, the vertical scaling is greatly exaggerated for clarity; it is actually the slope change of the cantilever which significantly dominates the detection.

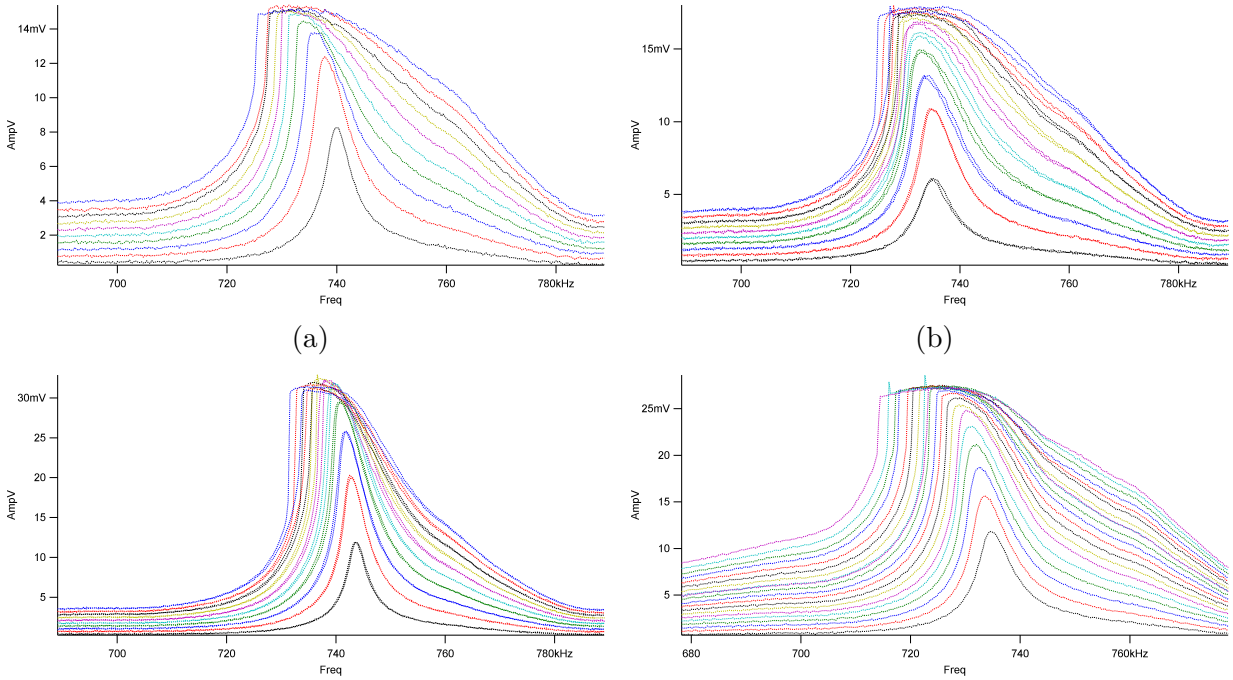

Figure 5.6. Additional evidence of tip-sample detachment on silicon samples at various piezoelectric drive amplitudes, shown as photodiode detector amplitude vs drive frequency.

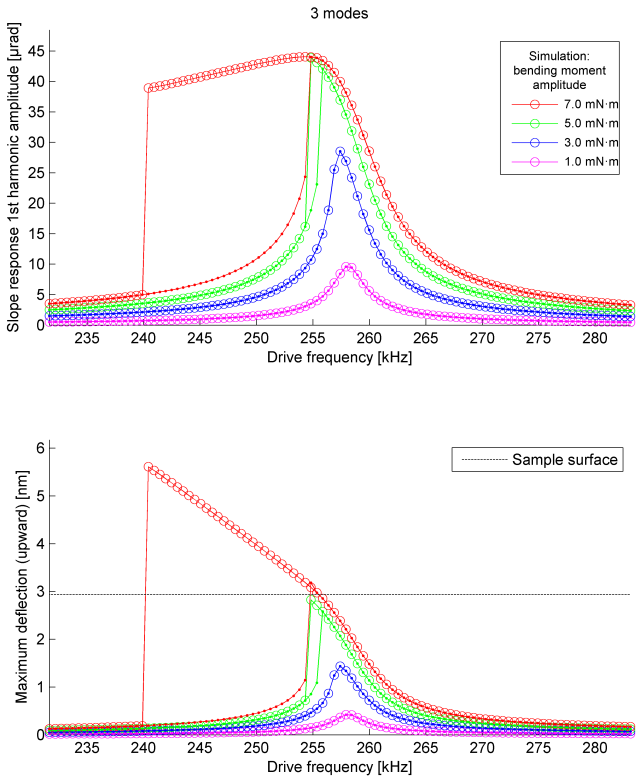

Figure 5.7. Similar to simulations from Figure 5.1, dynamic simulations of a hypothetical cantilever system (parameter values in Table 5.2) driven about contact resonance frequency using only three free cantilever eigenfunctions as a basis set. Slope response first harmonic amplitude versus drive frequency (upper) and maximum probe displacement versus drive frequency (lower).

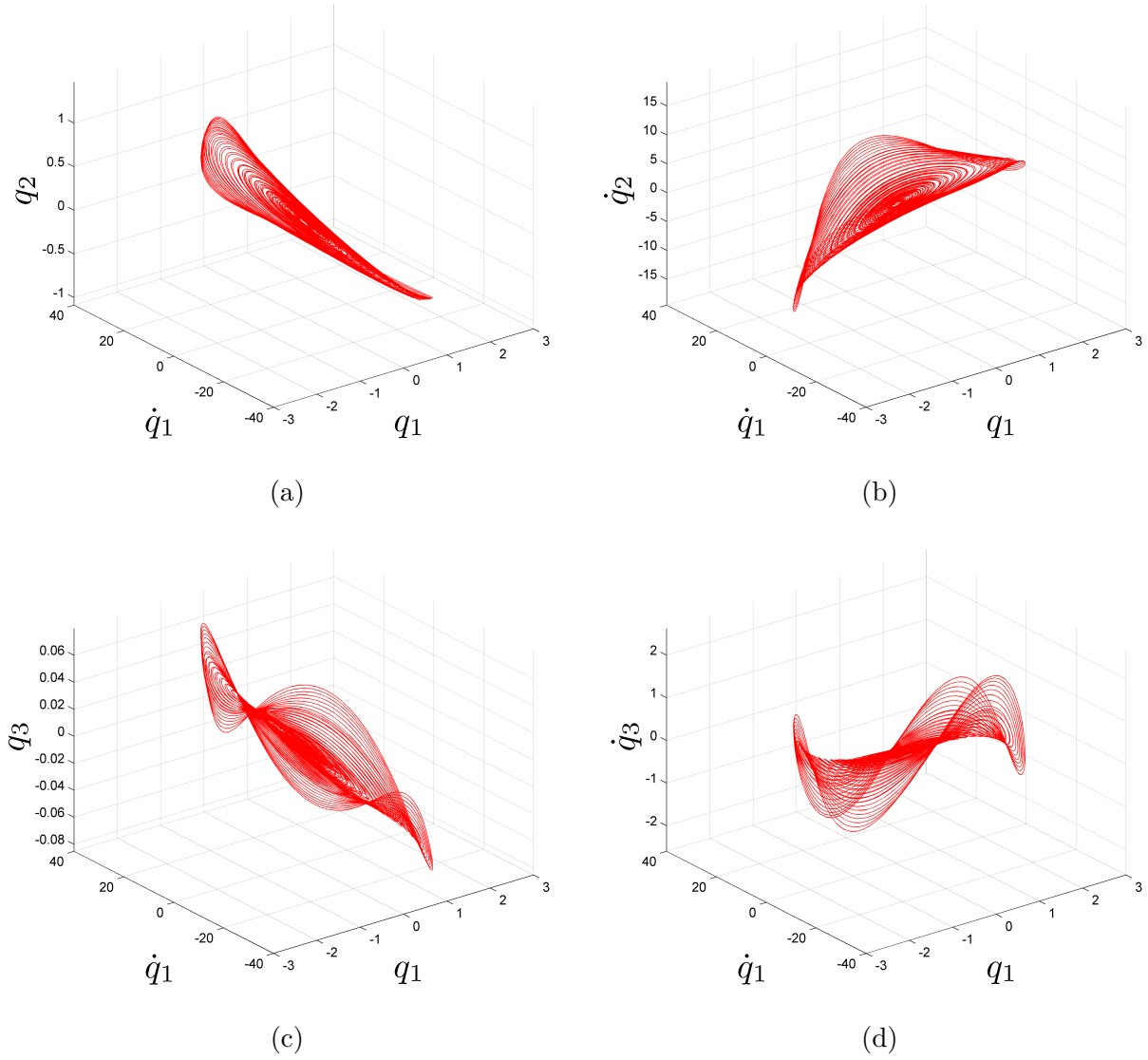

Figure 5.8. Steady-state periodic orbits (nonlinear normal modes) from hypothetical simulations (parameter values in Table 5.2) in Figure 5.7 projected onto phase space comprised of state variables. Second basis function displacement q_2 (a) and velocity $\dot{q}_2$ (b), as well as third basis function displacement q_3 (c) and velocity $\dot{q}_3$ (d) are plotted against first basis function displacement q_1 and velocity $\dot{q}_1$.

6. CONCLUSION

In closing, this chapter provides final thoughts on the dissertation projects as well as a look forward to future research work building on the previous chapters.

6.1 Summary

Chapter 2 provides the framework for solving MEMS device equilibria expediantly in commercially available software packages. Numerical computation in COMSOL Multiphysics® is shown to quantitatively match the results of AUTO for microbeam examples under various multiphysics loadings, but really displays its FEM power when solving for equilibria solutions to devices with complex geometry in 2D and 3D – a necessity in MEMS design. Even as a precursor to dynamical operation, all MEMS research benefits from fundamental understanding of the relationship between quasistatic loading and deformation. There is no quicker or more comprehensive way to solve such equilibria than by numerical continuation, and no more accessible or communicable implementation than through commercial software.

Chapter 3 succeeds in developing a compact analytical model for a MEMS microcantilever capacitive switch and predicting the possible multistability present across the associated set of all physically-realizable system parameter values. The deforming beam element of the devices exhibits three unique (defined via equilibrium solution branches, not by observation) configuration shapes corresponding to three tiers of output capacitance. Depending on system properties and device geometry, operable regions of each configuration may overlap with one, two, or none of the others, and all three can possibly occur with zero actuation. The compact model is a critical contribution to device literature through its capture of all configurations without the need to swap boundary conditions and restric static or dynamic analysis about one configuration at a time.

Chapter 4 brings device-specific simulations and experimental validation of switching behavior to support the previous multistability predictions of the compact model. Experimental reconstructions of microcantilever deformation are the first clear mechanical observation of the multistability in depicting the floating, arc-shaped, and s-shaped configurations. The switching performance of each individual device reconstruction – and moreso the difference

between each one – is shown to be well-captured by simulations in COMSOL Multiphysics® when modeled with individual device geometry measurements. Both the measurements of mechanical deformations as well as the computational approach are contributions to MEMS device research.

Chapter 5 identifies a long-standing nonlinear feature of CR-AFM resonance peaks as a signature of tip-sample detachment at high operating amplitude. Though strictly explored via AFM, this observation is relevant to the MEMS community interested in dynamic methods of stiction release as it is a dynamical indicator of the onset of detachment. For the CR-AFM community, it denotes an observable operating amplitude ceiling to measurement techniques which assume sustained contact between tip and sample.

6.2 Future Work: Dynamic Switching in MEMS Microcantilever Capacitive Switches

Chapters 2 through 4 are concerned with the static equilibria and, to a limited extent, the quasistatic operation of MEMS microcantilever capacitive switches. A more complicated phenomenon is the dynamic switching between stable states and, more specifically, release of a device stiction-failed in the arc- or s-shaped configuration to the floating configuration. Preliminary numerical investigation suggests that there may be valuable insight gained from harmonic electrostatic actuation of the devices, while experimental measurement indicate that there may be a higher-harmonic signature in connection to the CR-AFM detachment studied in Chapter 5.

In the context of electrostatic excitation-induced switching, the knowledge of switching thresholds is often sufficient for normal operation. However, when devices fail due to stiction (i.e. adhesive forces overpower restorative forces), this mechanism for actuation can also be exploited to release devices back into their undeflected state. Primary contributions to stiction repair come from the field of fracture mechanics, where periodic excitation interacts with the energy balance between beam bending and adhesion to propagate a "crack tip" through the seemingly-laminated microcantilever and underlying layer [27], [125].

To best replicate literature results using the foundation presented in earlier chapters, a process is first followed to reconcile the differences in modeling of physical phenomena

based on a similar set of driving assumptions. Next, time-marching simulations provide a preliminary glimpse into the model behavior, and then a nonlinear analysis approach is proposed to describe such computational results. The aim is to identify features of stiction release inaccessible through past approaches.

6.2.1 Modeling

Commonplace in MEMS, the stable equilibria are a resultant of a force-balancing act: electrostatics and adhesion attract the beam to the dielectric-coated electrode, while internal restorative forces and surface repulsion work to push the two objects apart. Now, in a return to governing equations of motion, a reinstatement of time-varying terms provide yet another layer of complexity to the study of system response. The following is a return to Equation (3.3) with associated cantilever boundary conditions, except the voltage actuation is allowed to vary in time, and a linear viscous damping term is present:

$$EI\frac{\partial^4\hat{w}}{\partial\hat{x}^4}+c\frac{\partial\hat{w}}{\partial\hat{t}}+\rho A\frac{\partial^2\hat{w}}{\partial\hat{t}^2}=\frac{\epsilon_0 b\left[\hat{V}(t)\right]^2}{2(a+\frac{d}{\epsilon_r}-\hat{w})^2}+\frac{b\hat{H}}{6\pi(a-\hat{w})^3}\left[1-\left(\frac{\hat{z}_0}{a-\hat{w}}\right)^6\right]. \tag{6.1}$$

To look at a static, stiction-failed device, the continuation technique from Chapter 3 is employed with parameters given in Table 6.1 which are chosen specifically to match earlier works [27], [125]. The first ten parameters are direct connections to literature in order to establish the same geometric layout and material properties. The final two parameters, however, are unique to the surface interaction force definition followed in this report, and are designed to enforce an s-shaped configuration at zero applied electrostatic actuation (stiction). This exact s-shaped condition, determined through a similar continuation approach to that of Appendix 3.A, has approximately half its length unstuck from the dielectric layer, as depicted in Figure 6.1. Herein, unstuck refers to region(s) of the microcantilever whose interaction with the surface interaction force is purely adhesive, while stuck refers to those region(s) in pure repulsion. Thus, the zero pressure gap $\hat{z}_0$ is crossed at nearly half the microcantilever length.

6.2.2 Harmonic and pulse loading simulations

Time-integration solutions to the PDE of Equation 6.1 provide an initial tool to explore system response to dynamic electrostatic actuation. These simulations, carried out using the ode45 function in MATLAB, follow a similar finite difference spatial discretization scheme to that of Appendix 3.A. Each evaluation of the model begins with initial conditions of Figure 6.1, and step sequentially forward in time until either a stop condition or the maximum time (0.5 ms) is met. In this case, the stop condition is a release criterion, where the algorithm halts if each of the hundreds of finite difference nodes are all at least 100 nm away from the dielectric surface. It provides a soft restriction on the complexity of dynamic solutions in order to examine a binary classification of the results: the device remains stiction-failed under the prescribed loading conditions for the duration considered, or it releases from the s-shaped stiction configuration.

Harmonic and (half-sine) pulse electrostatic actuation are the two dynamic loading conditions considered in an attempt to release stiction-failed devices. For the case of harmonic loading, the voltage term of Equation 6.1 becomes

$$\hat{V}_{harmonic}(t) = \hat{V}_0 sin(\Omega t) \implies \left[\hat{V}_{harmonic}(t)\right]^2 = \frac{\hat{V}_0^2}{2}\left[1 - cos(2\Omega t)\right], \tag{6.2}$$

where $\hat{V}_0$ is the voltage amplitude and Ω is the drive frequency. Alternatively, in the case of the pulse loading, the voltage term of Equation 6.1 becomes

$$\hat{V}_{pulse}(t) = \begin{cases} \hat{V}_0 sin(\frac{\pi}{T_p}t), & 0 \leq t < T_p \\ 0, & t \geq T_p, \end{cases} \tag{6.3}$$

where T_p is the duration of the pulse. Though the pulse loading is unexplored, early results for harmonic loading are shown in Figure 6.2. Contrasting the more assumption-laden approaches from literature, complex features of the boundaries between released and stiction-failed conditions are apparent.

6.2.3 Goals and remaining challenges

Several important topics remain unsolved in the preliminary steps outlined for dynamic release from stiction-failure. Damping, electrostatic loading, experimentation, and foundational analysis are all enticing directions for future research.

Damping: the linear viscous term in Equation (6.1) is sufficient to match with specific literature results, but any discussion of equilibria release or final resting states in dynamic operation will likely have a sensitive dependence on the choice of damping model. Previous MEMS analysis indicates the need to consider the squeeze-film damping phenomenon, in which fluid flow models are incorporated to understand how the surrounding medium flows out (in) as the microcantilever approaches (retracts from) the dielectric surface [126]. A compact squeeze-film damping model may take the place of the linear viscous term in Equation (6.1) as a precursor to any rigorous practical comparison. As research output, two main inquiries remain: what is the minimum damping complexity needed to explore switching behavior, and can one use this model choice to extract parameters experimentally?

Harmonic and pulse loading simulations: discussions of loading, stiction release criteria, and final resting states are all crucial to success of the dynamic electrostatic actuation project. As mentioned, the preliminary results of Figure 6.2 are strictly for harmonic electrostatic actuation. Successive periods of the harmonic loading continue to intermittently pull the microcantilever toward the substrate, against the intended motion of stiction release, but with the aim of building energy for the system to jump to another stable equilibrium. Alternatively, pulse (half-sine) loading might be an attractive option for a quicker transition, though possibly at the expense of a higher peak voltage requirement. Exploring either loading condition requires a clear directive for articulating when a microcantilever has released from stiction failure, and where it rests afterward. The simulations of Figure 6.2 end when the microcantilever has separated a sufficient distance from the dielectric layer below, but it is unknown if it, through the breadth of dynamic behavior accessible to the model, returns to the failed configuration after some amount of time. A larger scope of this concern is of determining all final resting states for various loading conditions. An understanding in

this perspective will guide experimental measurement choices, as well as inform analytical approaches through comparison.

Experimentation: as a complement to the simulation-driven search through dynamic electrostatic loading considerations, experimental measurements of device stiction and release will be performed. The same batch of devices from the prior switching threshold investigation contains many that come out of fabrication already stiction failed, as shown for an example device in Figure 6.3. These optical microscope scans can be used in conjunction with the LDV system to identify stiction-failed devices from the microcantilever shape, repair them via dynamic electrostatic actuation, and then reimage each one to be sure that stiction release is successful. By mapping the microcantilever profile and tracking the electrostatic loading, broad regions of harmonic loading simulations according to Figure 6.2, as well as the pulse loading counterpart, can be confirmed.

Two critical challenges remain with regard to experimental contributions to this project: imposing stiction failure on released devices, and the ability to connect results from device measurements back to simulation and analysis results. With regard to the former, manual manipulation via pointed probes is an option, but it comes with a risk of partial damage or even complete destruction of the microcantilever. Alternatively, electrostatic actuation (DC) could enforce the s-shaped configuration of the microcantilever, though dielectric charging is a significant concern to manage. Even if reliable access to stiction-failed devices is ascertained, failed either from manipulation or from the original fabrication process, a comparison between measurements and either simulations or analysis remains a research hurdle. Microcantilever failure may be in arc-shaped configurations rather than s-shaped, the failure may be asymmetric with regard to the lateral position, and the unstuck segment found through measurement may contrast that of the mathematically ideal scenario.

Analytical explanation: the results from simulations and experiments are of strong interest, but require some semblance of analytical justification in order to have applicability outside a narrow set of system and loading parameters. Using Equations (6.1) and (6.2) along with the preliminary results of Figure 6.3 as motivation, the root of the dynamic switching behavior may be accessible if treated as an extension of a parametric instability problem from

nonlinear dynamics. This may need to be completed in conjunction with a strong reduced order approach to the spatial discretization of the PDE models.

6.3 Future Work: Nonlinear Normal Modes and Order Reduction in CR-AFM Detachment Dynamics

Many interesting dynamical features have been observed in the numerical simulations of CR-AFM tip-sample detachment in Chapter 5 with potential for analytical explanation and order reduction. By simulating the PDE of Equation 5.4 and plotting the resulting stable periodic orbits corresponding to a sweep of drive frequencies at various drive amplitudes, a family of periodic orbits (FPO) is shown in Figure 5.3. Following the same process but with only three cantilever eigenfunction basis functions, Figures 6.4 to 6.11 detail not only the FPO, but also two examples of trajectories from two selected initial conditions in phase space: one on-manifold and another off-manifold. The on-manifold example of Figures 6.4 to 6.7 show the trajectory broken up into thirds (beginning, middle, and end) in four representations of the six-dimensional phase space of state variables stemming from an initial condition set coinciding with the FPO. The off-manifold example of Figures 6.8 to 6.11 show the same for an initial condition set off of the FPO.

It is clear from the results of Chapter 5 that the FPOs presented seem to fill out a 2D manifold that can be parametrized by the lowest basis function state variables, but the on- and off-manifold initial condition trajectory examples show additional information. From the former, it appears that the trajectory starting on the FPO remains on the FPO as it dynamically transitions to its stable periodic orbit for the applied drive conditions. For the latter, it appears that the trajectory starting off of the FPO quickly approaches the FPO before settling. These are early simulation-based suggestions of invariance and local stability. If evolutions of the system from initial conditions on the FPO stay for all time and those off the FPO approach the FPO quickly, then it is plausible for all pertinent dynamics of the system to be captured by a single-degree-of-freedom (SDOF) nonlinear oscillator constrained to the FPO. It may be possible to use this feature as a tool for order reduction in the exploration of tip-sample detachment in CR-AFM.

6.3.1 Goals and Remaining Challenges

Significant opportunities for future projects are available for constructing and exploring FPOs.

Numerically-constructed FPO for order reduction: stable periodic orbits from numerical simulations have been shown to fill out an FPO when modulating the drive amplitude and frequency. Such numerical FPO could feasibly be applied back to the original PDE as a constraint to reduce it to a SDOF system through parametrizing each state variable by that of the lowest basis function. If successful, this SDOF nonlinear oscillator construction would be an impressive reduction in order for modeling purposes.

Analytically-constructed FPO for order reduction: though more challenging of a conceptual approach, an analytical construction of the FPO would be valuable for design of experiments as there could be a formulaic relationship between system parameters and tip-sample detachment without lengthy time-integration solutions to find stable periodic orbits. It may be possible to build an FPO analytically through local approximation of the nonlinear PDE, and successively relax local restriction to approach large drive amplitude behavior and tip-sample detachment.

Exploration into persistence of FPO properties: an exhaustive investigation into varying system parameters (AFM cantilevers, samples, and actuation methods) would be valuable to CR-AFM detachment research. To this end, generation of FPOs from either suggested previous method as well as their manifold, stability, and invariance properties should hopefully apply for a broad set of system parameters. This would allow for the order reduction goal to be solved robustly.

Table 6.1. Parameters for stiction-failed device analysis

E	160 GPa
I	$\frac{1}{12}bh^3$
ρ	2300 kg m^{-3}
A	$b * h$
ϵ_0	8.8542×10^{-12} m^{-3} kg^{-1} s^4 A^2
b	30 μm
a	2 μm
d	300 nm
ϵ_r	3.9
c	1.89×10^{-4} kg s^{-1} m^{-1}
$\hat{H}$	6×10^{-19} J
$\hat{z}_0$	10 nm

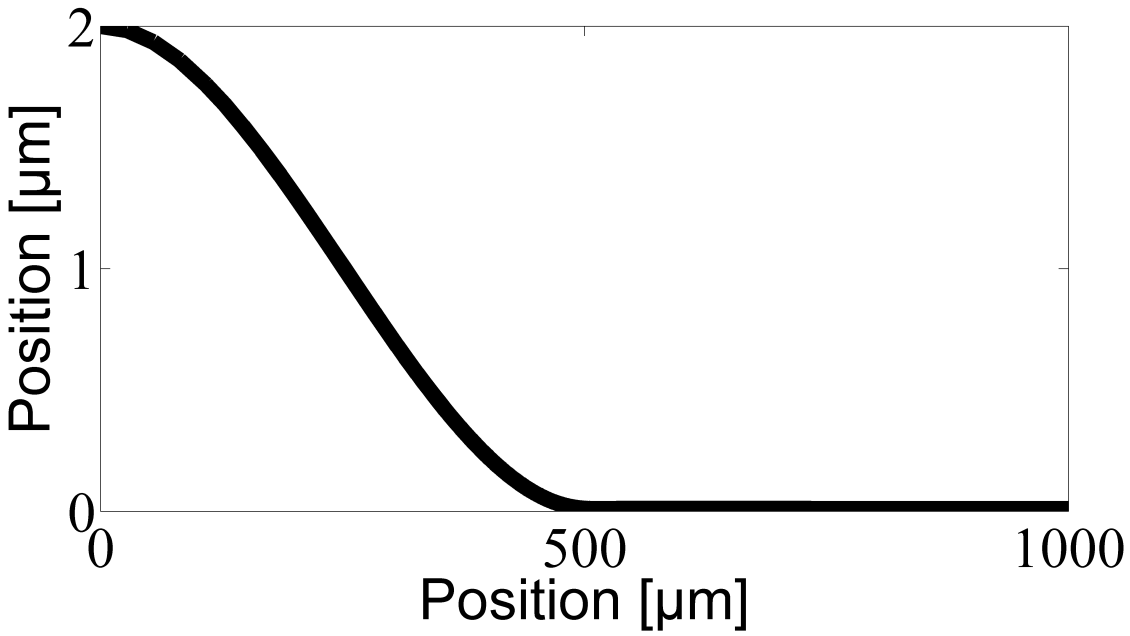

Figure 6.1. Initial deflection of the microcantilever used for stiction-release analysis. Microcantilever is in black with length of 1000 μm and anchored on the left at an undeflected gap of 2 μm. It has approximately 500 μm of length in close proximity (contact/near-contact) to the dielectric layer (imagined to coincide with the 0 μm mark on the vertical axis).

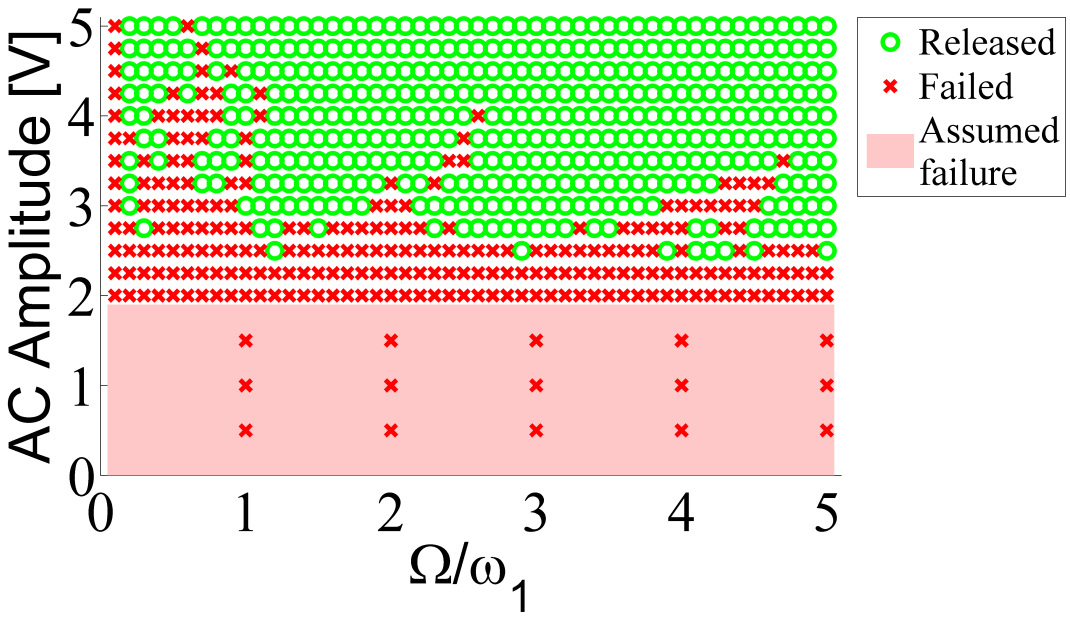

Figure 6.2. Preliminary simulation-based investigation into the dynamic electrostatic actuation release of the stiction-failed microcantilever presented in Figure 6.1, showing failed (microcantilever maintains contact with dielectric layer) and released (microcantilever releases from contact with the dielectric layer) regions. AC Amplitude refers to the magnitude of the sinusoidal voltage input, while the drive frequency Ω is divided by ω_1, the fundamental frequency for a clamped-clamped beam of length corresponding to the unstuck region of the microcantilever.

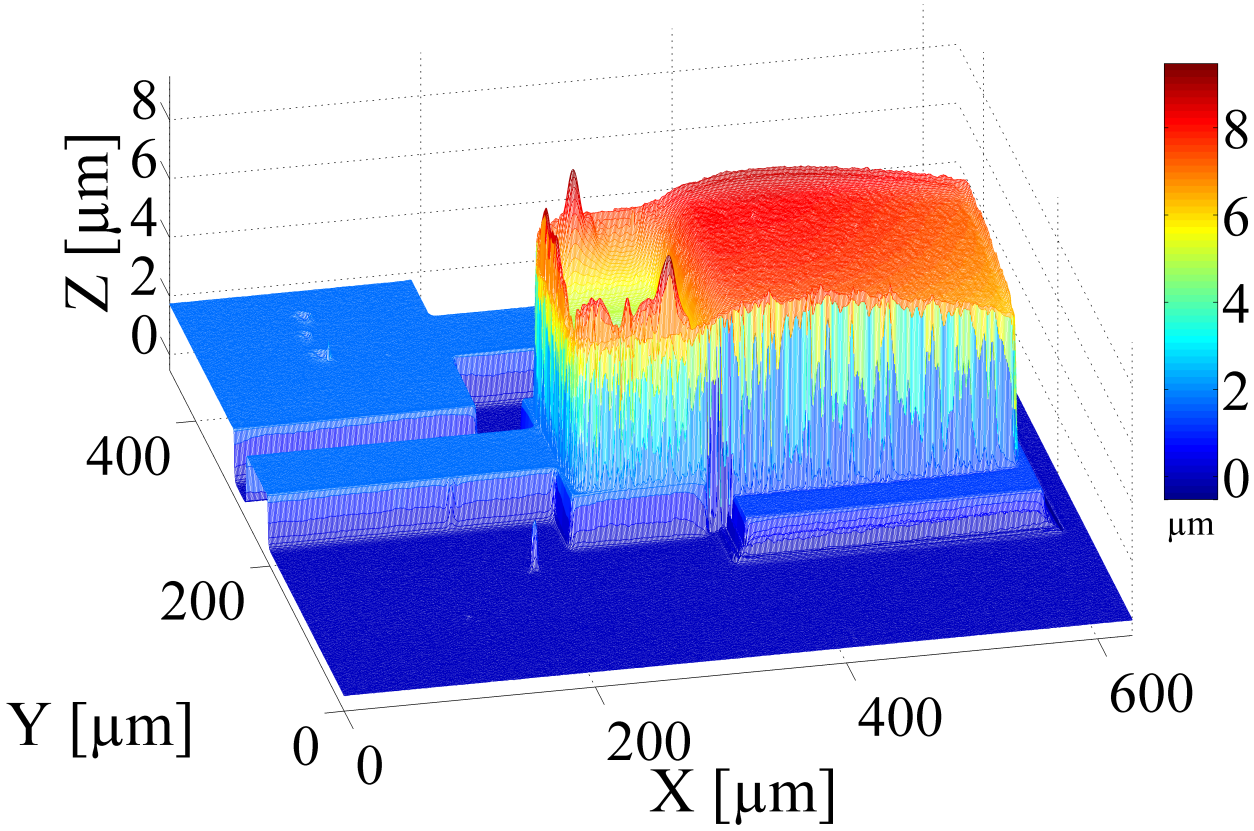

Figure 6.3. Example output from the Bruker ContourGT-K 3D optical microscope for a switch is failed in the ON state due to stiction between the microcantilever and the dielectric layer.

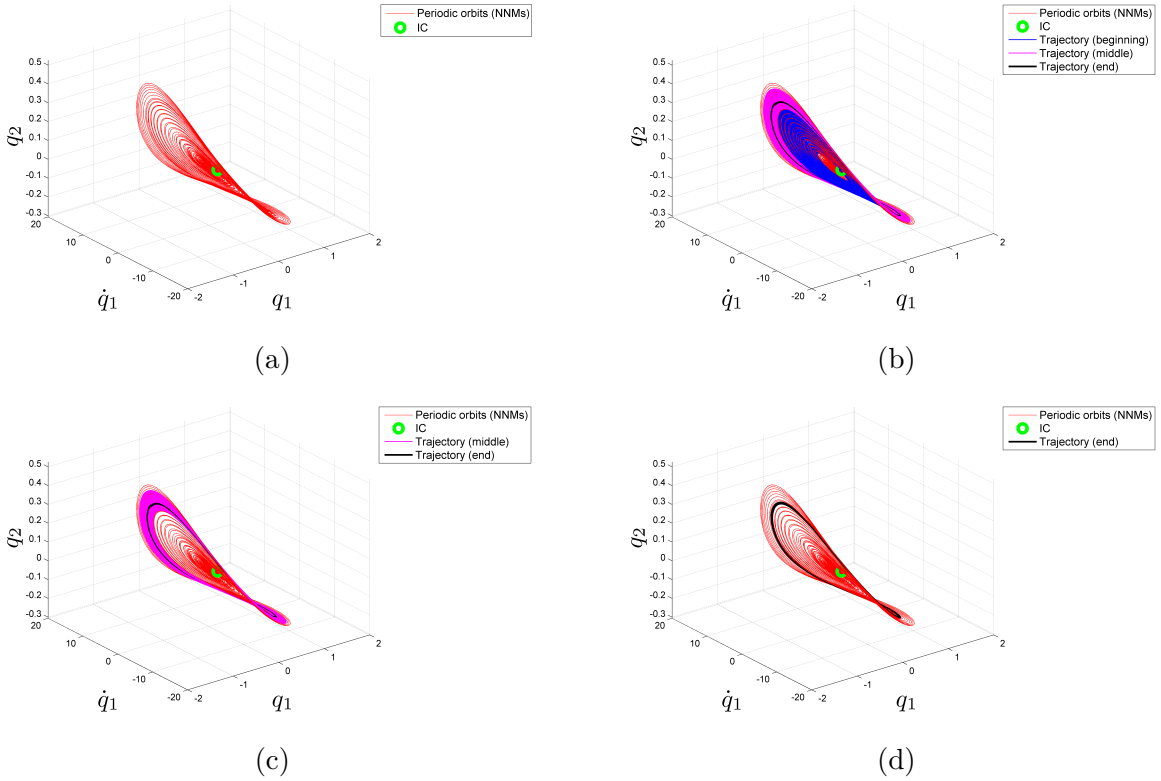

Figure 6.4. Phase space representation of the FPO and a simulated trajectory for state variables q_1, $\dot{q}_1$, and q_2. Trajectory for 500 drive periods is divided up into thirds (beginning, middle, and end) to indicate its path toward the final stable periodic orbit. Initial conditions correspond to a point on the FPO.

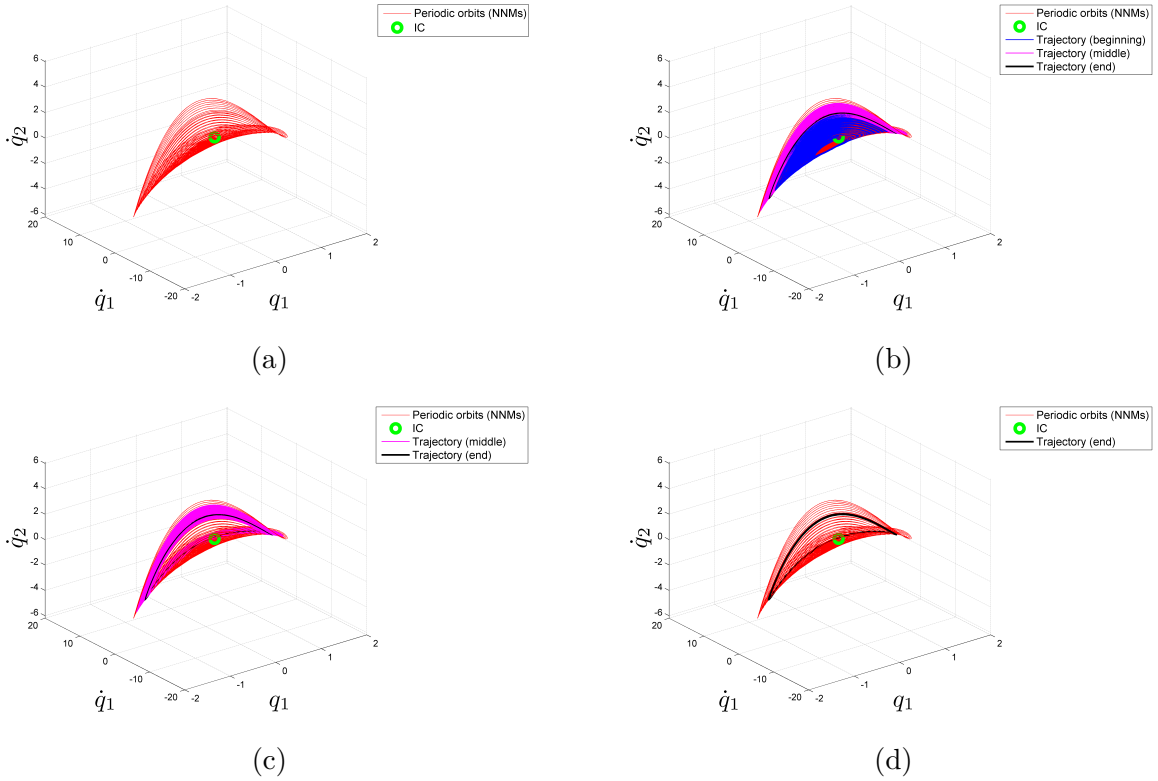

Figure 6.5. Phase space representation of the FPO and a simulated trajectory for state variables q_1, $\dot{q}_1$, and $\dot{q}_2$. Trajectory for 500 drive periods is divided up into thirds (beginning, middle, and end) to indicate its path toward the final stable periodic orbit. Initial conditions correspond to a point on the FPO.

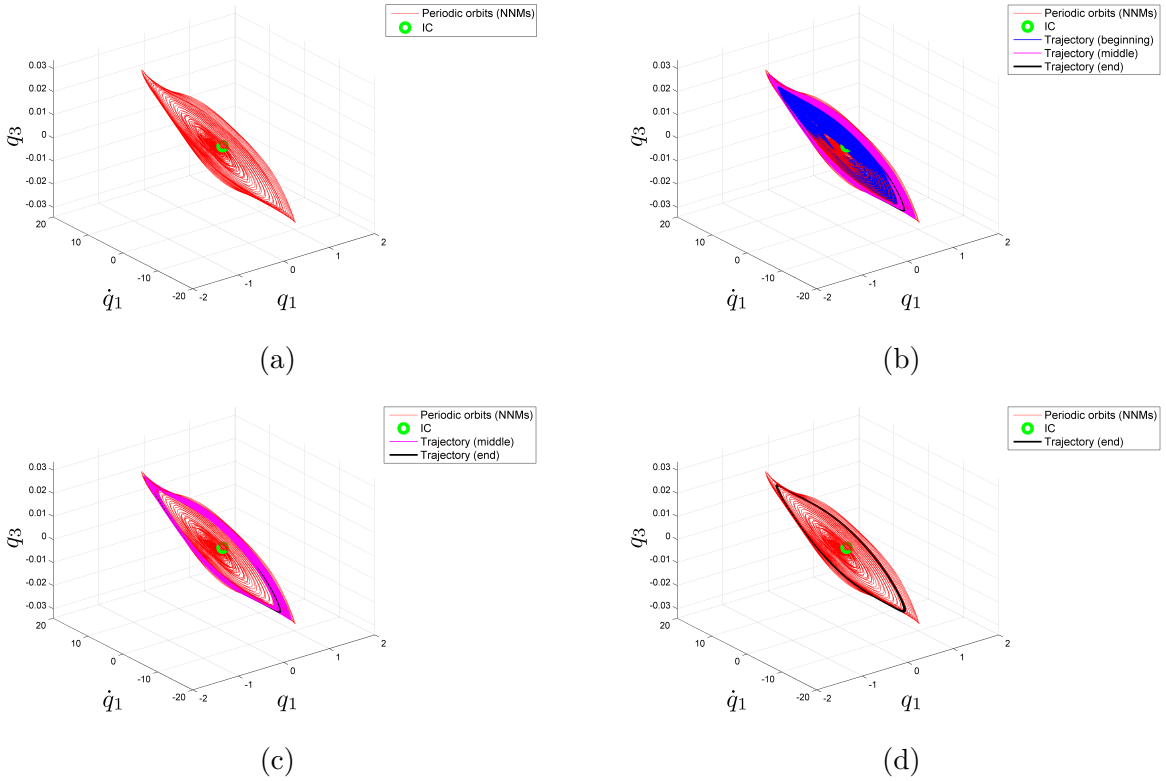

Figure 6.6. Phase space representation of the FPO and a simulated trajectory for state variables q_1, $\dot{q}_1$, and q_3. Trajectory for 500 drive periods is divided up into thirds (beginning, middle, and end) to indicate its path toward the final stable periodic orbit. Initial conditions correspond to a point on the FPO.

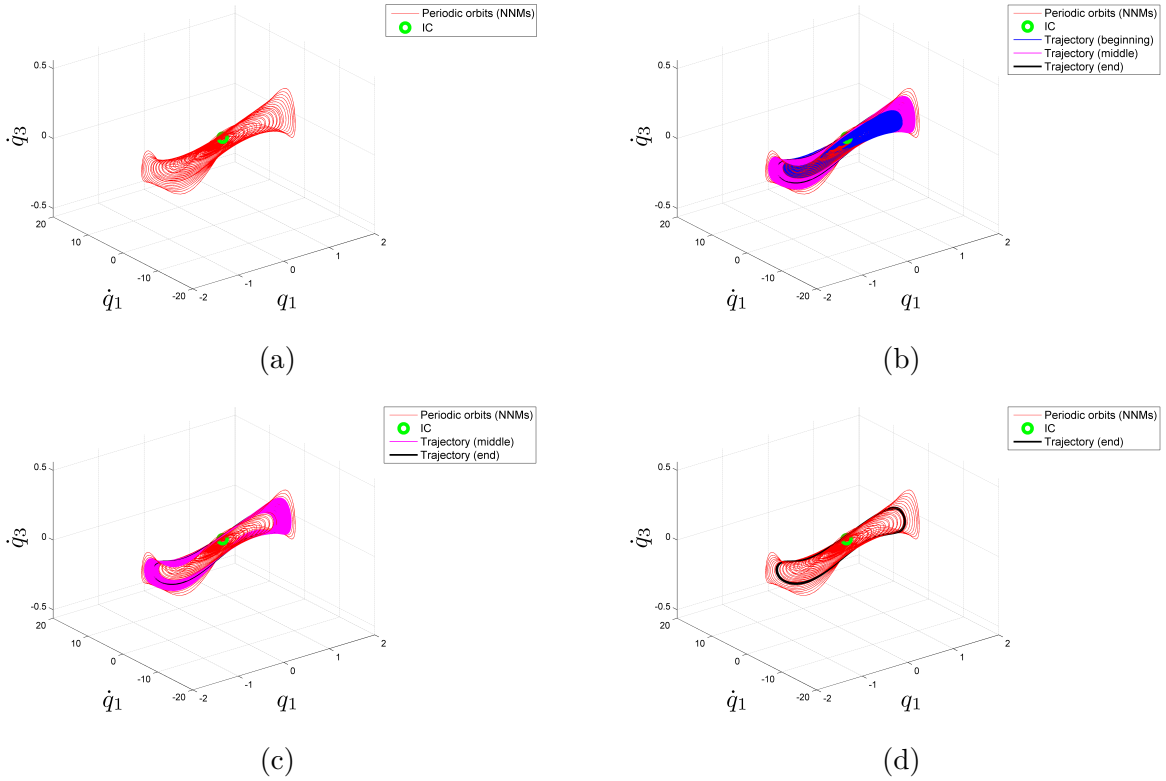

Figure 6.7. Phase space representation of the FPO and a simulated trajectory for state variables q_1, $\dot{q}_1$, and $\dot{q}_3$. Trajectory for 500 drive periods is divided up into thirds (beginning, middle, and end) to indicate its path toward the final stable periodic orbit. Initial conditions correspond to a point on the FPO.

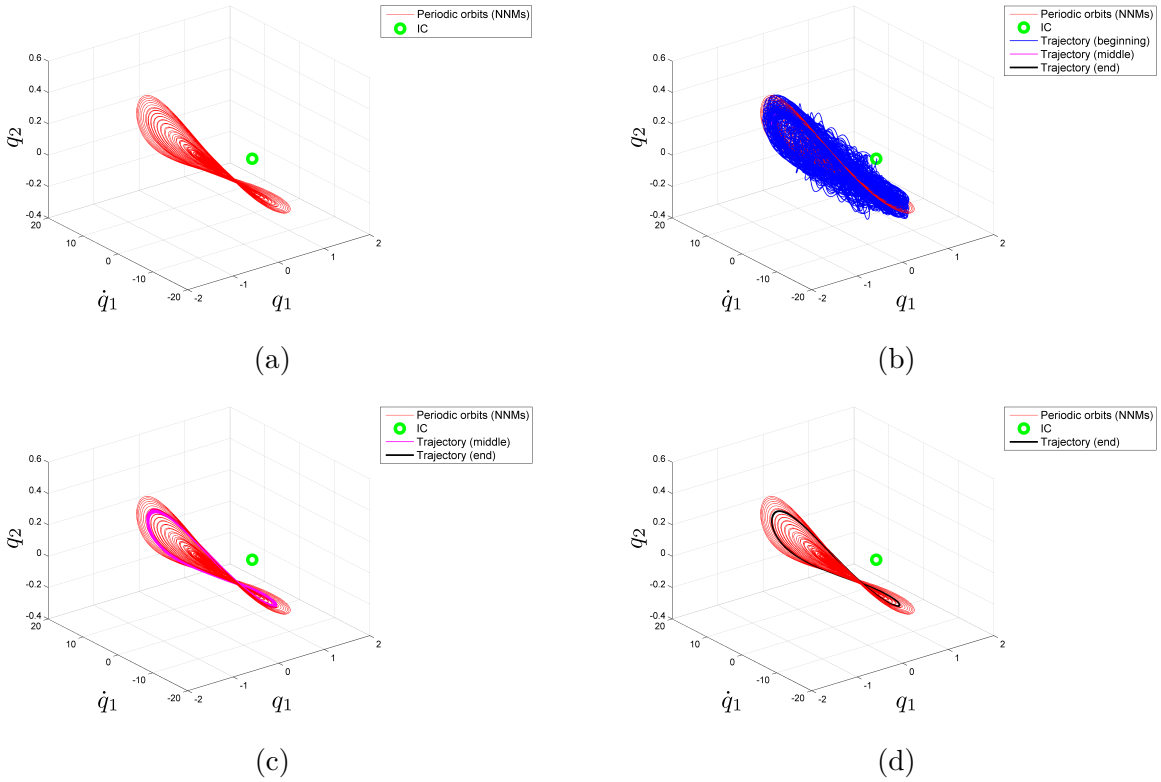

Figure 6.8. Phase space representation of the FPO and a simulated trajectory for state variables q_1, $\dot{q}_1$, and q_2. Trajectory for 500 drive periods is divided up into thirds (beginning, middle, and end) to indicate its path toward the final stable periodic orbit. Initial conditions correspond to a point away from the FPO.

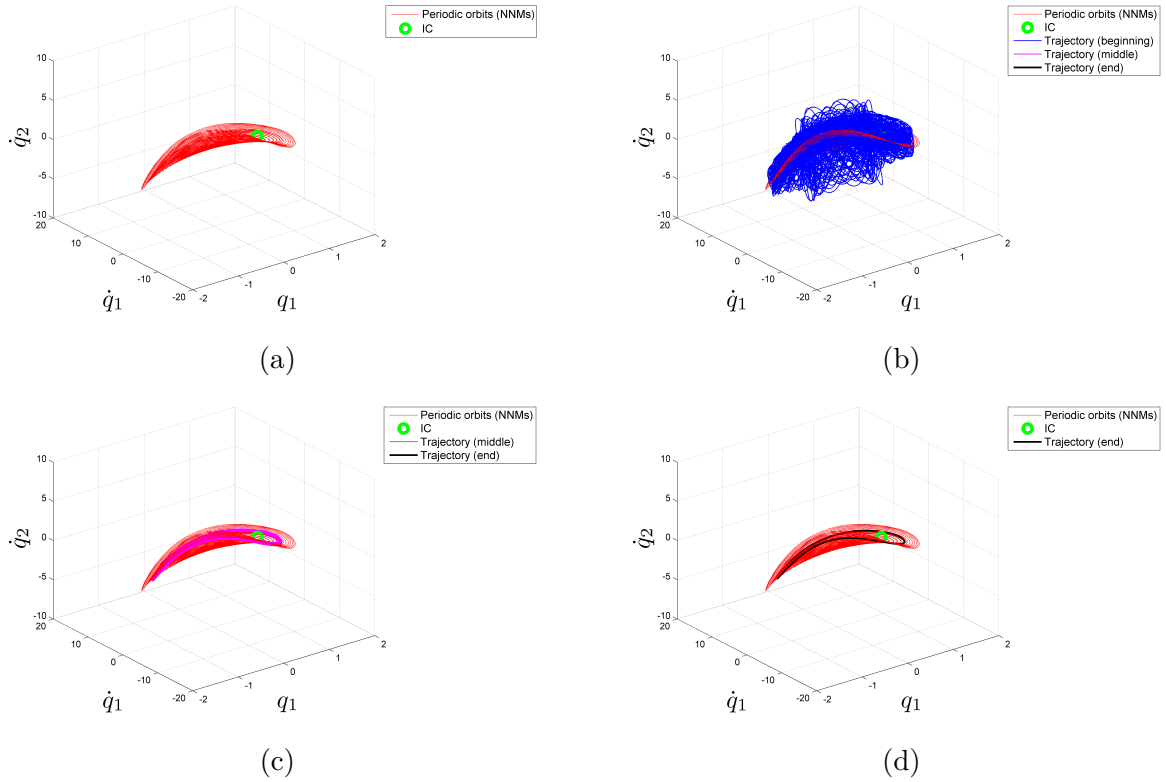

Figure 6.9. Phase space representation of the FPO and a simulated trajectory for state variables q_1, $\dot{q}_1$, and $\dot{q}_2$. Trajectory for 500 drive periods is divided up into thirds (beginning, middle, and end) to indicate its path toward the final stable periodic orbit. Initial conditions correspond to a point away from the FPO.

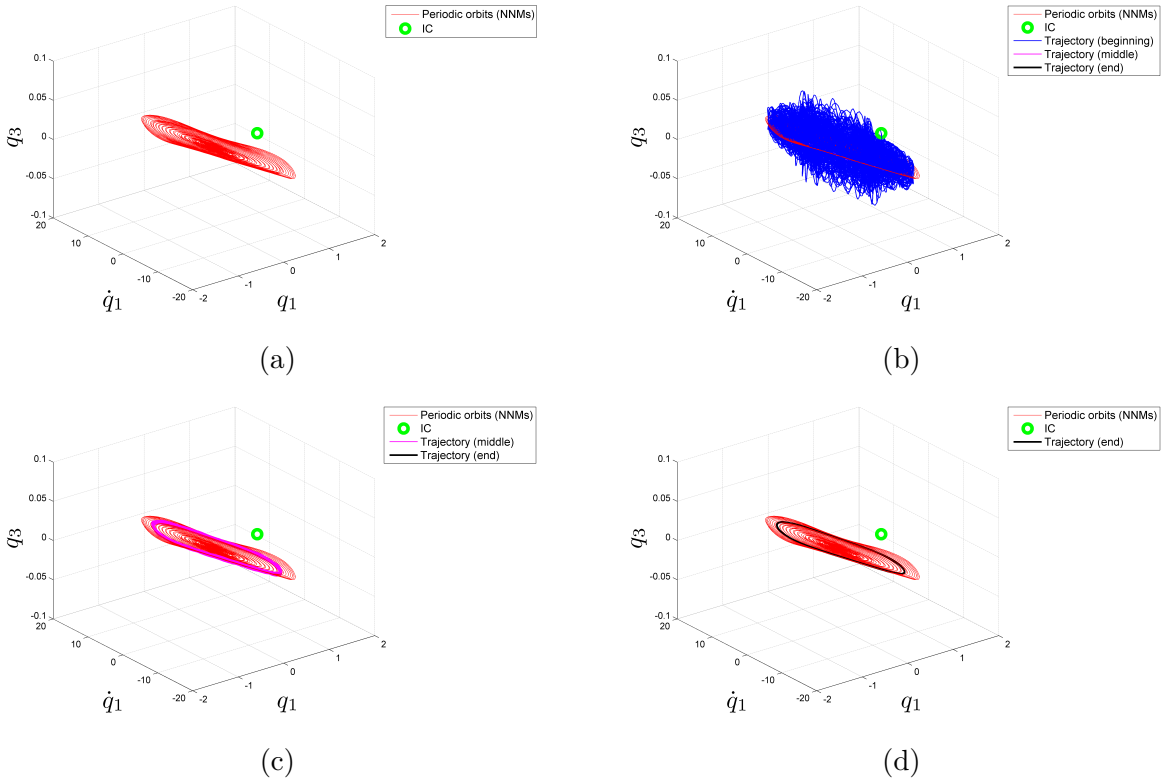

Figure 6.10. Phase space representation of the FPO and a simulated trajectory for state variables q_1, $\dot{q}_1$, and q_3. Trajectory for 500 drive periods is divided up into thirds (beginning, middle, and end) to indicate its path toward the final stable periodic orbit. Initial conditions correspond to a point away from the FPO.

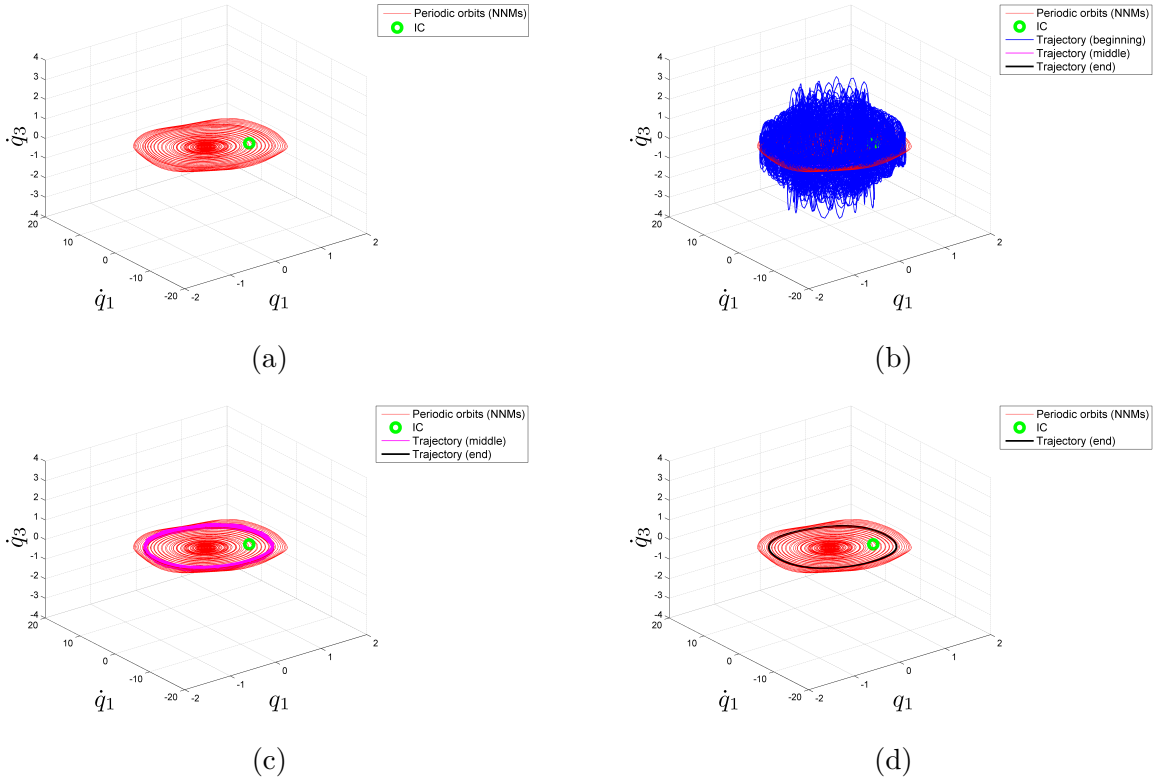

Figure 6.11. Phase space representation of the FPO and a simulated trajectory for state variables q_1, $\dot{q}_1$, and $\dot{q}_3$. Trajectory for 500 drive periods is divided up into thirds (beginning, middle, and end) to indicate its path toward the final stable periodic orbit. Initial conditions correspond to a point away from the FPO.

REFERENCES

[1] A. Boisen, S. Dohn, S. S. Keller, S. Schmid, and M. Tenje, "Cantilever-like micromechanical sensors," *Reports on Progress in Physics*, vol. 74, no. 3, p. 036 101, 2011, ISSN: 0034-4885. DOI: 10.1088/0034-4885/74/3/036101. [Online]. Available: http://stacks.iop.org/0034-4885/74/i=3/a=036101.

[2] M. I. Younis, F. M. Alsaleem, R. Miles, and Q. Su, "Characterization of the performance of capacitive switches activated by mechanical shock," *Journal of Micromechanics and Microengineering*, vol. 17, no. 7, p. 1360, Jul. 2007, ISSN: 0960-1317. DOI: 10.1088/0960-1317/17/7/019. [Online]. Available: http://iopscience.iop.org.ezproxy.lib.purdue.edu/0960-1317/17/7/019.

[3] J. S. Go, Y.-H. Cho, B. M. Kwak, and K. Park, "Snapping microswitches with adjustable acceleration threshold," *Sensors and Actuators A: Physical*, vol. 54, no. 1, pp. 579–583, Jun. 1996, ISSN: 0924-4247. DOI: 10.1016/S0924-4247(97)80018-0. [Online]. Available: http://www.sciencedirect.com/science/article/pii/S0924424797800180.

[4] M. T. A. Saif, "On a tunable bistable MEMS-theory and experiment," *Journal of Microelectromechanical Systems*, vol. 9, no. 2, pp. 157–170, Jun. 2000, ISSN: 1057-7157. DOI: 10.1109/84.846696.

[5] Gabriel M. Rebeiz, *RF MEMS: Theory, Design, and Technology*. Hoboken, NJ: John Wiley, 2003, ISBN: 0-471-20169-3.

[6] G. M. Rebeiz and J. B. Muldavin, "RF MEMS switches and switch circuits," *IEEE Microwave Magazine*, vol. 2, no. 4, pp. 59–71, Dec. 2001, ISSN: 1527-3342. DOI: 10.1109/6668.969936.

[7] C. T. C. Nguyen, L. P. B. Katehi, and G. M. Rebeiz, "Micromachined devices for wireless communications," *Proceedings of the IEEE*, vol. 86, no. 8, pp. 1756–1768, Aug. 1998, ISSN: 0018-9219. DOI: 10.1109/5.704281.

[8] H. A. C. Tilmans, W. D. Raedt, and E. Beyne, "MEMS for wireless communications: 'from RF-MEMS components to RF-MEMS-SiP'," *Journal of Micromechanics and Microengineering*, vol. 13, no. 4, S139, 2003, ISSN: 0960-1317. DOI: 10.1088/0960-1317/13/4/323. [Online]. Available: http://stacks.iop.org/0960-1317/13/i=4/a=323.

[9] J. F. Rhoads, S. W. Shaw, and K. L. Turner, "Nonlinear dynamics and its applications in micro- and nanoresonators," *Journal of Dynamic Systems, Measurement, and Control*, vol. 132, no. 3, p. 034 001, 2010, ISSN: 00220434. DOI: 10.1115/1.4001333. [Online]. Available: http://DynamicSystems.asmedigitalcollection.asme.org/article.aspx?articleid=1414388.

[10] B. Halg, "On a micro-electro-mechanical nonvolatile memory cell," *IEEE Transactions on Electron Devices*, vol. 37, no. 10, pp. 2230–2236, Oct. 1990, ISSN: 0018-9383. DOI: 10.1109/16.59913.

[11] M. I. Younis and F. Alsaleem, "Exploration of new concepts for mass detection in electrostatically-actuated structures based on nonlinear phenomena," *Journal of Computational and Nonlinear Dynamics*, vol. 4, no. 021010, Mar. 2009, ISSN: 1555-1415. DOI: 10.1115/1.3079785. [Online]. Available: https://doi.org/10.1115/1.3079785.

[12] M. H. Hasan, F. M. Alsaleem, and H. M. Ouakad, "Novel threshold pressure sensors based on nonlinear dynamics of MEMS resonators," *Journal of Micromechanics and Microengineering*, vol. 28, no. 6, p. 065 007, 2018, ISSN: 0960-1317. DOI: 10.1088/1361-6439/aab515. [Online]. Available: http://stacks.iop.org/0960-1317/28/i=6/a=065007.

[13] A. Fruehling, R. Tung, A. Raman, and D. Peroulis, "In situ monitoring of dynamic bounce phenomena in RF MEMS switches," *Journal of Micromechanics and Microengineering*, vol. 23, no. 11, p. 115 007, Nov. 2013, ISSN: 0960-1317, 1361-6439. DOI: 10.1088/0960-1317/23/11/115007. [Online]. Available: http://stacks.iop.org/0960-1317/23/i=11/a=115007?key=crossref.b4bc157eecbe26211ec138e94c542c78.

[14] S. S. Rao, *Mechanical Vibrations*, 5th ed.. Upper Saddle River, NJ: Prentice Hall, 2011, ISBN: 0-13-212819-5.

[15] S. Gorthi, A. Mohanty, and A. Chatterjee, "Cantilever beam electrostatic MEMS actuators beyond pull-in," *Journal of Micromechanics and Microengineering*, vol. 16, no. 9, pp. 1800–1810, Sep. 2006, ISSN: 0960-1317, 1361-6439. DOI: 10.1088/0960-1317/16/9/007. [Online]. Available: http://stacks.iop.org/0960-1317/16/i=9/a=007?key=crossref.6d58e4e5908b5c94d0ce75705c15db9c.

[16] R. Batra, M. Porfiri, and D. Spinello, "Electromechanical model of electrically actuated narrow microbeams," *Journal of Microelectromechanical Systems*, vol. 15, no. 5, pp. 1175–1189, Oct. 2006, ISSN: 1057-7157. DOI: 10.1109/JMEMS.2006.880204.

[17] J. N. Israelachvili, *Intermolecular and Surface Forces*, 3rd, J. N. Israelachvili, Ed. San Diego: Academic Press, 2011, ISBN: 978-0-12-375182-9. [Online]. Available: http://www.sciencedirect.com/science/article/pii/B9780123751829100132.

[18] F. W. DelRio, M. P. de Boer, J. A. Knapp, E. David Reedy, P. J. Clews, and M. L. Dunn, "The role of van der Waals forces in adhesion of micromachined surfaces," *Nature Materials*, vol. 4, no. 8, pp. 629–634, Aug. 2005, ISSN: 1476-1122. DOI: 10.1038/nmat1431. [Online]. Available: http://www.nature.com.ezproxy.lib.purdue.edu/nmat/journal/v4/n8/full/nmat1431.html.

[19] M. Abtahi, G. Vossoughi, and A. Meghdari, "Effects of the van der Waals force, squeeze-film damping, and contact bounce on the dynamics of electrostatic microcantilevers before and after pull-in," *Nonlinear Dynamics*, Feb. 2014, ISSN: 0924-090X, 1573-269X. DOI: 10.1007/s11071-014-1275-7. [Online]. Available: http://link.springer.com/10.1007/s11071-014-1275-7.

[20] Y.-P. Zhao, L. S. Wang, and T. X. Yu, "Mechanics of adhesion in MEMS—a review," *Journal of Adhesion Science and Technology*, vol. 17, no. 4, pp. 519–546, Jan. 2003, ISSN: 0169-4243. DOI: 10.1163/15685610360554393. [Online]. Available: http://dx.doi.org/10.1163/15685610360554393.

[21] H. M. Ouakad and M. I. Younis, "Modeling and simulations of collapse instabilities of microbeams due to capillary forces," *Mathematical Problems in Engineering*, vol. 2009, Article ID 871902, 16 p. 2009, ISSN: 1024-123X. DOI: 10.1155/2009/871902.

[22] Y. Huang, A. S. S. Vasan, R. Doraiswami, M. Osterman, and M. Pecht, "MEMS reliability review," *IEEE Transactions on Device and Materials Reliability*, vol. 12, no. 2, pp. 482–493, Jun. 2012, ISSN: 1530-4388. DOI: 10.1109/TDMR.2012.2191291.

[23] J. Knapp and M. de Boer, "Mechanics of microcantilever beams subject to combined electrostatic and adhesive forces," *Journal of Microelectromechanical Systems*, vol. 11, no. 6, pp. 754–764, Dec. 2002, ISSN: 1057-7157. DOI: 10.1109/JMEMS.2002.805047. [Online]. Available: http://ieeexplore.ieee.org/lpdocs/epic03/wrapper.htm?arnumber=1097796.

[24] H. Hsu, M. Koslowski, and D. Peroulis, "An experimental and theoretical investigation of creep in ultrafine crystalline nickel RF-MEMS devices," *IEEE Transactions on Microwave Theory and Techniques*, vol. 59, no. 10, pp. 2655–2664, Oct. 2011, Conference Name: IEEE Transactions on Microwave Theory and Techniques, ISSN: 1557-9670. DOI: 10.1109/TMTT.2011.2163727.

[25] S. Das, M. Koslowski, S. R. Mathur, and J. Y. Murthy, "Finite volume method for simulation of creep in RF MEMS Devices," American Society of Mechanical Engineers Digital Collection, Aug. 2012, pp. 119–128. DOI: 10.1115/IMECE2011-62660. [Online]. Available: https://proceedings.asmedigitalcollection.asme.org/IMECE/proceedings/IMECE2011/54976/119/358745.

[26] J. Rogers, T. Mackin, and L. Phinney, "A thermomechanical model for adhesion reduction of MEMS cantilevers," *Journal of Microelectromechanical Systems*, vol. 11, no. 5, pp. 512–520, Oct. 2002, ISSN: 1057-7157. DOI: 10.1109/JMEMS.2002.803412. [Online]. Available: http://ieeexplore.ieee.org/lpdocs/epic03/wrapper.htm?arnumber=1038846.

[27] A. Savkar, K. Murphy, Z. Leseman, T. Mackin, and M. R. Begley, "On the use of structural vibrations to release stiction failed MEMS," *Journal of Microelectromechanical Systems*, vol. 16, no. 1, pp. 163–173, Feb. 2007, ISSN: 1057-7157. DOI: 10.1109/JMEMS.2006.885986.

[28] K. Asadi, J. Li, S. Peshin, J. Yeom, and H. Cho, "Mechanism of geometric nonlinearity in a nonprismatic and heterogeneous microbeam resonator," *Physical Review B*, vol. 96, no. 11, p. 115 306, Sep. 2017, Publisher: American Physical Society. DOI: 10.1103/PhysRevB.96.115306. [Online]. Available: https://link.aps.org/doi/10.1103/PhysRevB.96.115306.

[29] R. C. Tung, A. Garg, A. Kovacs, D. Peroulis, and A. Raman, "Estimating residual stress, curvature and boundary compliance of doubly clamped MEMS from their vibration response," *Journal of Micromechanics and Microengineering*, vol. 23, no. 4, p. 045 009, 2013, ISSN: 0960-1317. DOI: 10.1088/0960-1317/23/4/045009. [Online]. Available: http://stacks.iop.org/0960-1317/23/i=4/a=045009.

[30] Z. J. Guo, N. E. McGruer, and G. G. Adams, "Modeling, simulation and measurement of the dynamic performance of an ohmic contact, electrostatically actuated RF MEMS switch," *Journal of Micromechanics and Microengineering*, vol. 17, no. 9, p. 1899, 2007, ISSN: 0960-1317. DOI: 10.1088/0960-1317/17/9/019. [Online]. Available: http://stacks.iop.org/0960-1317/17/i=9/a=019.

[31] S. W. Lee, S. J. Park, E. E. B. Campbell, and Y. W. Park, "A fast and low-power microelectromechanical system-based non-volatile memory device," *Nature Communications*, vol. 2, p. 220, Mar. 2011. DOI: 10.1038/ncomms1227. [Online]. Available: https://www.nature.com/articles/ncomms1227.

[32] *COMSOL Multiphysics®*, Stockholm, Sweden, 2020. [Online]. Available: www.comsol.com.

[33] E. J. Doedel and B. E. Oldeman, *AUTO-07p: Continuation and Bifurcation Software*, 2012. [Online]. Available: http://indy.cs.concordia.ca/auto/.

[34] W.-J. Beyn, A. Champneys, E. Doedel, W. Govaerts, Y. A. Kuznetsov, and B. Sandstede, "Numerical continuation, and computation of normal forms," in *Handbook of Dynamical Systems*, ser. Handbook of Dynamical Systems, B. Fiedler, Ed., vol. 2, Elsevier Science, Jan. 2002, pp. 149–219. DOI: 10.1016/S1874-575X(02)80025-X. [Online]. Available: http://www.sciencedirect.com/science/article/pii/S1874575X0280025X.

[35] H. B. Keller, "Numerical solution of bifurcation and nonlinear eigenvalue problems," in *Applications of Bifurcation Theory, P. Rabinowitz, ed.* New York: Academic Press, 1977, pp. 359–384.

[36] S. Krylov, B. R. Ilic, D. Schreiber, S. Seretensky, and H. Craighead, "The pull-in behavior of electrostatically actuated bistable microstructures," *Journal of Micromechanics and Microengineering*, vol. 18, no. 5, p. 055 026, May 2008, ISSN: 0960-1317. DOI: 10.1088/0960-1317/18/5/055026. [Online]. Available: http://iopscience.iop.org/0960-1317/18/5/055026.

[37] A. H. Nayfeh and D. T. Mook, *Nonlinear Oscillations*. John Wiley & Sons, Ltd, 1995, ISBN: 978-3-527-61758-6. [Online]. Available: https://onlinelibrary.wiley.com/doi/abs/10.1002/9783527617586.fmatter.

[38] D. Kalafut, A. Bajaj, and A. Raman, "Multistability of cantilever MEMS/NEMS switches induced by electrostatic and surface forces," *International Journal of Non-Linear Mechanics*, vol. 95, pp. 209–215, Oct. 2017, ISSN: 00207462. DOI: 10.1016/j.ijnonlinmec.2017.06.009. [Online]. Available: http://linkinghub.elsevier.com/retrieve/pii/S0020746216304309.

[39] *Postbuckling Analysis of a Hinged Cylindrical Shell*. [Online]. Available: https://www.comsol.com/model/postbuckling-analysis-of-a-hinged-cylindrical-shell-10257.

[40] J. Stulemeijer, J. Bielen, P. Steeneken, and J. van den Berg, "Numerical path following as an analysis method for electrostatic MEMS," *Journal of Microelectromechanical Systems*, vol. 18, no. 2, pp. 488–499, Apr. 2009, ISSN: 1057-7157. DOI: 10.1109/JMEMS.2008.2011111.

[41] D. Kalafut, A. Bajaj, and A. Raman, "Tristable capacitive microcantilever switches: Measurements and simulations," *International Journal of Non-Linear Mechanics*, vol. 119, p. 103 304, Mar. 2020, ISSN: 0020-7462. DOI: 10.1016/j.ijnonlinmec.2019.103304. [Online]. Available: http://www.sciencedirect.com/science/article/pii/S0020746219302124.

[42] M. G. Snow and A. K. Bajaj, "Comprehensive reduced-order models of electrostatically actuated MEMS switches and their dynamics including impact and bounce," in *4th International Conference on Micro- and Nanosystems*, vol. 4, Montreal, Quebec, Canada: ASME, Jan. 2010, pp. 579–588. DOI: 10.1115/DETC2010-28590. [Online]. Available: http://dx.doi.org/10.1115/DETC2010-28590.

[43] A. E. Lindsay, J. Lega, and K. B. Glasner, "Regularized model of post-touchdown configurations in electrostatic MEMS: Equilibrium analysis," *Physica D: Nonlinear Phenomena*, vol. 280–281, pp. 95–108, Jul. 2014, ISSN: 0167-2789. DOI: 10.1016/j.physd.2014.04.007. [Online]. Available: http://www.sciencedirect.com/science/article/pii/S0167278914000864.

[44] S. Krylov, "Lyapunov exponents as a criterion for the dynamic pull-in instability of electrostatically actuated microstructures," *International Journal of Non-Linear Mechanics*, vol. 42, no. 4, pp. 626–642, May 2007, ISSN: 00207462. DOI: 10.1016/j.ijnonlinmec.2007.01.004. [Online]. Available: http://linkinghub.elsevier.com/retrieve/pii/S0020746207000376.

[45] M. Dequesnes, S. V. Rotkin, and N. R. Aluru, "Calculation of pull-in voltages for carbon-nanotube-based nanoelectromechanical switches," *Nanotechnology*, vol. 13, no. 1, p. 120, Feb. 2002, ISSN: 0957-4484. DOI: 10.1088/0957-4484/13/1/325. [Online]. Available: http://iopscience.iop.org/0957-4484/13/1/325.

[46] O. Loh, X. Wei, C. Ke, J. Sullivan, and H. D. Espinosa, "Robust carbon-nanotube-based nano-electromechanical devices: Understanding and eliminating prevalent failure modes using alternative electrode materials," *Small*, vol. 7, no. 1, pp. 79–86, 2011, ISSN: 1613-6829. DOI: 10.1002/smll.201001166. [Online]. Available: http://onlinelibrary.wiley.com/doi/10.1002/smll.201001166/abstract.

[47] K. Ono, "Numerical analysis of contact mechanics between a spherical slider and a flat disk with low roughness considering Lennard-Jones surface forces," *Journal of Adhesion Science & Technology*, vol. 24, no. 15/16, pp. 2341–2362, Oct. 2010, ISSN: 01694243. DOI: 10.1163/016942410X508316. [Online]. Available: http://search.ebscohost.com/login.aspx?direct=true&db=aph&AN=54554873&site=ehost-live.

[48] H. Kim, N. H. Shaik, X. Xu, A. Raman, and A. Strachan, "Multiscale contact mechanics model for RF–MEMS switches with quantified uncertainties," *Modelling and Simulation in Materials Science and Engineering*, vol. 21, no. 8, p. 085 002, Dec. 2013, ISSN: 0965-0393, 1361-651X. DOI: 10.1088/0965-0393/21/8/085002. [Online]. Available: http://stacks.iop.org/0965-0393/21/i=8/a=085002?key=crossref.051249075f35dded88ecb0d2265b1646.

[49] G. S. Fishman, *Monte Carlo: Concepts, Algorithms, and Applications*. New York, NY: Springer New York, 1996, ISBN: 978-1-4419-2847-4 978-1-4757-2553-7. [Online]. Available: http://link.springer.com/10.1007/978-1-4757-2553-7.

[50] N. P. van der Meijs and J. T. Fokkema, "VLSI circuit reconstruction from mask topology," *Integration, the VLSI Journal*, vol. 2, no. 2, pp. 85–119, Jun. 1984, ISSN: 0167-9260. DOI: 10.1016/0167-9260(84)90016-6. [Online]. Available: http://www.sciencedirect.com/science/article/pii/0167926084900166.

[51] M. G. Snow, "Comprehensive modeling of electrostatically actuated MEMS beams including uncertainty quantification," M.S.M.E. Thesis, Purdue University, United States – Indiana, 2010. [Online]. Available: http://search.proquest.com/docview/856128644/abstract/8E068DB4A7924228PQ/1?accountid=13360.

[52] K. Mittal, Ed., *Adhesion Aspects in MEMS/NEMS*. CRC Press, Feb. 2011, ISBN: 978-90-04-19094-8 978-90-04-19095-5. [Online]. Available: http://www.crcnetbase.com/doi/book/10.1201/b12181.

[53] P. Attard and J. L. Parker, "Deformation and adhesion of elastic bodies in contact," *Physical Review A*, vol. 46, no. 12, pp. 7959–7971, Dec. 1992. DOI: 10.1103/PhysRevA.46.7959. [Online]. Available: http://link.aps.org/doi/10.1103/PhysRevA.46.7959.

[54] N. Yu and A. A. Polycarpou, "Adhesive contact based on the Lennard-Jones potential: A correction to the value of the equilibrium distance as used in the potential," *Journal of Colloid and Interface Science*, vol. 278, no. 2, pp. 428–435, Oct. 2004, ISSN: 0021-9797. DOI: 10.1016/j.jcis.2004.06.029. [Online]. Available: http://www.sciencedirect.com/science/article/pii/S0021979704005454.

[55] W. M. van Spengen, "A physical model to describe the distribution of adhesion strength in MEMS, or why one MEMS device sticks and another 'identical' one does not," *Journal of Micromechanics and Microengineering*, vol. 25, no. 12, p. 125 012, Dec. 2015, ISSN: 0960-1317, 1361-6439. DOI: 10.1088/0960-1317/25/12/125012. [Online]. Available: http://stacks.iop.org/0960-1317/25/i=12/a=125012?key=crossref.505ce6224a2efc5ca2b291008ed1af63.

[56] W. M. van Spengen, "MEMS reliability from a failure mechanisms perspective," *Microelectronics Reliability*, vol. 43, no. 7, pp. 1049–1060, Jul. 2003, ISSN: 0026-2714. DOI: 10.1016/S0026-2714(03)00119-7. [Online]. Available: http://www.sciencedirect.com/science/article/pii/S0026271403001197.

[57] M. P. de Boer and T. A. Michalske, "Accurate method for determining adhesion of cantilever beams," *Journal of Applied Physics*, vol. 86, no. 2, pp. 817–827, Jul. 1999, ISSN: 0021-8979, 1089-7550. DOI: 10.1063/1.370809. [Online]. Available: http://scitation.aip.org/content/aip/journal/jap/86/2/10.1063/1.370809.

[58] C. de Boor and B. Swartz, "Collocation at Gaussian points," *SIAM Journal on Numerical Analysis*, vol. 10, no. 4, pp. 582–606, Sep. 1973, ISSN: 0036-1429. DOI: 10.1137/0710052. [Online]. Available: http://epubs.siam.org/doi/abs/10.1137/0710052.

[59] J. M. Souza, "Boundary conditions in the finite-difference method," *Mecánica Computacional*, vol. 1, no. 1, pp. 23–33, 1985. [Online]. Available: http://www.cimec.org.ar/ojs/index.php/mc/issue/view/462.

[60] R. LeVeque, *Finite Difference Methods for Ordinary and Partial Differential Equations*, ser. Other Titles in Applied Mathematics. Society for Industrial and Applied Mathematics, 2007, ISBN: 978-0-89871-629-0. [Online]. Available: http://epubs.siam.org/doi/book/10.1137/1.9780898717839.

[61] *PRISM - Discovery Park at Purdue*. [Online]. Available: http://www.purdue.edu/discoverypark/prism/.

[62] J. Zhao, R. Gao, Y. Yang, Y. Huang, and P. Hu, "A bidirectional acceleration switch incorporating magnetic-fields-based tristable mechanism," *IEEE/ASME Transactions on Mechatronics*, vol. 18, no. 1, pp. 113–120, Feb. 2013, ISSN: 1083-4435. DOI: 10.1109/TMECH.2011.2163725.

[63] B. Wu, M. Okoniewski, and M. E. Potter, "Design and fabrication of a ternary switch for MEMS-controlled reflectarray elements," *IEEE Antennas and Wireless Propagation Letters*, vol. 8, pp. 998–1001, 2009, ISSN: 1536-1225. DOI: 10.1109/LAWP.2009.2030770.

[64] G. Chen, Y. Gou, and A. Zhang, "Synthesis of compliant multistable mechanisms through use of a single bistable mechanism," *Journal of Mechanical Design*, vol. 133, no. 8, pp. 081007–081007–9, Aug. 2011, ISSN: 1050-0472. DOI: 10.1115/1.4004543. [Online]. Available: http://dx.doi.org/10.1115/1.4004543.

[65] H.-T. Pham and D.-A. Wang, "A quadristable compliant mechanism with a bistable structure embedded in a surrounding beam structure," *Sensors and Actuators A: Physical*, Solid-State Sensors, Actuators and Microsystems Workshop, vol. 167, no. 2, pp. 438–448, Jun. 2011, ISSN: 0924-4247. DOI: 10.1016/j.sna.2011.02.044. [Online]. Available: http://www.sciencedirect.com/science/article/pii/S0924424711001178.

[66] D.-A. Wang, J.-H. Chen, and H.-T. Pham, "A tristable compliant micromechanism with two serially connected bistable mechanisms," *Mechanism and Machine Theory*, vol. 71, pp. 27–39, Jan. 2014, ISSN: 0094-114X. DOI: 10.1016/j.mechmachtheory.2013.08.018. [Online]. Available: http://www.sciencedirect.com/science/article/pii/S0094114X13001766.

[67] J. Oberhammer, M. Tang, A.-Q. Liu, and G. Stemme, "Mechanically tri-stable, true single-pole-double-throw (SPDT) switches," *Journal of Micromechanics and Microengineering*, vol. 16, no. 11, pp. 2251–2258, 2006, ISSN: 0960-1317. DOI: 10.1088/0960-1317/16/11/001. [Online]. Available: http://stacks.iop.org/0960-1317/16/i=11/a=001.

[68] C. Wu, F. Li, and T. Guo, "Efficient tristable resistive memory based on single layer graphene/insulating polymer multi-stacking layer," *Applied Physics Letters*, vol. 104, no. 18, p. 183 105, May 2014, ISSN: 0003-6951. DOI: 10.1063/1.4875596. [Online]. Available: https://aip.scitation.org/doi/full/10.1063/1.4875596.

[69] P.-Y. Gu, F. Zhou, J. Gao, G. Li, C. Wang, Q.-F. Xu, Q. Zhang, and J.-M. Lu, "Synthesis, characterization, and nonvolatile ternary memory behavior of a larger heteroacene with nine linearly fused rings and two different heteroatoms," *Journal of the American Chemical Society*, vol. 135, no. 38, pp. 14 086–14 089, Sep. 2013, ISSN: 0002-7863. DOI: 10.1021/ja408208c. [Online]. Available: https://doi.org/10.1021/ja408208c.

[70] L. Li and D. Wen, "Memristic characteristics from bistable to tristable memory with controllable charge trap carbon nanotubes," *Nanomaterials*, vol. 8, no. 2, p. 114, Feb. 2018. DOI: 10.3390/nano8020114. [Online]. Available: http://www.mdpi.com/2079-4991/8/2/114.

[71] C. P. Vyasarayani, E. M. Abdel-Rahman, and J. McPhee, "Modeling of contact and stiction in electrostatic microcantilever actuators," *Journal of Nanotechnology in Engineering and Medicine*, vol. 3, no. 1, pp. 011003–011003–8, Aug. 2012, ISSN: 1949-2944. DOI: 10.1115/1.4006618. [Online]. Available: http://dx.doi.org/10.1115/1.4006618.

[72] T. J. W. Wagner and D. Vella, "Switch on, switch off: Stiction in nanoelectromechanical switches," *Nanotechnology*, vol. 24, no. 27, p. 275 501, Jun. 2013, ISSN: 0957-4484. DOI: 10.1088/0957-4484/24/27/275501. [Online]. Available: https://doi.org/10.1088%2F0957-4484%2F24%2F27%2F275501.

[73] E. K. Chan, K. Garikipati, and R. W. Dutton, "Characterization of contact electromechanics through capacitance-voltage measurements and simulations," *Journal of Microelectromechanical Systems*, vol. 8, no. 2, pp. 208–217, Jun. 1999, ISSN: 1057-7157. DOI: 10.1109/84.767117.

[74] S. H. Pu, A. S. Holmes, E. M. Yeatman, C. Papavassiliou, and S. Lucyszyn, "Stable zipping RF MEMS varactors," *Journal of Micromechanics and Microengineering*, vol. 20, no. 3, p. 035 030, Mar. 2010, ISSN: 0960-1317. DOI: 10.1088/0960-1317/20/3/035030. [Online]. Available: https://doi.org/10.1088%2F0960-1317%2F20%2F3%2F035030.

[75] R. Mahameed, M. A. El-Tanani, and G. M. Rebeiz, "A zipper RF MEMS tunable capacitor with interdigitated RF and actuation electrodes," *Journal of Micromechanics and Microengineering*, vol. 20, no. 3, p. 035 014, Feb. 2010, ISSN: 0960-1317. DOI: 10.1088/0960-1317/20/3/035014. [Online]. Available: https://doi.org/10.1088%2F0960-1317%2F20%2F3%2F035014.

[76] M. Ramezani, S. Severi, H. A. C. Tilmans, and K. D. Meyer, "Study of electrical breakdown and secondary pull-in failure modes for NEM relays," *Journal of Micromechanics and Microengineering*, vol. 27, no. 1, p. 015 030, Nov. 2016, ISSN: 0960-1317. DOI: 10.1088/1361-6439/27/1/015030. [Online]. Available: https://doi.org/10.1088%2F1361-6439%2F27%2F1%2F015030.

[77] Y. Song, M. Kim, M. Seo, and J. Yoon, "A complementary dual-contact MEMS switch using a "zipping" technique," *Journal of Microelectromechanical Systems*, vol. 23, no. 3, pp. 710–718, Jun. 2014, ISSN: 1057-7157. DOI: 10.1109/JMEMS.2013.2281835.

[78] R. Parsa, W. S. Lee, M. Shavezipur, J. Provine, R. Maboudian, S. Mitra, H. P. Wong, and R. T. Howe, "Laterally actuated platinum-coated polysilicon NEM Relays," *Journal of Microelectromechanical Systems*, vol. 22, no. 3, pp. 768–778, Jun. 2013, ISSN: 1057-7157. DOI: 10.1109/JMEMS.2013.2244779.

[79] D. A. Czaplewski, G. A. Patrizi, G. M. Kraus, J. R. Wendt, C. D. Nordquist, S. L. Wolfley, M. S. Baker, and M. P. d. Boer, "A nanomechanical switch for integration with CMOS logic," *Journal of Micromechanics and Microengineering*, vol. 19, no. 8, p. 085 003, Jul. 2009, ISSN: 0960-1317. DOI: 10.1088/0960-1317/19/8/085003. [Online]. Available: https://doi.org/10.1088%2F0960-1317%2F19%2F8%2F085003.

[80] E. E. Jones, K. D. Murphy, and M. R. Begley, "Mechanical measurements of adhesion in microcantilevers: Transitions in geometry and cyclic energy changes," *Experimental Mechanics*, vol. 43, no. 3, pp. 280–288, Sep. 2003, ISSN: 0014-4851, 1741-2765. DOI: 10.1007/BF02410526. [Online]. Available: https://link.springer.com/article/10.1007/BF02410526.

[81] E. E. Jones, M. R. Begley, and K. D. Murphy, "Adhesion of micro-cantilevers subjected to mechanical point loading: Modeling and experiments," *Journal of the Mechanics and Physics of Solids*, vol. 51, no. 8, pp. 1601–1622, Aug. 2003, ISSN: 0022-5096. DOI: 10.1016/S0022-5096(03)00025-5. [Online]. Available: http://www.sciencedirect.com/science/article/pii/S0022509603000255.

[82] Z. C. Leseman, S. P. Carlson, and T. J. Mackin, "Experimental measurements of the strain energy release rate for stiction-failed microcantilevers using a single-cantilever beam peel test," *Journal of Microelectromechanical Systems*, vol. 16, no. 1, pp. 38–43, Feb. 2007, ISSN: 1057-7157. DOI: 10.1109/JMEMS.2006.883570.

[83] O. Bochobza-Degani, D. Elata, and Y. Nemirovsky, "An efficient DIPIE algorithm for CAD of electrostatically actuated MEMS devices," *Journal of Microelectromechanical Systems*, vol. 11, no. 5, pp. 612–620, Oct. 2002, ISSN: 1057-7157. DOI: 10.1109/JMEMS.2002.803280.

[84] R. C. Batra, M. Porfiri, and D. Spinello, "Analysis of electrostatic MEMS using meshless local Petrov–Galerkin (MLPG) method," *Engineering Analysis with Boundary Elements*, Applications in Mirco and Nano Electromechanical Systems, vol. 30, no. 11, pp. 949–962, Nov. 2006, ISSN: 0955-7997. DOI: 10.1016/j.enganabound.2006.04.008. [Online]. Available: http://www.sciencedirect.com/science/article/pii/S0955799706001287.

[85] L. Medina, R. Gilat, and S. Krylov, "Bistability criterion for electrostatically actuated initially curved micro plates," *International Journal of Engineering Science*, vol. 130, pp. 75–92, Sep. 2018, ISSN: 0020-7225. DOI: 10.1016/j.ijengsci.2018.05.006. [Online]. Available: http://www.sciencedirect.com/science/article/pii/S0020722518303987.

[86] D. Bernstein, P. Guidotti, and J. A. Pelesko, "Mathematical analysis of an electrostatically actuated MEMS devices," *Proceedings of the Modeling and Simulation of Microsystems MSM*, pp. 489–492, 2000.

[87] A. S. Kovacs, "Fully electronic method of measuring post-release gap and gradient/residual stress of a MEMS cantilever," Ph.D. Purdue University, United States – Indiana, 2015. [Online]. Available: http://search.proquest.com.ezproxy.lib.purdue.edu/docview/1709250603/abstract/3620D82F3BFC4500PQ/1.

[88] P. Blondy, A. Crunteanu, A. Pothier, P. Tristant, A. Catherinot, and C. Champeaux, "Effects of atmosphere on the reliability of RF-MEMS capacitive switches," in *2007 European Microwave Conference*, Oct. 2007, pp. 1346–1348. DOI: 10.1109/EUMC.2007.4405452.

[89] A. Nowodzinski, T. Toussaint, A. Koszewski, and F. Souchon, "EFM study of the influence of humidity on charge injection and charge relaxation in silicon nitride used in electrostatically actuated MEMS," in *2011 16th International Solid-State Sensors, Actuators and Microsystems Conference*, Jun. 2011, pp. 2895–2898. DOI: 10.1109/TRANSDUCERS.2011.5969569.

[90] D. C. Hurley, "Contact resonance force microscopy techniques for nanomechanical measurements," in *Applied Scanning Probe Methods XI: Scanning Probe Microscopy Techniques*, ser. NanoScience and Technology, B. Bhushan and H. Fuchs, Eds., Berlin, Heidelberg: Springer, 2009, pp. 97–138, ISBN: 978-3-540-85037-3. DOI: . [Online]. Available: .

[91] U. Rabe, "Atomic force acoustic microscopy," in *Applied Scanning Probe Methods II: Scanning Probe Microscopy Techniques*, ser. NanoScience and Technology, B. Bhushan and H. Fuchs, Eds., Berlin, Heidelberg: Springer, 2006, pp. 37–90, ISBN: 978-3-540-27453-7. DOI: . [Online]. Available: .

[92] E. Soergel, "Piezoresponse force microscopy (PFM)," *Journal of Physics D: Applied Physics*, vol. 44, no. 46, p. 464 003, Nov. 2011, Publisher: IOP Publishing, ISSN: 0022-3727. DOI: 10.1088/0022-3727/44/46/464003. [Online]. Available: https://doi.org/10.1088/0022-3727/44/46/464003.

[93] N. Balke, S. Jesse, A. N. Morozovska, E. Eliseev, D. W. Chung, Y. Kim, L. Adamczyk, R. E. García, N. Dudney, and S. V. Kalinin, "Nanoscale mapping of ion diffusion in a lithium-ion battery cathode," *Nature Nanotechnology*, vol. 5, no. 10, pp. 749–754, Oct. 2010, Number: 10 Publisher: Nature Publishing Group, ISSN: 1748-3395. DOI: 10.1038/nnano.2010.174. [Online]. Available: https://www.nature.com/articles/nnano.2010.174.

[94] G. Binnig, C. F. Quate, and C. Gerber, "Atomic force microscope," *Physical Review Letters*, vol. 56, no. 9, pp. 930–933, Mar. 1986, Publisher: American Physical Society. DOI: 10.1103/PhysRevLett.56.930. [Online]. Available: https://link.aps.org/doi/10.1103/PhysRevLett.56.930.

[95] J. P. Killgore and F. W. DelRio, "Contact resonance force microscopy for viscoelastic property measurements: From fundamentals to state-of-the-art applications," *Macromolecules*, vol. 51, no. 18, pp. 6977–6996, Sep. 2018, Publisher: American Chemical Society, ISSN: 0024-9297. DOI: 10.1021/acs.macromol.8b01178. [Online]. Available: https://doi.org/10.1021/acs.macromol.8b01178.

[96] Y. Efremov, T. Okajima, and A. Raman, "Measuring viscoelasticity of soft biological samples using atomic force microscopy," *Soft Matter*, vol. 16, no. 1, pp. 64–81, 2020, Publisher: Royal Society of Chemistry. DOI: 10.1039/C9SM01020C. [Online]. Available: https://pubs.rsc.org/en/content/articlelanding/2020/sm/c9sm01020c.

[97] M. J. Cadena, Y. Chen, R. G. Reifenberger, and A. Raman, "Sub-surface AFM imaging using tip generated stress and electric fields," *Applied Physics Letters*, vol. 110, no. 12, p. 123 108, Mar. 2017, Publisher: American Institute of Physics, ISSN: 0003-6951. DOI: 10.1063/1.4977837. [Online]. Available: https://aip.scitation.org/doi/full/10.1063/1.4977837.

[98] J. P. Killgore, J. Y. Kelly, C. M. Stafford, M. J. Fasolka, and D. C. Hurley, "Quantitative subsurface contact resonance force microscopy of model polymer nanocomposites," *Nanotechnology*, vol. 22, no. 17, p. 175 706, Mar. 2011, Publisher: IOP Publishing, ISSN: 0957-4484. DOI: 10.1088/0957-4484/22/17/175706. [Online]. Available: https://doi.org/10.1088%2F0957-4484%2F22%2F17%2F175706.

[99] C. Ma, Y. Chen, W. Arnold, and J. Chu, "Detection of subsurface cavity structures using contact-resonance atomic force microscopy," *Journal of Applied Physics*, vol. 121, no. 15, p. 154 301, Apr. 2017, Publisher: American Institute of Physics, ISSN: 0021-8979. DOI: 10.1063/1.4981537. [Online]. Available: https://aip.scitation.org/doi/full/10.1063/1.4981537.

[100] W. Wang, C. Ma, Y. Chen, L. Zheng, H. Liu, and J. Chu, "Subsurface imaging of flexible circuits via contact resonance atomic force microscopy," *Beilstein Journal of Nanotechnology*, vol. 10, no. 1, pp. 1636–1647, Aug. 2019, Publisher: Beilstein-Institut, ISSN: 2190-4286. DOI: 10.3762/bjnano.10.159. [Online]. Available: https://www.beilstein-journals.org/bjnano/articles/10/159.

[101] C. Ma, W. Wang, Y. Chen, W. Arnold, and J. Chu, "Depth-sensing using AFM contact-resonance imaging and spectroscopy at the nanoscale," *Journal of Applied Physics*, vol. 126, no. 12, p. 124 302, Sep. 2019, Publisher: American Institute of Physics, ISSN: 0021-8979. DOI: 10.1063/1.5113567. [Online]. Available: https://aip.scitation.org/doi/full/10.1063/1.5113567.

[102] S. V. Kalinin and D. A. Bonnell, "Imaging mechanism of piezoresponse force microscopy of ferroelectric surfaces," *Physical Review B*, vol. 65, no. 12, p. 125 408, Mar. 2002, Publisher: American Physical Society. DOI: 10.1103/PhysRevB.65.125408. [Online]. Available: https://link.aps.org/doi/10.1103/PhysRevB.65.125408.

[103] S. V. Kalinin, R. Shao, and D. A. Bonnell, "Local phenomena in oxides by advanced scanning probe microscopy," *Journal of the American Ceramic Society*, vol. 88, no. 5, pp. 1077–1098, 2005, ISSN: 1551-2916. DOI: https://doi.org/10.1111/j.1551-2916.2005.00383.x. [Online]. Available: https://ceramics.onlinelibrary.wiley.com/doi/abs/10.1111/j.1551-2916.2005.00383.x.

[104] D. A. Bonnell, S. V. Kalinin, A. L. Kholkin, and A. Gruverman, "Piezoresponse Force Microscopy: A Window into Electromechanical Behavior at the Nanoscale," *MRS Bulletin*, vol. 34, no. 9, pp. 648–657, Sep. 2009, ISSN: 1938-1425. DOI: 10.1557/mrs2009.176. [Online]. Available: https://doi.org/10.1557/mrs2009.176.

[105] L. Jin, F. Li, and S. Zhang, "Decoding the fingerprint of ferroelectric loops: Comprehension of the material properties and structures," *Journal of the American Ceramic Society*, vol. 97, no. 1, pp. 1–27, 2014, ISSN: 1551-2916. DOI: https://doi.org/10.1111/jace.12773. [Online]. Available: https://ceramics.onlinelibrary.wiley.com/doi/abs/10.1111/jace.12773.

[106] R. O'Hayre, M. Lee, and F. B. Prinz, "Ionic and electronic impedance imaging using atomic force microscopy," *Journal of Applied Physics*, vol. 95, no. 12, pp. 8382–8392, Jun. 2004, Publisher: American Institute of Physics, ISSN: 0021-8979. DOI: 10.1063/1.1737047. [Online]. Available: https://aip.scitation.org/doi/10.1063/1.1737047.

[107] S. Jesse, A. Kumar, T. M. Arruda, Y. Kim, S. V. Kalinin, and F. Ciucci, "Electrochemical strain microscopy: Probing ionic and electrochemical phenomena in solids at the nanometer level," *MRS Bulletin*, vol. 37, no. 7, pp. 651–658, Jul. 2012, ISSN: 1938-1425. DOI: 10.1557/mrs.2012.144. [Online]. Available: https://doi.org/10.1557/mrs.2012.144.

[108] A. N. Morozovska, E. A. Eliseev, N. Balke, and S. V. Kalinin, "Local probing of ionic diffusion by electrochemical strain microscopy: Spatial resolution and signal formation mechanisms," *Journal of Applied Physics*, vol. 108, no. 5, p. 053 712, Sep. 2010, Publisher: American Institute of Physics, ISSN: 0021-8979. DOI: 10.1063/1.3460637. [Online]. Available: https://aip.scitation.org/doi/full/10.1063/1.3460637.

[109] U. Rabe, E. Kester, and W. Arnold, "Probing linear and non-linear tip–sample interaction forces by atomic force acoustic microscopy," *Surface and Interface Analysis*, vol. 27, no. 5-6, pp. 386–391, 1999, ISSN: 1096-9918. DOI: 10.1002/(SICI)1096-9918(199905/06)27:5/6⟨386::AID-SIA526⟩3.0.CO;2-J. [Online]. Available: https://onlinelibrary.wiley.com/doi/abs/10.1002/%28SICI%291096-9918%28199905/06%2927%3A5/6%3C386%3A%3AAID-SIA526%3E3.0.CO%3B2-J.

[110] U. Rabe, M. Kopycinska, S. Hirsekorn, and W. Arnold, "Evaluation of the contact resonance frequencies in atomic force microscopy as a method for surface characterisation (invited)," *Ultrasonics*, vol. 40, no. 1, pp. 49–54, May 2002, ISSN: 0041-624X. DOI: 10.1016/S0041-624X(02)00089-6. [Online]. Available: http://www.sciencedirect.com/science/article/pii/S0041624X02000896.

[111] D. Rupp, U. Rabe, S. Hirsekorn, and W. Arnold, "Nonlinear contact resonance spectroscopy in atomic force microscopy," *Journal of Physics D: Applied Physics*, vol. 40, no. 22, pp. 7136–7145, Nov. 2007, Publisher: IOP Publishing, ISSN: 0022-3727. DOI: 10.1088/0022-3727/40/22/041. [Online]. Available: https://doi.org/10.1088%2F0022-3727%2F40%2F22%2F041.

[112] G. Haller and S. Ponsioen, "Nonlinear normal modes and spectral submanifolds: Existence, uniqueness and use in model reduction," *Nonlinear Dynamics*, vol. 86, no. 3, pp. 1493–1534, Nov. 2016, ISSN: 1573-269X. DOI: 10.1007/s11071-016-2974-z. [Online]. Available: https://doi.org/10.1007/s11071-016-2974-z.

[113] R. M. Rosenberg, "Normal modes of nonlinear dual-mode systems," *Journal of Applied Mechanics*, vol. 27, no. 2, pp. 263–268, Jun. 1960, ISSN: 0021-8936. DOI: 10.1115/1.3643948. [Online]. Available: https://doi.org/10.1115/1.3643948.

[114] S. Shaw and C. Pierre, "Non-linear normal modes and invariant manifolds," *Journal of Sound and Vibration*, vol. 150, no. 1, pp. 170–173, 1991, Publisher: Elsevier. DOI: 10.1016/0022-460X(91)90412-D. [Online]. Available: https://hal.archives-ouvertes.fr/hal-01310674.

[115] H.-J. Butt, B. Cappella, and M. Kappl, "Force measurements with the atomic force microscope: Technique, interpretation and applications," *Surface Science Reports*, vol. 59, no. 1, pp. 1–152, Oct. 2005, ISSN: 0167-5729. DOI: 10.1016/j.surfrep.2005.08.003. [Online]. Available: http://www.sciencedirect.com/science/article/pii/S0167572905000488.

[116] H.-J. Butt and M. Jaschke, "Calculation of thermal noise in atomic force microscopy," *Nanotechnology*, vol. 6, no. 1, pp. 1–7, Jan. 1995, Publisher: IOP Publishing, ISSN: 0957-4484. DOI: 10.1088/0957-4484/6/1/001. [Online]. Available: https://doi.org/10.1088/0957-4484/6/1/001.

[117] B. V. Derjaguin, V. M. Muller, and Y. P. Toporov, "Effect of contact deformations on the adhesion of particles," *Journal of Colloid and Interface Science*, vol. 53, no. 2, pp. 314–326, Nov. 1975, ISSN: 0021-9797. DOI: 10.1016/0021-9797(75)90018-1. [Online]. Available: http://www.sciencedirect.com/science/article/pii/0021979775900181.

[118] N. H. Shaik, R. G. Reifenberger, and A. Raman, "Nanomechanical mapping in air or vacuum using multi-harmonic signals in tapping mode atomic force microscopy," *Nanotechnology*, 2020, ISSN: 0957-4484. DOI: 10.1088/1361-6528/ab9390. [Online]. Available: http://iopscience.iop.org/10.1088/1361-6528/ab9390.

[119] A. Labuda, M. Kocuń, W. Meinhold, D. Walters, and R. Proksch, "Generalized Hertz model for bimodal nanomechanical mapping," *Beilstein Journal of Nanotechnology*, vol. 7, no. 1, pp. 970–982, Jul. 2016, Publisher: Beilstein-Institut, ISSN: 2190-4286. DOI: 10.3762/bjnano.7.89. [Online]. Available: https://www.beilstein-journals.org/bjnano/articles/7/89.

[120] I. N. Sneddon, "The relation between load and penetration in the axisymmetric boussinesq problem for a punch of arbitrary profile," *International Journal of Engineering Science*, vol. 3, no. 1, pp. 47–57, May 1965, ISSN: 0020-7225. DOI: 10.1016/0020-7225(65)90019-4. [Online]. Available: http://www.sciencedirect.com/science/article/pii/0020722565900194.

[121] U. Rabe, K. Janser, and W. Arnold, "Vibrations of free and surface-coupled atomic force microscope cantilevers: Theory and experiment," *Review of Scientific Instruments*, vol. 67, no. 9, pp. 3281–3293, Sep. 1996, Publisher: American Institute of Physics, ISSN: 0034-6748. DOI: 10.1063/1.1147409. [Online]. Available: https://aip.scitation.org/doi/10.1063/1.1147409.

[122] J. Melcher, S. Hu, and A. Raman, "Equivalent point-mass models of continuous atomic force microscope probes," *Applied Physics Letters*, vol. 91, no. 5, p. 053 101, Jul. 2007, ISSN: 0003-6951. DOI: 10.1063/1.2767173. [Online]. Available: https://aip.scitation.org/doi/abs/10.1063/1.2767173.

[123] R. Wagner and J. P. Killgore, "Photothermally excited force modulation microscopy for broadband nanomechanical property measurements," *Applied Physics Letters*, vol. 107, no. 20, p. 203 111, Nov. 2015, Publisher: American Institute of Physics, ISSN: 0003-6951. DOI: 10.1063/1.4935982. [Online]. Available: https://aip.scitation.org/doi/full/10.1063/1.4935982.

[124] A. Labuda, K. Kobayashi, D. Kiracofe, K. Suzuki, P. H. Grütter, and H. Yamada, "Comparison of photothermal and piezoacoustic excitation methods for frequency and phase modulation atomic force microscopy in liquid environments," *AIP Advances*, vol. 1, no. 2, p. 022 136, Jun. 2011, Publisher: American Institute of Physics. DOI: 10.1063/1.3601872. [Online]. Available: https://aip.scitation.org/doi/full/10.1063/1.3601872.

[125] A. A. Savkar and K. D. Murphy, "The evolution of stiction repair for microelectromechanical system cantilevers using periodic excitation," *Journal of Sound and Vibration*, vol. 329, no. 2, pp. 189–201, Jan. 2010, ISSN: 0022-460X. DOI: 10.1016/j.jsv.2009.09.003. [Online]. Available: http://www.sciencedirect.com/science/article/pii/S0022460X09007032.

[126] A. Alexeenko, S. Chigullapalli, J. Zeng, X. Guo, A. Kovacs, and D. Peroulis, "Uncertainty in microscale gas damping: Implications on dynamics of capacitive MEMS switches," *Reliability Engineering & System Safety*, vol. 96, no. 9, pp. 1171–1183, Sep. 2011, ISSN: 09518320. DOI: 10.1016/j.ress.2011.01.002. [Online]. Available: http://linkinghub.elsevier.com/retrieve/pii/S095183201100069X.